DESIGN AND ANALYSIS OF AN ELECTRICALLY SMALL INDUCTIVELY LOADED SECTOR ANTENNA FOR FREQUENCY RECONFIGURATION USING VARACTOR DIODES

BY

STEVEN MICHAEL DAWSON

THESIS

Submitted in partial fulfillment of the requirements
for the degree of Master of Science in Electrical and Computer Engineering
in the Graduate College of the
University of Illinois at Urbana-Champaign, 2011

Urbana, Illinois

Adviser:

Professor Jennifer T. Bernhard

ABSTRACT

Global wireless communications networks are facing an ever increasing demand to deliver content to the consumer. Along with increased consumption of wireless bandwidth, consumers demand that their devices interface with a plethora of different wireless bands and protocols. To meet this demand, mobile devices have a multiplicity of antennas designed to work for specific bands. However, as mobile communication demands continue to grow, the number of antennas will become even more constrained by size and cost. In order to address this issue, an inductively loaded, electrically small, frequency reconfigurable, sector antenna that covers most consumer frequency bands has been developed. This thesis details the design and characterization of the antenna element, which tunes the GSM 900, GSM 1800, 3G, WiFi, and WiMAX bands. The antenna developed is modified from a previous design for frequency reconfiguration using varactor diodes placed in inductive loads. In order to allow for frequency agility, a DC bias network is carefully designed utilizing blocking capacitors to allow for an impedance match over the bands of interest. Characterization of the antenna on different ground plane sizes and construction issues are also addressed. Finally the inductively loaded, electrically small, frequency reconfigurable, sector antenna is fabricated and measured to confirm the simulation analysis. Comments on the radiation patterns, efficiency, and gain are also provided.

ACKNOWLEDGMENTS

The author would like to thank the following people, without whose help and support none of this work would be possible: Dr. Jennifer Bernhard for her overwhelming support, guidance, and motivation; Siwen Yong for his tremendous amount of help with every step of this project; and Stephen Yan for answering question upon question and giving helpful advice. Special thanks also goes to CSIT for funding this thesis project.

Thanks to the whole of the antennas research group, who made living in Champaign fun and interesting. Special thanks to Professor Mayes and Professor Klock for their expertise and many consultations on this project. I would also like to thank my family and especially my fiancée Amanda for her incredible love and support throughout this entire process.

TABLE OF CONTENTS

CHAPTER 1 INTRODUCTION 1

1.1 SYNOPSIS 1
1.2 MOTIVATION 3

CHAPTER 2 BACKGROUND 4

2.1 ELECTRICALLY SMALL ANTENNAS 4
2.2 FREQUENCY RECONFIGURABLE ANTENNAS 5
2.3 STACKED SECTOR ANTENNA 7
2.3.1 Dual sector antenna with vertical inductive loads 7
2.3.2 Addition of inductive feed 10

CHAPTER 3 FREQUENCY RECONFIGURABLE SECTOR ANTENNA 12

3.1 PRELIMINARY CHANGES IN ANTENNA GEOMETRY 12
3.2 CANDIDATE LOCATIONS FOR VARACTOR PLACEMENT 15
3.3 TUNING OF LOAD RECONFIGURED ANTENNA 19
3.3.1 Addition of third inductive load 19
3.3.2 Addition of final two inductive loads 21
3.4 EFFECT OF VARACTOR PLACEMENT ON IMPEDANCE MATCH AND RADIATION EFFICIENCY 23
3.4.1 Simulations performed with 1 pF capacitance 23
3.4.2 Simulations performed with 3.2 pF capacitance 32
3.5 CHARACTERIZATION OF THE RECONFIGURABLE ELEMENT 33
3.6 RESULTS 37

CHAPTER 4 GROUND PLANE SIZE EFFECTS 39

4.1 EFFECT OF GROUND PLANE SIZE ON ANTENNA PERFORMANCE 39
4.2 PATTERN CONSIDERATIONS 43

CHAPTER 5 TUNING RANGE STUDY 47

5.1 IMPROVING MAXIMUM ANTENNA TUNING RANGE 47
5.1.1 Cant angle study 47
5.1.2 Sector back edge study 52
5.1.3 Sector height study 55
5.2 SINGLE VARACTOR MAXIMUM TUNING DESIGN 59
5.2.1 Radiation efficiency and gain of the SVMTD 61
5.3 MEASURED RESULTS FOR THE SVMTD 63
5.4 DOUBLE VARACTOR DESIGN 65
5.4.1 Operating physics of the dual varactor antenna 69
5.4.2 Candidate varactors for frequency tuning 73
5.4.3 Results 74

CHAPTER 6 DC BIAS NETWORK 76

6.1 PRELIMINARY BIAS NETWORK 76

6.2 Revised Bias Network 77
6.2.1 Candidate blocking capacitors 78
6.2.2 Addition of blocking capacitors 81
6.3 Characterization of Antenna with Blocking Capacitors 82
6.3.1 Broadband blocking capacitors 83
6.3.2 Combination of blocking capacitors 87
6.4 Practical Construction Considerations 91
6.5 Results 93
CHAPTER 7 FINAL DESIGN 94
7.1 Approach 94
7.2 Realistic Varactor Modeling 94
7.2.1 Realistic varactor model 95
7.2.2 Simulations with realistic varactor model 97
7.3 Final Design Simulations 103
7.3.1 Simulation results 104
7.4 Fabrication and Measurements 109
7.4.1 Equipment and materials 109
7.4.2 Construction 110
7.4.3 Measured results 112
7.4.4 Efficiency measurement 126
CHAPTER 8 CONCLUSION AND FUTURE WORK 131
REFERENCES 132

Chapter 1

INTRODUCTION

1.1 Synopsis

With the proliferation of wireless communication, the sizes of electronic devices are rapidly decreasing while the information transmitted by these devices increases every day. Consumers' thirst for increased functionality of their mobile devices has led many wireless companies to search for new antenna design techniques to satisfy the demand. Since many of these devices operate at multiple frequency bands (GSM or CDMA, 802.11b/g/n Wi-Fi, Bluetooth, WiMax) utilizing a single antenna for each operating frequency is impractical. While current designs often feature multiple co-located antennas in order to maintain multi-band functionality, in the future wireless devices will require a more robust solution.

An elegant solution to the aforementioned problems is a frequency reconfigurable, electrically small antenna. Instead of including a multiplicity of antennas that take up valuable real-estate, a frequency reconfigurable, electrically small antenna would be able to cover the entire frequency range with a single antenna element.

However, designing such an element to cover much of the wireless band does not come without caveats. The costs of using electrically small antennas include poor efficiencies, design of "invisible" bias networks, conductor losses, and narrow band impedance matching over large frequency ranges to name a few. Designing the antenna to maintain a balance between these costs and performance will be a difficult challenge.

To overcome these difficulties, the antenna must be designed with its biggest limitation, the bias network, in mind. Unlike conventional reconfigurable antennas, which assume that the bias network remains relatively "invisible" to the radiating structure [1, 2], the impedance changes much more rapidly across the radiating structure of an electrically small antenna, making it extremely difficult to integrate the bias network without adversely affecting the antenna's radiating characteristics. Therefore, extra care must be taken such that the inclusion of any tuning or switching elements does not result in significant radiation from the bias network.

Keeping the above-mentioned concerns in mind, it was determined that the inductively loaded dual sector antenna developed here at the University of Illinois [3, 4] was a good starting point for a frequency reconfigurable design. How changes in antenna geometry affect its radiation characteristics have been studied in detail previously in [4], providing valuable insight when determining the necessary alterations for meeting certain design criteria.

Chapter 2 develops the background behind electrically small antennas and frequency reconfigurable antennas before introducing the inductively loaded dual sector antenna. Subsequently, Chapter 3 details the changes required to achieve frequency reconfigurability. Also included are parametric studies on modifications in antenna geometry that were not considered in [4], and the effect of tuning element placement on antenna efficiency. Subsequently, antenna impedance match is characterized across the frequencies of operation at the end of Chapter 3.

Chapter 4 focuses on the effects of variations in ground plane size on impedance match and radiation pattern, whereas Chapter 5 details the studies performed to improve the frequency agility of the antenna. To facilitate tuning over the entire desired frequency range, a second tuning varactor was incorporated into the structure and varactor candidates for a practical design were determined.

Chapter 6 revisits the antenna bias network, and documents the changes needed to maintain DC isolation on the tuning varactor(s) during antenna operation. To improve the understanding of the designed antenna, Chapter 7 presents a circuit model for predictions of antenna performance when the design is varied.

Finally, Chapter 8 details the final antenna design characterized through simulation and measurement of fabricated antennas.

1.2 Motivation

The motivation for this thesis comes from a research agreement between the University of Illinois and Centre for Strategic Infocomm Technologies (CSIT). As described in the research proposal this work involves the design, analysis and prototyping of small linear arrays composed of electrically small reconfigurable antennas. The work presented in this thesis is a portion of the research agreement focusing on the analysis and design of the antenna element to be later used in these linear arrays. In accordance with the research proposal, the specifications for the final product are given in Table 1.1.

Table 1.1: Target reference specifications for array.

Parameter	**Goal**
Operating Frequency	0.9-3.5 GHz
Instantaneous Bandwidth	10-30 MHz
Minimum Return Loss	10 dB
Maximum Sidelobe Level relative to Peak	-13 dB
Target Array Size	0.25 m^2
Maximum Array Depth	10 cm
Overall Array Gain	10 dBi

While the operating frequency of the project is defined at 0.9 – 3.5 GHz, the agreement stipulates that the actual frequency bands of interest are the GSM 900, GSM 1800, 3G, WiFi, and WiMAX bands. The use of an electrically small antenna as the fundamental element for this project is based on several issues that arise from the final goals for the system. First, the selection of electrically small antennas comes from the desire to have a fairly narrow instantaneous bandwidth while having the ability to be tuned across the specified wide frequency bandwidth. Second, since a single element will not be able to achieve the specified gain over this bandwidth, the selection of electrically small antennas supports their use in an array to increase the effective gain of the available aperture by approximating a uniformly illuminated aperture equal to the size of the array. It is anticipated that this will be helpful in maximizing the gain and reducing sidelobe level over the entire frequency tuning range for the final project design.

Chapter 2

BACKGROUND

2.1 Electrically Small Antennas

An electrically small antenna can be generally defined as any antenna whose largest physical dimension is small compared to the operational wavelength of the antenna. The exact definition of what is considered "small" is often discussed by many authors, but the most prevalent definition was proposed by Wheeler in 1946.

Wheeler described an electrically small antenna as one "whose maximum dimension is less than the radian length" [5], where the radian length is $\lambda/2\pi$. If a sphere surrounding the antenna is drawn with the radian length as the radius a new term radiansphere can be defined. The radiansphere, defined by Wheeler [5], is a hypothetical sphere that marks the physical transition of radiation from the "near fields" contained in the sphere to the "far fields" located outside of the radiansphere. Therefore according to Wheeler, an antenna can be considered to be electrically small if the propagation constant (k) times the minimum radius required to enclose the antenna (a) is less than one ($ka \leq 1$).

Various types of electrically small antennas exist: these include stacked sector antennas [6], folded spherical helices [7], stacked conical antennas [8], spherical dipole antennas [9], and inductively loaded dipoles [10]. Electrically small antennas are present in nearly every industry that uses antennas for communication purposes. In these areas, limitations on package size, weight, and operational frequencies often require the use of electrically small antennas. The antenna's intended use usually dictates the design focus used in making the antenna look electrically larger.

Ideally, these antennas are designed to appear electrically larger while maintaining good radiation characteristics such as large impedance match bandwidth, radiation efficiency, and gain figures. However, fundamental limits exist that limit how electrically small an antenna can become before it is impractical to use. A figure of merit that is often used when analyzing antenna performance is the radiation power factor [5], or quality factor (Q) [11]. The quality factor or Q is defined to be the ratio of the time-averaged stored magnetic or electric energy to

radiated power ($Q = \frac{2\omega W}{P}$). As the antenna becomes more and more electrically small, the Q increases drastically [6]. A high Q implies that the stored electric or magnetic energies surrounding the antenna are large, resulting in a higher presence of current on the antenna structure. As the current density increases on the antenna structure, conductive losses also become larger and since the radiation resistance of small antennas is small, the efficiency of the overall antenna decreases.

In the design of electrically small antennas, trade-offs must be made in order to realistically meet design goals. In order to drastically decrease the size of an antenna, sacrifices in performance figures must be made to achieve the more important design priorities.

2.2 Frequency Reconfigurable Antennas

A frequency reconfigurable antenna is defined as an antenna whose operating frequency can be tuned or "reconfigured" without a serious redesign of the entire antenna. One of the first frequency reconfigurable antenna was proposed by Schaubert et al. in June of 1980 [12] and consisted of a microwave patch antenna whose frequency of operation could be varied by the changing the distance between two shorting posts placed on the patch. They demonstrated that by varying the distance between the posts they could effectively tune the patch antenna from 1450 to 1700 MHz while maintaining a VSWR impedance match < 2. While this work utilized physical posts that needed to be added or removed to achieve this tuning effect, the authors theorized that rf-switching diodes could easily be implemented into the design to allow for an electronically controlled frequency reconfigurable antenna.

Schaubert et al. expanded on this preliminary result in 1981 with a paper presenting the original patch modified by additional shorting posts for polarization diversity [13]. The authors also detailed one of the major difficulties of designing frequency reconfigurable antennas; the design of a control network to individually bias the diodes (or reconfiguration devices) while simultaneously isolating the R.F. signal present on the antenna as to not adversely affect the performance of the antenna.

Another paper published soon after Schaubert et al.'s original work was the development of a frequency agile microstrip antenna that utilized varactor diodes for tuning mechanisms [14]. In this paper, Bhartia and Bahl present a microstrip patch antenna with varactor diodes mounted on the radiating edges of the antenna and tuned using a reverse bias DC voltage. By changing the capacitance present at the radiating edge of the antenna the effective electrical length of the patch was altered resulting in a shift in operating frequency. Bhartia and Bahl show that by using this technique of varactor loading they can realize a continuous operating frequency shift of 1.5 to 1.8 GHz for a rectangular patch and 1.8 to 2.4 GHz for a circular patch antenna.

Recently, much work has been focused on the development of small antennas utilizing frequency reconfiguration techniques to cover a multitude of frequency bands. One such design is a PIFA that uses both PIN diode switches and a tuning varactor diode in order to cover the USPCS (1.85-1.99 GHz), WCDMA (19.2-2.18 GHz), m-WiMAX (3.4-3.6 GHz), and WLAN (5.15-5.825 GHz) bands [15]. This combinational design allows for switching between m-WiMAX and WLAN bands via the PIN diode and tuning of the USPCS to WCDMA bands using the tunable varactor diode.

Frequency reconfigurable antennas have evolved considerably since their inception, but their design can generally be categorized into two main methods: switched and continuous. Switched reconfigurable antennas rely on abrupt on/off mechanisms to achieve a change to a specific operating frequency or band. Continuously tuned antennas utilize methods that allow for a smooth progression of the operating frequency over a specific range. In order to achieve frequency agility, both of these categories rely on the same basic theory: changing the effective electrical length of the antenna in order to make the antenna appear electrically larger or smaller.

The methods for achieving frequency reconfiguration typically rely on four different mechanisms: switches, variable reactive loading (this work), structural/mechanical changes, and material changes [16]. Switching mechanisms often use PIN diodes [17], or radio frequency microelectromechanical system (RF-MEMS) switches [18] to add or subtract physical lengths or sections of the antenna in order to achieve a discontinuous step in the frequency band. Tunable antennas with variable reactive loading use devices such as FETs [19] or varactor diodes [20] that allow for gradual changes in reactance values that have the effect of continuously tuning the

effective electrical length of the antenna. Structural or mechanical mechanisms often use actuators or other methods to physically change the structure, size, or orientation of the antenna to enable frequency tuning. Variable material frequency reconfigurable antennas promote the tuning of an antenna by applying either a static electric or magnetic field to change the relative permittivity or permeability of a ferrite substrate changing the effective electrical length of the antenna.

While all of these mechanisms can be used to achieve frequency reconfiguration, for this specific application where the element size and the ease of construction of the DC bias network are limiting factors, only switched or variable reactive loading techniques can be practically implemented.

2.3 Stacked Sector Antenna

2.3.1 Dual sector antenna with vertical inductive loads

The dual sector antenna used in this thesis is derived from an earlier design, which used multiple, stacked, conical radiators to achieve an electrically small antenna with a wide bandwidth [21]. By closely stacking the radiating elements, bandwidth was increased since each element had a resonance at a slightly different frequency. The efficiency and gain bandwidth of this antenna were shown to be good for an electrically small antenna [18].

To further reduce the physical size of the antenna, the radiating elements were adapted to triangular, sector shaped elements as shown in Figure 2.1 [4]. In addition, parametric studies were performed and different geometric properties were changed one at a time [4]. The geometric degrees of freedom are: sector areas (Figure 2.2), vertical load widths (Figure 2.3), sector cant angle (Figure 2.4), height above ground plane (Figure 2.5), middle sector proximity to feed point (Figure 2.6), sector flare angle and ground plane size. Results are available in Soldner [4].

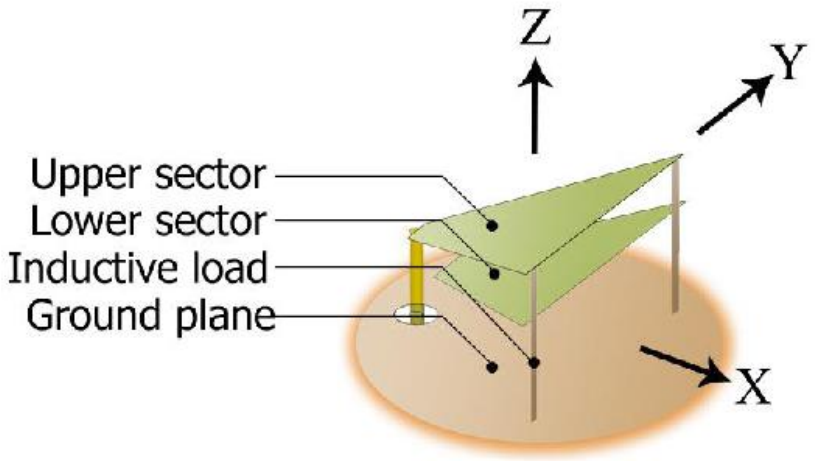

Figure 2.1: Dual sector antenna with vertical loads and SMA probe feeds connected to upper sector only (Graphics from [4]).

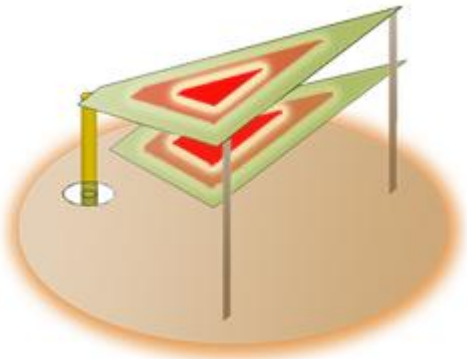

Figure 2.2: Diagram of dual sector antenna showing variance in sector areas (Graphics from [4]).

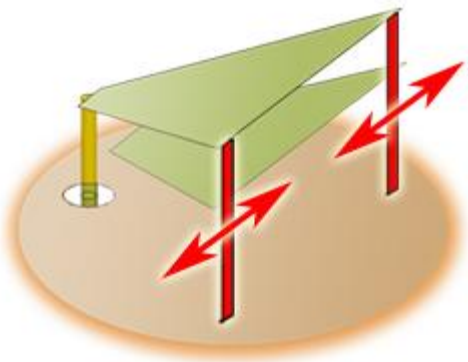

Figure 2.3: Diagram of dual sector antenna showing variance in load widths (Graphics from [4]).

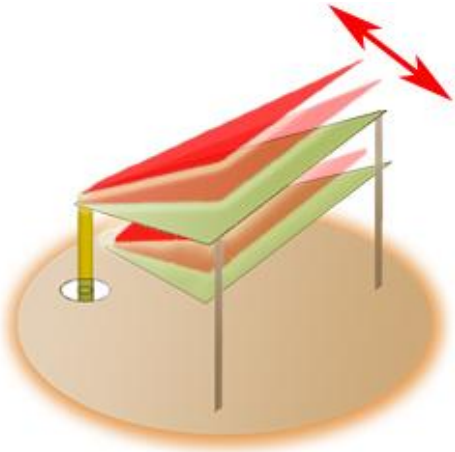

Figure 2.4: Diagram of dual sector antenna showing changes in cant angle (Graphics from [4]).

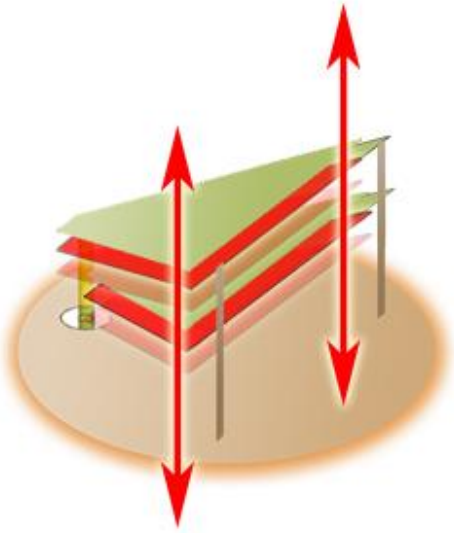

Figure 2.5: Diagram of dual sector antenna showing changes in sector height (Graphics from [4]).

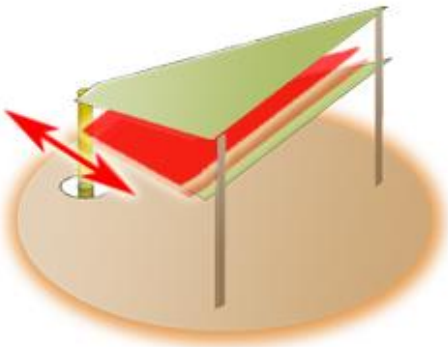

Figure 2.6: Diagram of dual sector antenna showing variance in lower sector length (Graphics from [4]).

2.3.2 Addition of inductive feed

In an effort to further reduce the antenna's apparent electrical size, an inductive feed was included in the antenna as indicated in Figure 2.7 [4]. Examination of the antenna performance indicated that without the feed, the overall antenna input impedance was capacitive, and inclusion of the inductive feed results in the antenna impedance response being centered over the real axis of the Smith chart. Finally, additional simulations were performed and a suitable antenna geometry was chosen. A picture of the fabricated antenna is presented in Figure 2.8 [4]. Measurements were performed and a 100 MHz impedance bandwidth from 2.61 to 2.71 GHz was achieved [4].

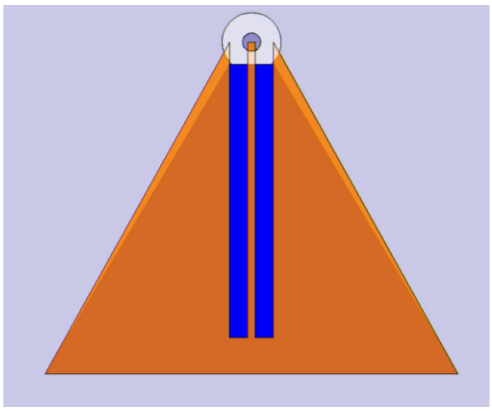

Figure 2.7: Top view diagram of dual sector antenna showing inductive feed (orange color indicates conductive material) [4].

Even though this antenna has been optimized to achieve a 3.75% impedance bandwidth, further modifications are necessary to achieve frequency reconfiguration. First, since our designed antenna must be electrically small at the desired upper frequency of operation, the antenna must be further miniaturized such that $ka \leq 1$. Furthermore, since the goal of this project is to achieve frequency reconfigurability and not bandwidth improvement, as in [4], the bottom sector of the antenna was removed to ease both its fabrication and analysis. Finally, additional considerations relating to the inclusion of tuning and/or switching elements are necessary. The above concerns are addressed in detail in the following chapter.

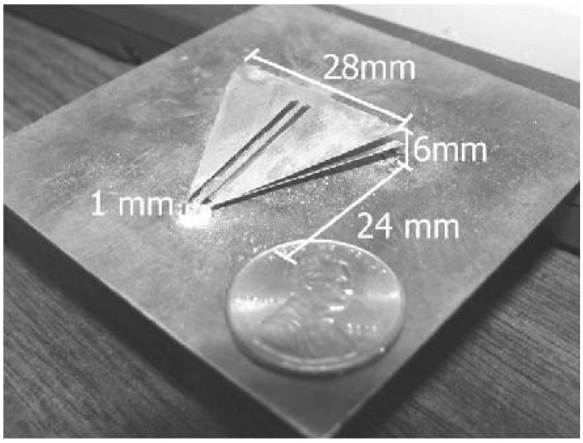

Figure 2.8: Photograph of dual-sector antenna from [4] used as a starting point for this research.

Chapter 3

FREQUENCY RECONFIGURABLE SECTOR ANTENNA

3.1 Preliminary Changes in Antenna Geometry

In order to achieve frequency reconfiguration the dual sector design described in Chapter 2 must be modified such that its effective electrical length can be changed. Therefore the structure was considered as presented and further modified for frequency reconfiguration.

For the antenna to be electrically small from 0.89 to 3.5 GHz, the antenna must have $ka \leq 1$ at 3.5 GHz. A quick calculation using Soldner's antenna [4] indicates that $ka = 1.42$ at 3.5 GHz, and therefore further antenna miniaturization is necessary. In addition, the second sector of the antenna is removed to prevent dual frequency behavior while attempting frequency reconfiguration. Lastly, to simplify antenna fabrication, the antenna cant angle is removed, and the antenna top sector is at a 90^{o} angle from the probe. A diagram of the simulated antenna is presented in Figure 3.1.

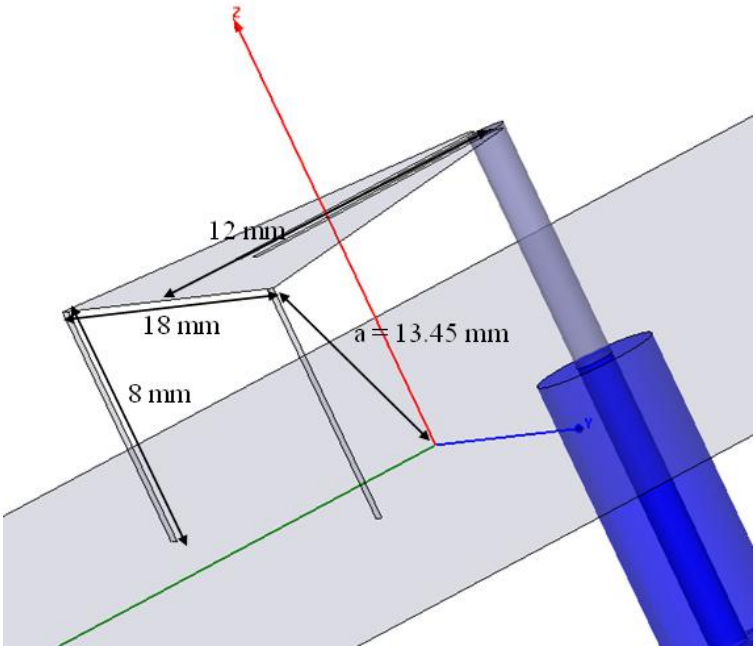

Figure 3.1: Diagram of new antenna geometry (Graphics from HFSS).

In Figure 3.1, the antenna had width = 18 mm, length = 12 mm and height = 8 mm. Assuming an infinite ground plane, a = 13.45 mm and $ka = 0.986$ at 3.5 GHz. In addition, all vertical inductive widths were 0.5 mm. As indicated in Figure 3.2, the inductive feed was 9 mm long and 0.9 mm wide and the slot widths were 0.5 mm. These values were chosen not only to maintain $ka \leq 1$ throughout the desired range of operating frequencies, but also to achieve the highest possible ka and therefore maximum gain.

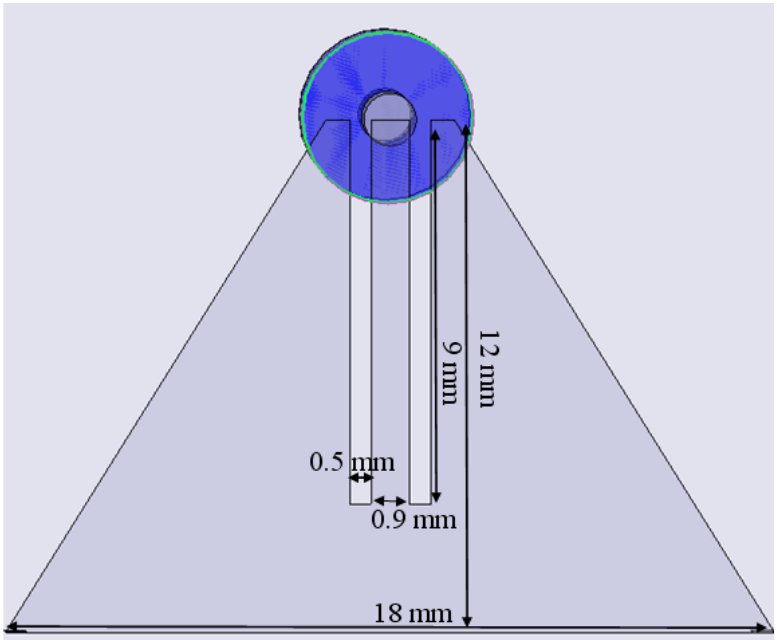

Figure 3.2: Feed dimensions of simulated antenna (Graphics from HFSS).

In order to accurately model the antenna which was to be fabricated, brass was used in the simulations as the material for the antenna sector and vertical inductive loads. Furthermore, a constraint was placed such that convergence occurs only when the calculated antenna radiation efficiency does not change by more than 1% between successive adaptive passes. By adding the additional constraint for convergence, more accurate simulation results can be obtained throughout the design of the antenna. This constraint remains consistent throughout all simulations performed in this thesis. Simulation results using Ansoft's HFSS for VSWR versus frequency on an infinite ground plane are presented in Figure 3.3.

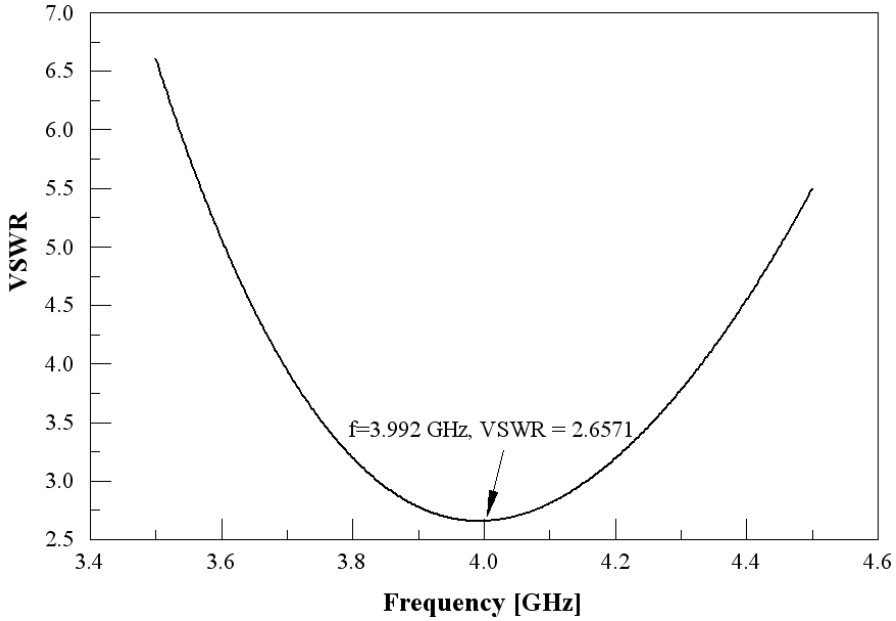

Figure 3.3: Simulated VSWR versus frequency.

Examination of Figure 3.3 indicates that the frequency of best match is at 3.99 GHz, which is outside the range of desired frequencies. In addition, return loss is also higher than 10 dB, since VSWR = 2.66. However, it was anticipated that the inclusion of a tuning varactor to the structure would decrease the match frequency and affect the impedance match due to the additional reactance placed at the edge of the sector.

In this application, varactors are preferable to RF MEMs switches since reconfiguration across multiple frequency bands over a wide range is required. Moreover, the necessary bias voltages for RF MEMS devices are too large (on the order of 25-90 V) for small portable devices. In addition, it is desirable to incorporate as few tuning or switching elements as possible to ease the bias network design and prevent significant degradation in radiation efficiency due to the losses present in the semiconductor devices. In light of this design choice, simulations were performed to examine the effect of varactor placement on the frequency reconfiguration ability of the antenna.

3.2 Candidate Locations for Varactor Placement

Using varactor diodes as tuning mechanisms involves determining where in the design they can be placed to maximize their effect on the antenna and how they will be biased without affecting the antennas performance. DC bias networks for electrically small antennas require careful design to ensure that the network does not become a part of the radiating structure. The design of the DC bias network is discussed in detail in Chapter 6, but a proposed preliminary bias network is detailed in Figure 3.4. With the reconfigurable sector design proposed in Section 3.1 and the bias network pictured in Figure 3.4, two locations for varactor placement exist – in the inductive feed (feed reconfiguration) and in the vertical inductive loads (load reconfiguration), as indicated in Figures 3.5 and 3.6 respectively.

In order to determine which location would allow for greater frequency reconfiguration, simulations were performed where the varactors were modeled as 1 pF capacitors with dimensions 0.5 by 1 mm utilizing a "lumped RLC" boundary condition in HFSS. The results from this reconfiguration study are presented in Figures 3.7 - 3.10.

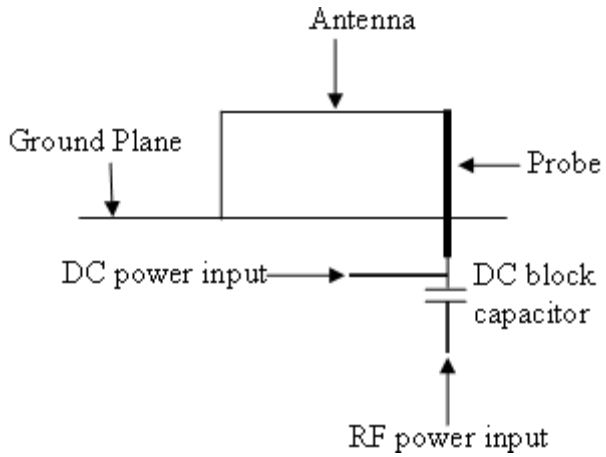

Figure 3.4: Diagram of proposed bias network.

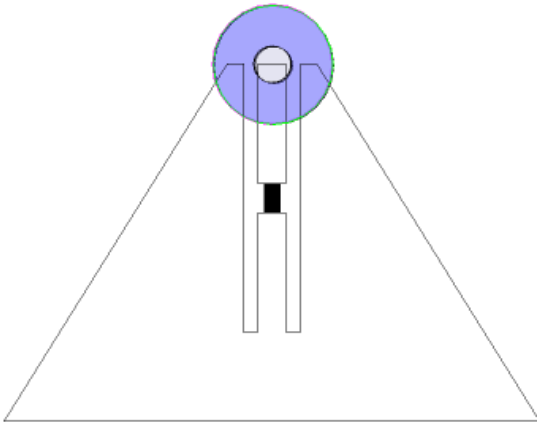

Figure 3.5: Inclusion of varactor in inductive feed (Graphics from HFSS).

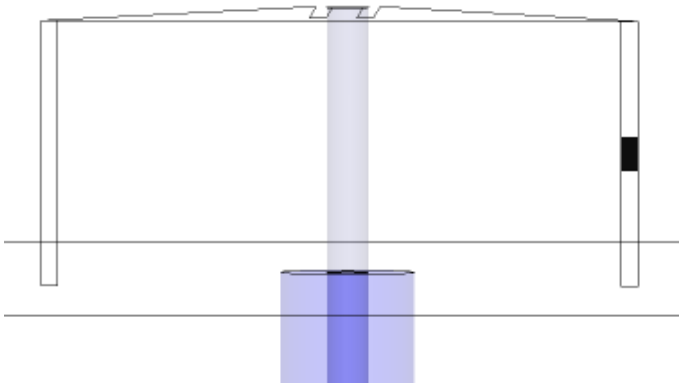

Figure 3.6: Inclusion of varactor in inductive load (Graphics from HFSS).

Figures 3.7 and 3.9 indicate that no good impedance match exists for either of these simple cases. However, the VSWR match with load reconfiguration is much better than with feed reconfiguration. Moreover, examination of Figures 3.8 and 3.10 indicates that the impedance circle is very large in both cases, but is tighter with load reconfiguration. Because of these conditions, it was determined that load reconfiguration exhibits better potential for frequency reconfiguration than feed reconfiguration.

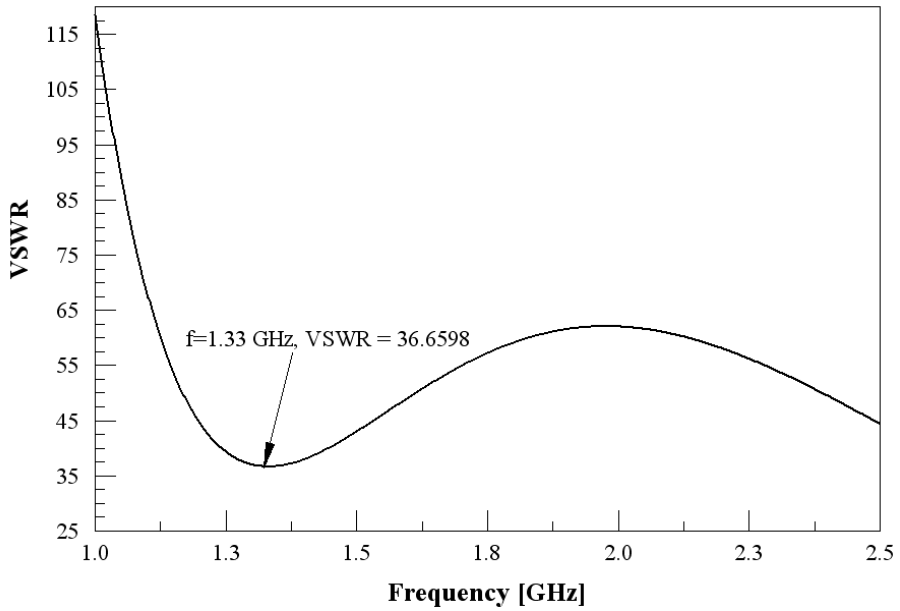

Figure 3.7: Simulated plot of VSWR versus frequency for feed reconfiguration.

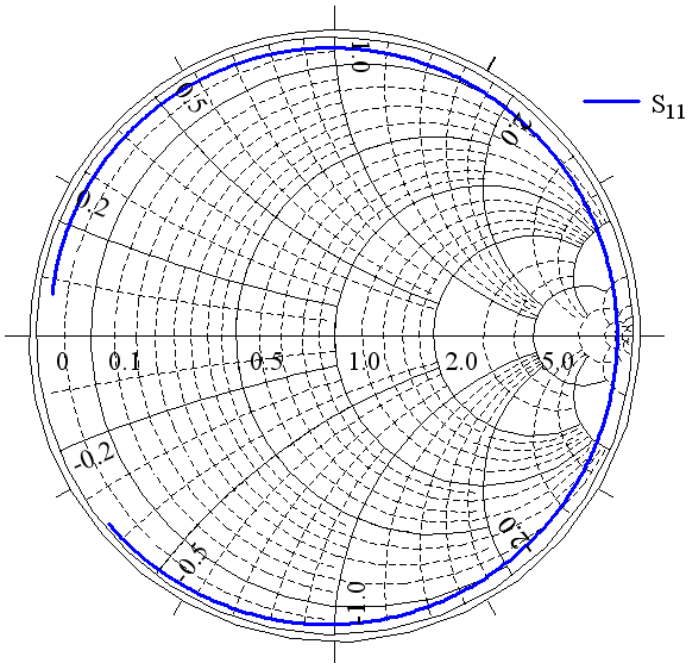

Figure 3.8: Simulated Smith chart plot from 1.0 to 2.5 GHz for feed reconfiguration.

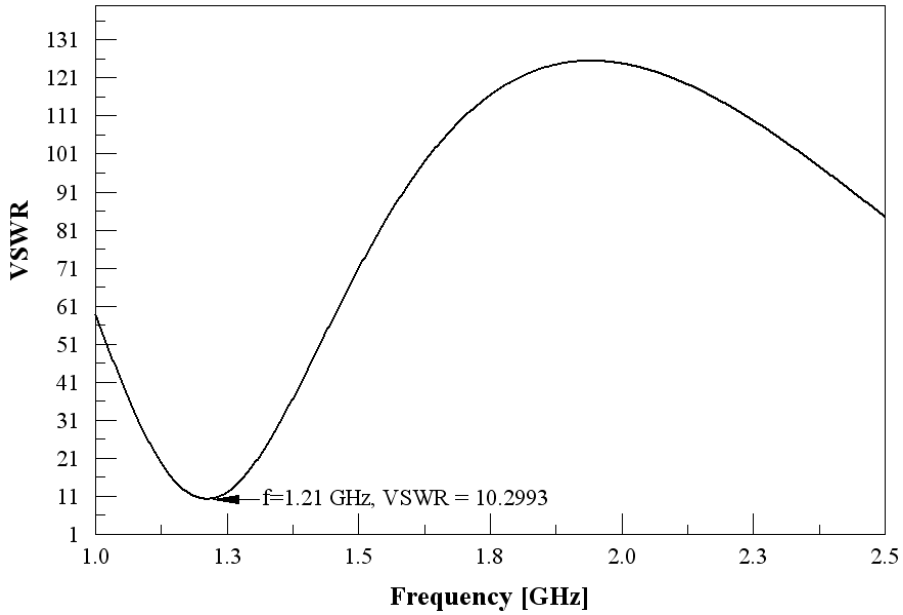

Figure 3.9: Simulated plot of VSWR versus frequency for load reconfiguration.

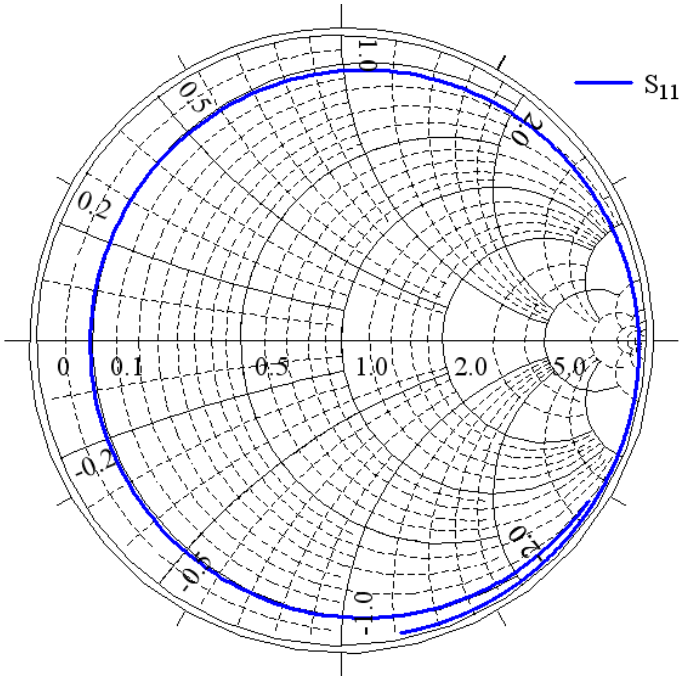

Figure 3.10: Simulated Smith chart plot from 1.0 to 2.5 GHz for load reconfiguration.

3.3 Tuning of Load Reconfigured Antenna

3.3.1 Addition of third inductive load

Even though the load-reconfigured antenna design exhibited the best potential for frequency reconfiguration, further tuning was necessary in order to improve its poor impedance match. Since the impedance circle was very large, as indicated in Figure 3.10, it was hypothesized that addition of a third vertical inductive load would alleviate the problem. The third load is to be added in parallel to the other two loads, serving to decrease the overall inductance of the antenna, thus tightening the impedance circle and improving the impedance match. A figure of the antenna is presented as Figure 3.11 and the simulated antenna response is presented in Figures 3.12 and 3.13.

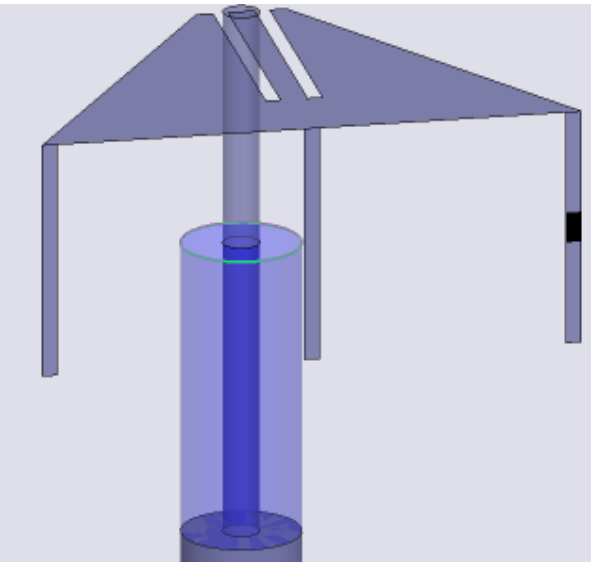

Figure 3.11: Load reconfigured antenna with 3 loads (Graphics from HFSS).

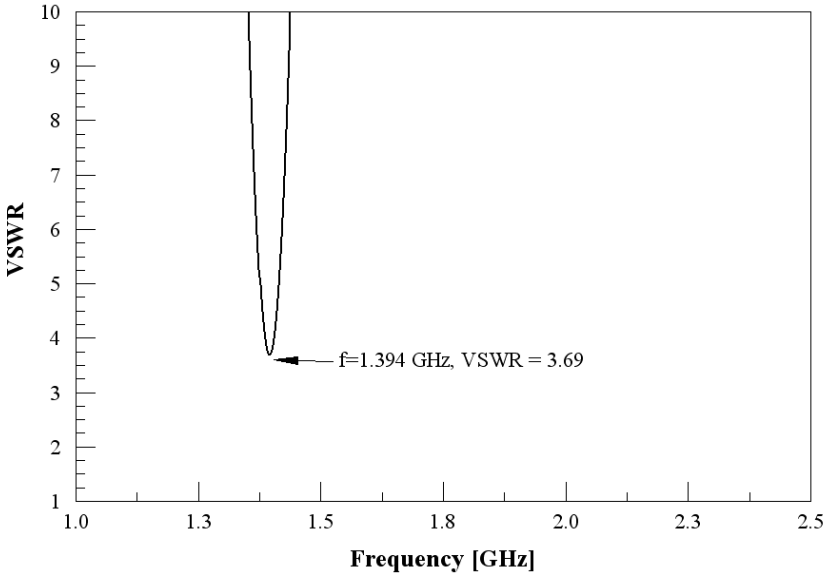

Figure 3.12: Simulated plot of VSWR versus frequency for load reconfigured antenna with 3 loads.

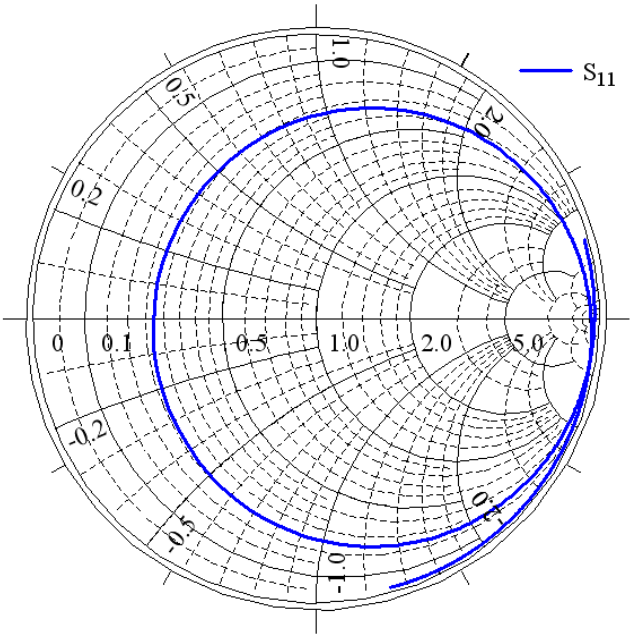

Figure 3.13: Simulated Smith chart plot from 1.0 to 2.5 GHz for load reconfigured antenna with 3 loads.

Examination of Figures 3.9 and 3.12 indicates that the addition of a third inductive load has led to both an increase in match frequency and an improvement in impedance match. In addition, comparison of Figures 3.10 and 3.13 indicates that the radius of the impedance circle has decreased by a sizeable margin. However, the match is still unsatisfactory for practical antenna

performance and two additional loads were included in the structure as detailed in the next subsection.

3.3.2 Addition of final two inductive loads

To further improve the impedance match, two additional inductive loads were added. The addition of the final two inductive loads decreased the inductance of the antenna so that a good impedance match could be realized. In addition, the effect of load placement on impedance match was studied by placing the loads at 3, 5 and 7 mm on either side of the antenna center and observing the results. A diagram of the antenna with loads placed at 5 mm is presented in Figure 3.14. Again, simulations in HFSS were performed and the results are presented in Figures 3.15 and 3.16.

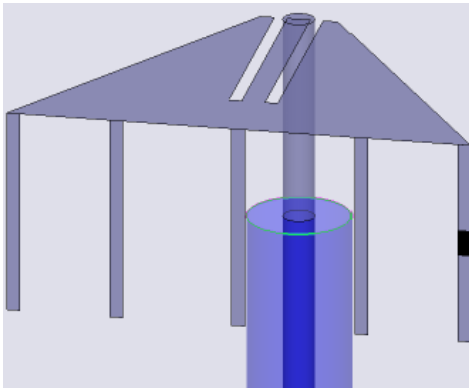

Figure 3.14: Load reconfigured antenna with 5 loads (Graphics from HFSS).

Examination of Figure 3.15 indicates that a good impedance match is achieved for all load placements. However, the match is best when the loads are placed 5 mm from the center. With the loads at 5 mm, the match frequency was 1.6 GHz with a VSWR of 1.13 and 10 MHz bandwidth. In addition, examination of Figure 3.16 indicates that the radius of the impedance circle decreases as the distance of the load from the antenna center increases.

Since the antenna depicted in Figure 3.14 exhibited the best match and had adequate bandwidth, it was chosen as the candidate antenna for frequency reconfiguation. Due to the three additional vertical loads, more candidate positions for varactor inclusion now exist for consideration. The effect of varactor placement on both the impedance match and radiated efficiency was examined and simulated results are presented next.

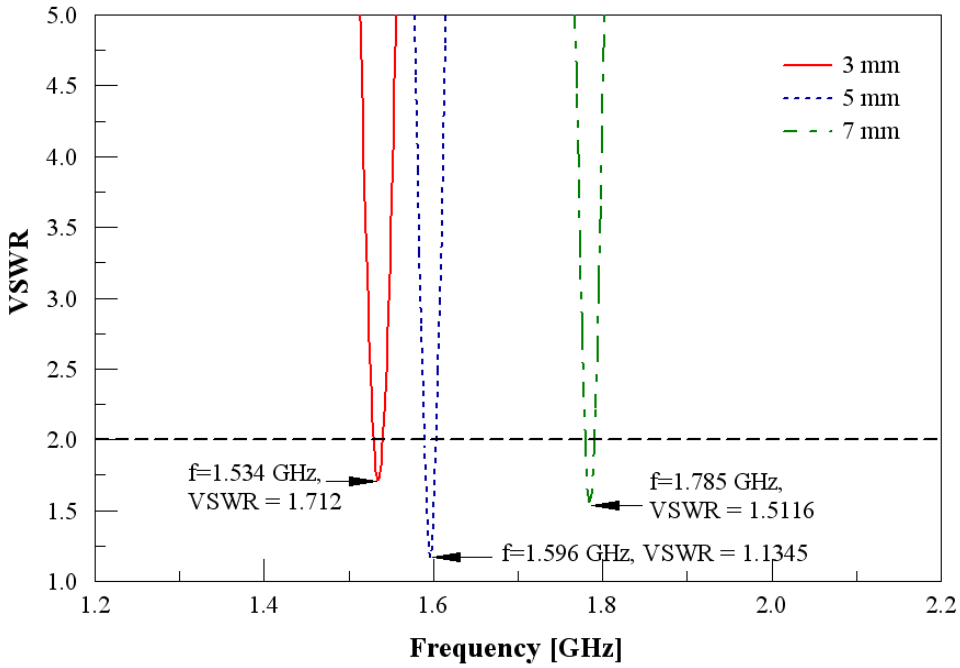

Figure 3.15: Simulated plot of VSWR versus frequency for load reconfigured antenna with 5 loads.

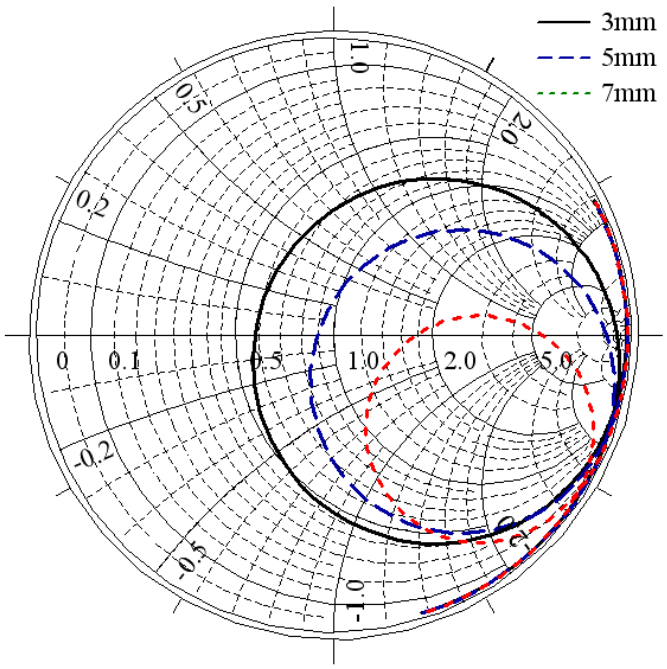

Figure 3.16: Simulated Smith chart plot for load reconfigured antenna with 5 loads from 1 to 2.5 GHz.

3.4 Effect of Varactor Placement on Impedance Match and Radiation Efficiency

3.4.1 Simulations performed with 1 pF capacitance

With the basic geometry of the antenna design chosen, it was desired to determine the best varactor positions for maximum frequency agility. In an effort to determine this, a 1 pF capacitor was incorporated into the structure in three different configurations, two of which are symmetric and the third asymmetric. In configuration 1, two capacitors are placed at the corner of the structure in a symmetric manner (Figure 3.17), whereas in configuration 2 (Figure 3.18), one capacitor is placed in the center load. Finally, in the third configuration (Figure 3.19), one capacitor is placed at the corner of the structure, as is done in prior simulations. Simulations in HFSS were performed with an infinite ground plane utilizing a fast sweep from 1.6 to 2.5 GHz and a 2 MHz step size. Again, a constraint was placed such that convergence occurs only when the calculated radiation efficiencies in successive passes differ by less than 1%. The total capacitance was kept constant in all three configurations by setting the capacitance in configurations 2 and 3 to 1 pF, whereas the capacitance in configuration 1 was set to 0.5 pF.

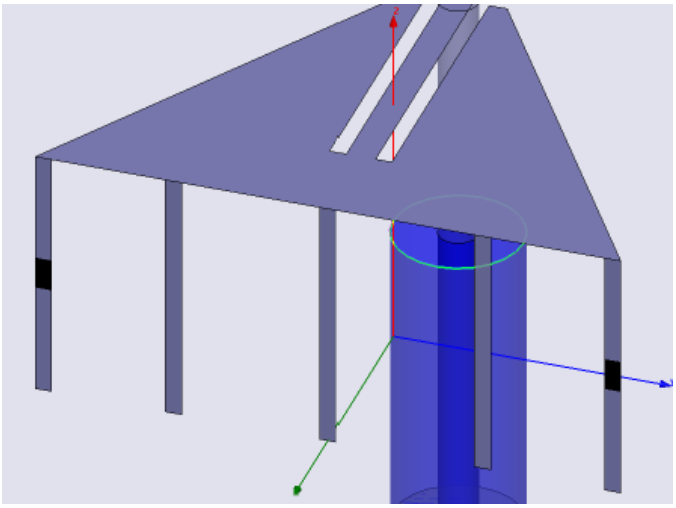

Figure 3.17: Placement of capacitors in configuration 1 (Graphics from HFSS).

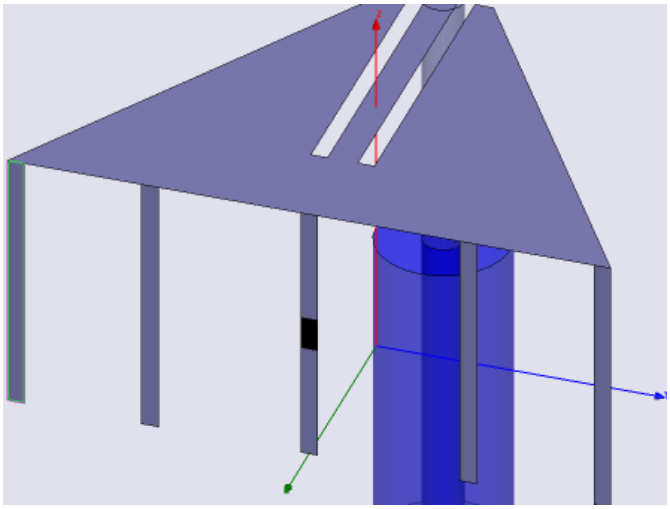

Figure 3.18: Placement of capacitor in configuration 2 (Graphics from HFSS).

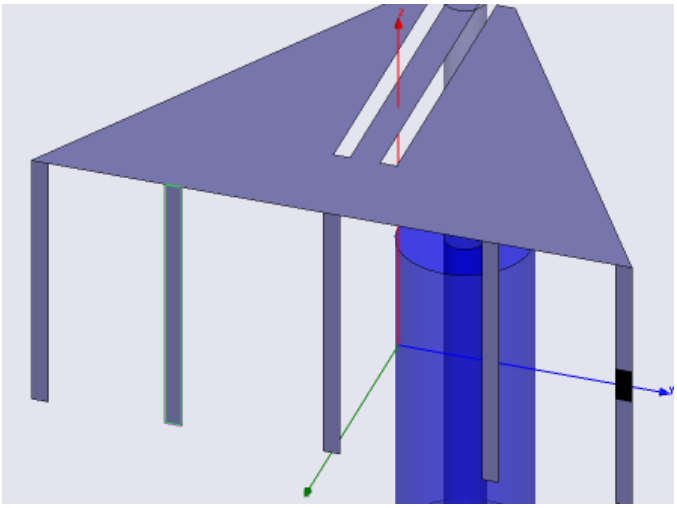

Figure 3.19: Placement of capacitor in configuration 3 (Graphics from HFSS).

Simulation results of VSWR versus frequency for all three configurations are presented in Figure 3.20. Examination of Figure 3.20 indicates that the antenna in configuration 1 is not well matched at all simulated frequencies, so it was not considered further. In addition, comparison of simulated results for configurations 2 and 3 indicate that the antenna is well matched at 1.822 GHz for configuration 2 and 1.608 GHz for configuration 3. Utilizing the HFSS antenna parameters calculation tool, the radiation efficiencies at these two frequencies were calculated and the results are summarized in Table 3.1.

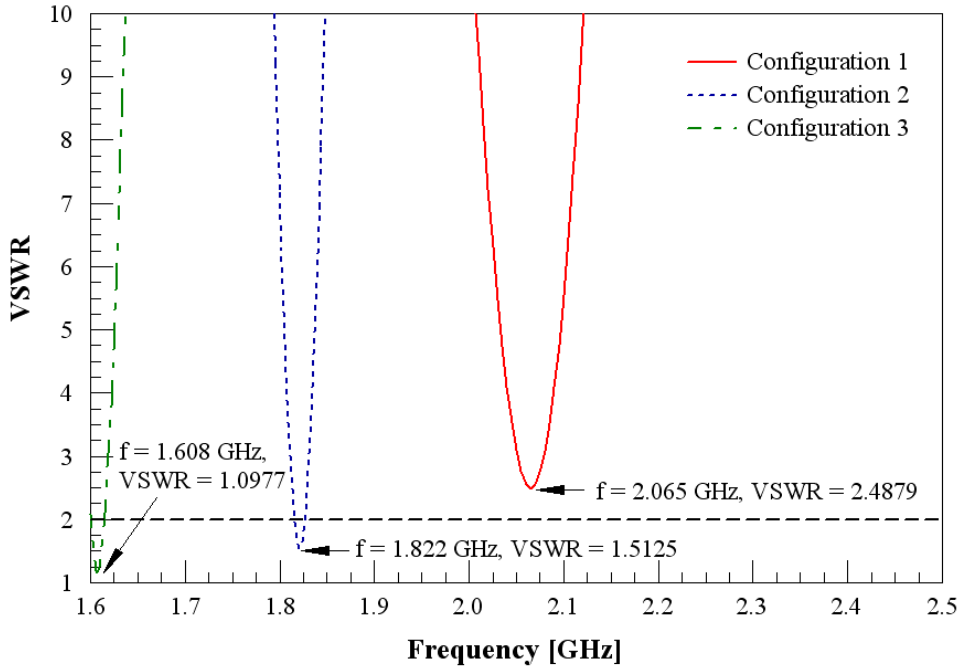

Figure 3.20: Simulated plot of VSWR versus frequency for capacitors in all three configurations.

Table 3.1: VSWR and radiated efficiency for antennas with 1 pF capacitance.

	Match frequency [GHz]	VSWR	Radiation efficiency
Configuration 2	1.822	1.51	6.9 %
Configuration 3	1.608	1.1	31.5%

Examination of Table 3.1 indicates that when the capacitor is placed in the center of the structure, the match frequency is higher and the radiation efficiency is lower. This is counterintuitive since at a higher frequency, the antenna is electrically larger and the radiation efficiency should be higher. An explanation is that capacitor placement results in a change in current flow, thus affecting efficiency. In configuration 2, the capacitor is placed in the center of the antenna and most current flows through the center inductive load. Due to the symmetry of the structure, current flows predominantly in a direction parallel to the x-axis, and radiation from any current flowing parallel to the y-axis cancels. However, asymmetric placement of the capacitor in configuration 3 results in no cancellation of radiation from currents flowing parallel to the y-axis, thus boosting radiation efficiency. Plots of current flow at the match frequency for configurations 2 and 3 are presented as Figures 3.21 and 3.22, respectively.

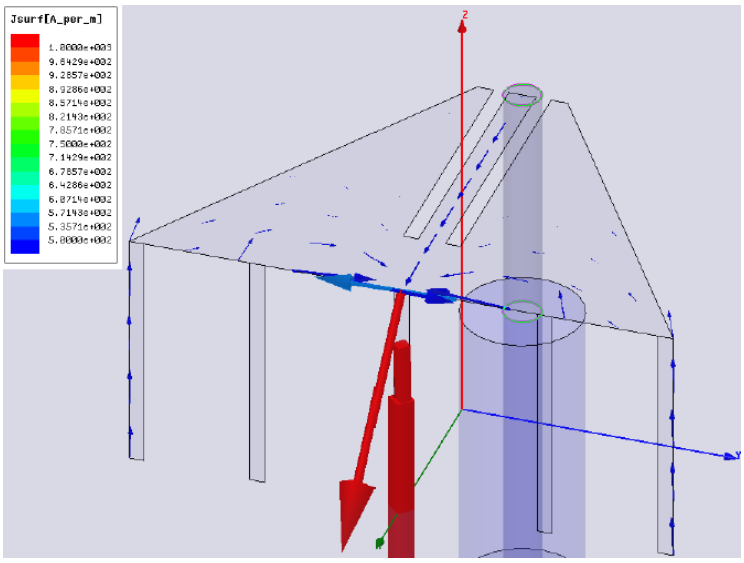

Figure 3.21: Current flow for antenna in configuration 2 (Graphics from HFSS).

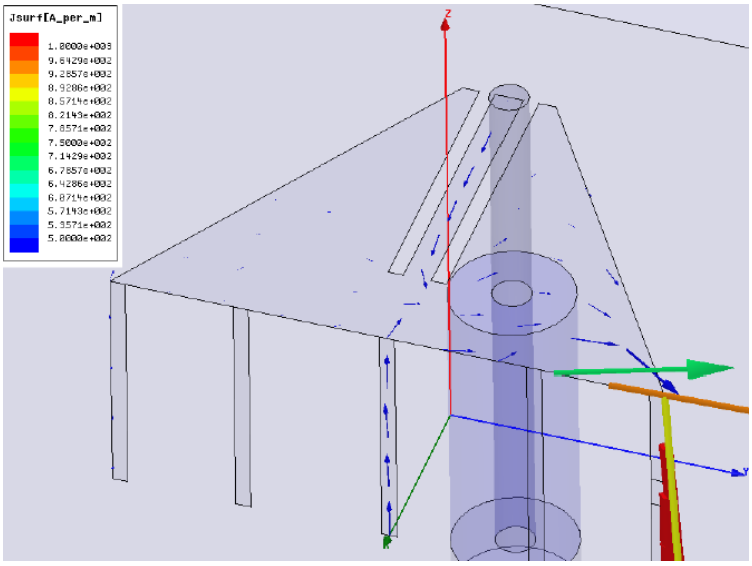

Figure 3.22: Current flow for antenna in configuration 3 (Graphics from HFSS).

To support further study, gain plots were generated and examined. If the additional cross polar components contribute to the antenna's higher efficiency, gain plots for the antenna in configuration 3 would indicate a much higher horizontal polarization component. Elevation plots of antenna gain for configuration 2 in the $\phi = 0^0$ and $\phi = 90^0$ planes are presented as Figures 3.23 and 3.24, respectively, with Figure 3.25 being the gain plot in the azimuth. Similarly, elevation plots of the gain for the antenna in configuration 3 in the $\phi = 0^0$ and $\phi = 90^0$ planes are presented as Figures 3.26 and 3.27, respectively, with Figure 3.28 being the gain plot in azimuth.

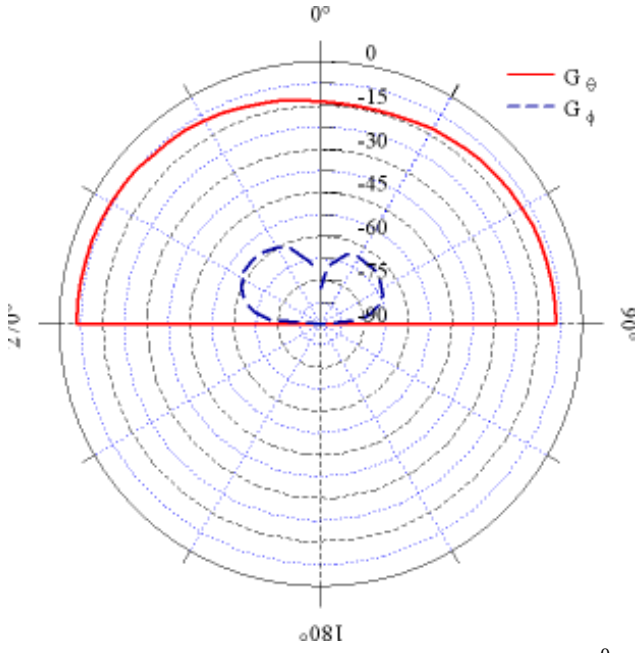

Figure 3.23: Simulated elevation plot of absolute gain along the $\phi = 0^0$ plane for configuration 2.

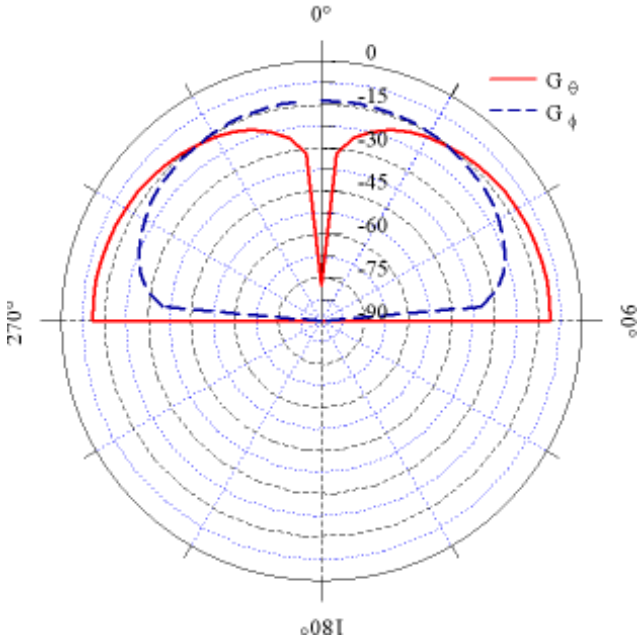

Figure 3.24: Simulated elevation plot of absolute gain along the $\phi = 90^0$ plane for configuration 2.

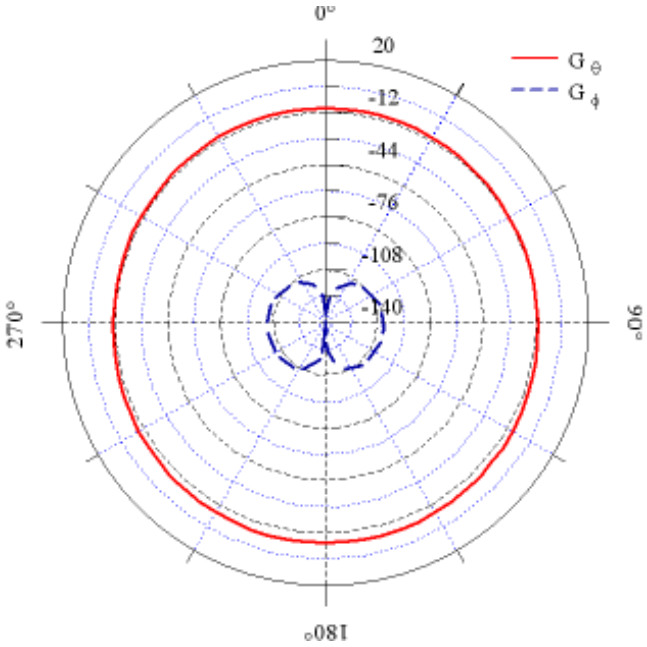

Figure 3.25: Simulated absolute gain plot in azimuth for configuration 2.

Examination of Figures 3.23 to 3.25 indicates that the radiation pattern of the antenna in configuration 2 resembles that of a monopole in the $\phi = 90^0$ plane. However, due to the currents flowing along the top sector of the antenna, the null at broadside in G_θ is not present, as indicated in Figure 3.24. In addition, comparison of Figures 3.23 and 3.26 indicates that in the $\phi = 0^0$ plane, G_φ is the dominant polarization in configuration 3 whereas G_θ is dominant in configuration 2. Since the radiation from currents flowing in opposite directions parallel to the y-axis offset for configuration 2, G_φ is suppressed and G_θ is dominant. The absence of this mechanism in configuration 3 results in G_φ being the dominant polarization. This supports the concept that the asymmetry in capacitor placement results in a stronger horizontal polarization component. Similarly, comparison of Figures 3.24 and 3.27 indicates that in the $\phi = 90^0$ plane, G_φ is the dominant polarization in configuration 2 whereas G_θ is dominant in configuration 3.

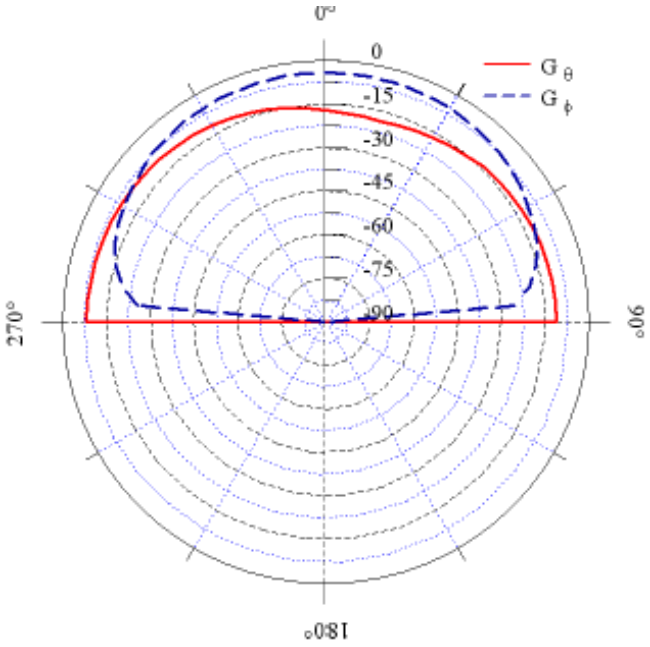

Figure 3.26: Simulated elevation plot of absolute gain along the $\phi = 0^0$ plane for configuration 3.

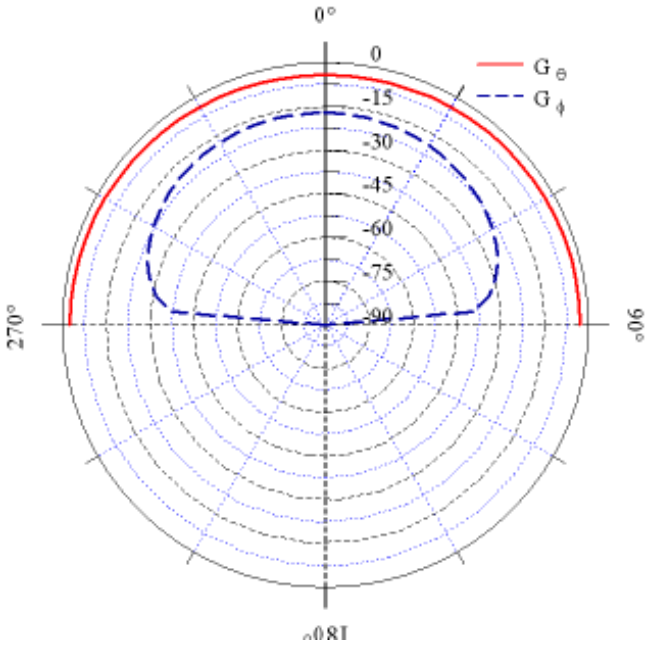

Figure 3.27: Simulated elevation plot of absolute gain along the $\phi = 90^0$ plane for configuration 3.

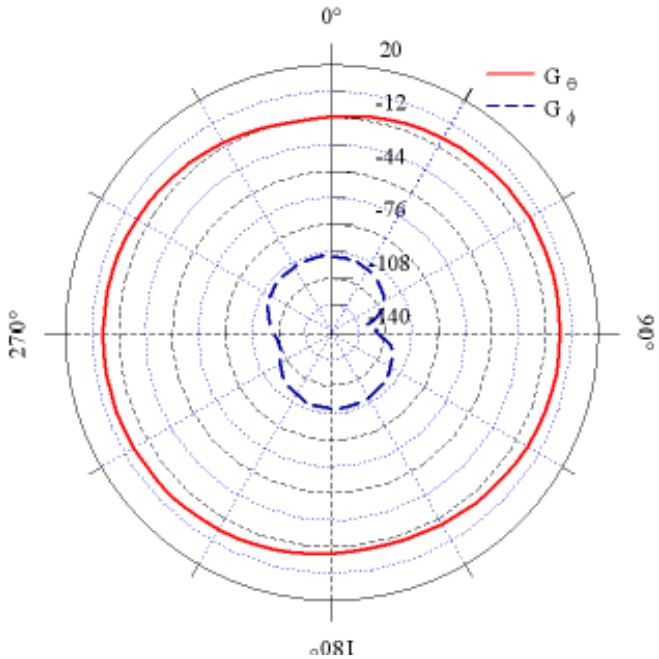

Figure 3.28: Simulated absolute gain plot in azimuth for configuration 3.

Further evidence that the discrepancy in radiation pattern for both configurations is due to symmetry is present in the gain plots for configuration 1. Since the capacitors are implemented in a symmetrical manner as in configuration 2, the gain plots for both configurations should be similar, and this is seen to be the case from Figures 3.29 to 3.31.

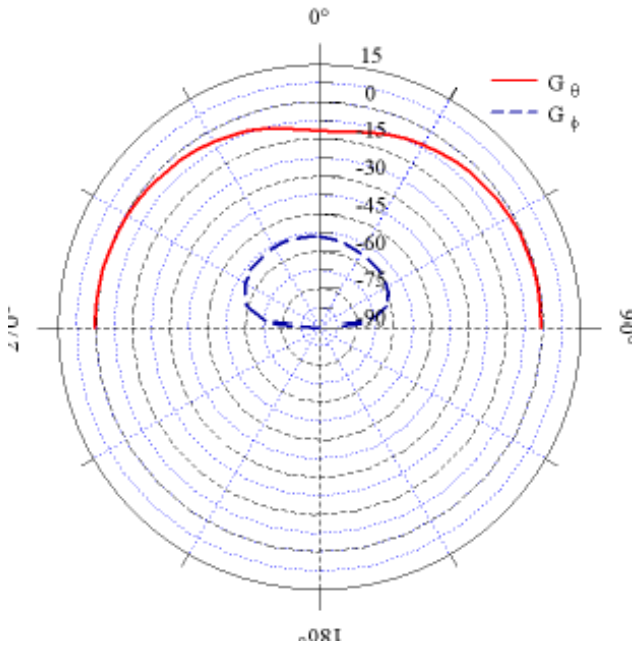

Figure 3.29: Simulated elevation plot of absolute gain along the $\phi = 0^0$ plane for configuration 1.

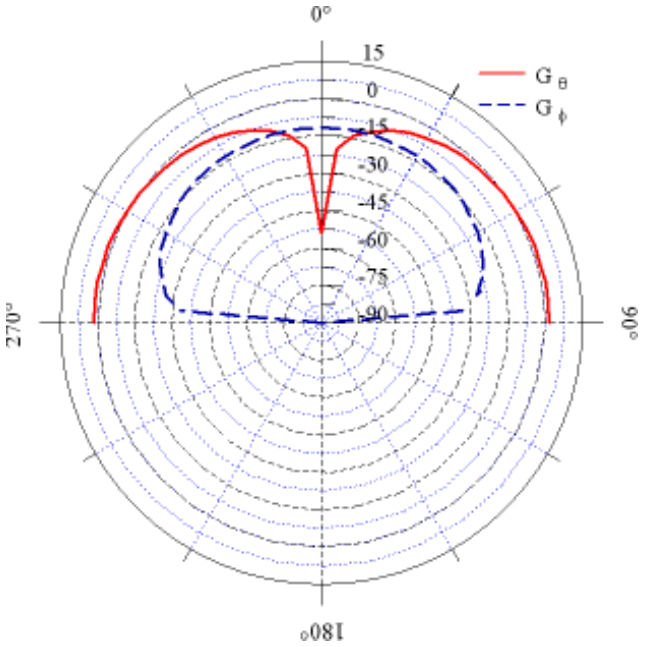

Figure 3.30: Simulated elevation plot of absolute gain along the $\phi = 90^0$ plane for configuration 1.

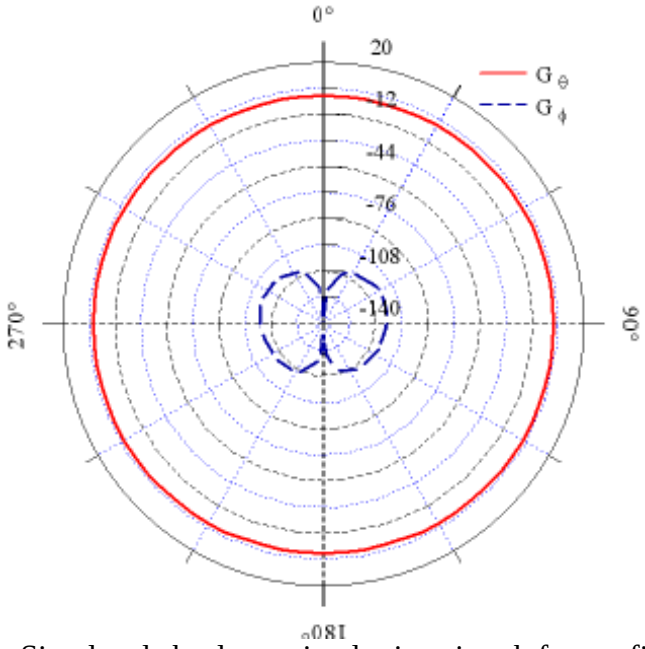

Figure 3.31: Simulated absolute gain plot in azimuth for configuration 1.

3.4.2 Simulations performed with 3.2 pF capacitance

To examine whether higher efficiencies are possible when varactors are placed in configuration 3 at lower frequencies, the same set of simulations was run but with the total capacitance changed to 3.2 pF. However, due to hardware limitations, it was impossible to run a fast sweep in HFSS and a discrete sweep with 5 MHz step size was performed instead. Simulation results of VSWR versus frequency for all three configurations are presented as Figure 3.32 and the HFSS calculated radiation efficiencies are presented as Table 3.2.

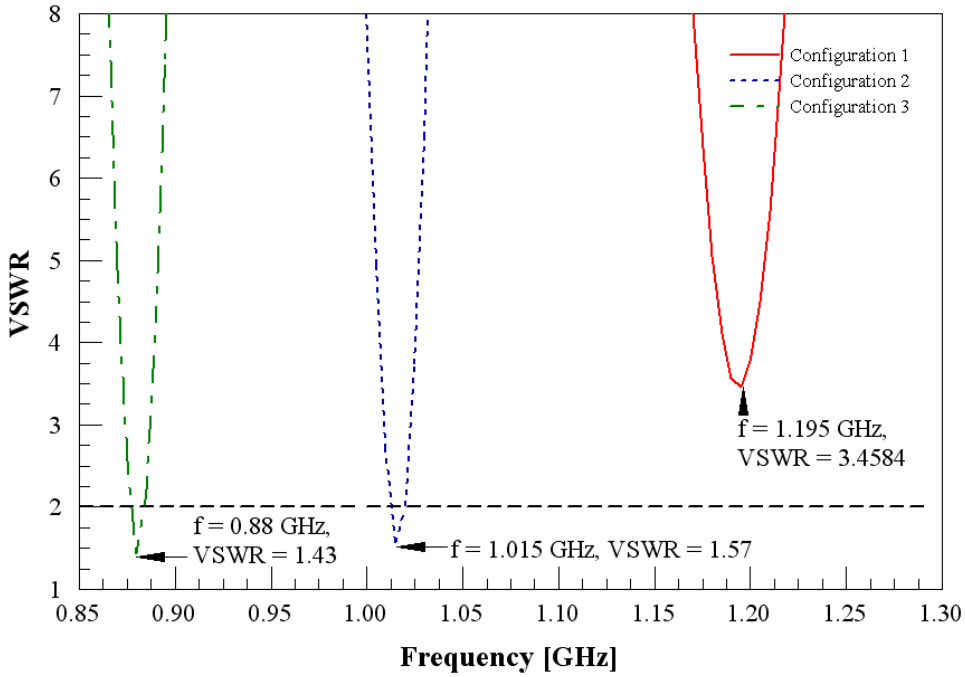

Figure 3.32: Simulated plot of VSWR versus frequency for capacitors in all three configurations with 3.2 pF capacitance.

Table 3.2: VSWR and radiated efficiency for antennas with 3.2 pF capacitance.

	Match frequency [GHz]	VSWR	Radiation efficiency
Configuration 2	1.015	1.57	1%
Configuration 3	0.88	1.43	13.9%

Examination of Figure 3.32 indicates that, similar to the previous set of simulations, a good impedance match cannot be achieved for the antenna in configuration 1. Furthermore, as in the earlier case, data in Table 3.2 indicates that the match frequency was higher in configuration 2

with poorer radiation efficiency. In addition, the gain plots for all three configurations were examined; they exhibit identical trends to those presented in Section 3.4.1 and are not presented here for brevity. Therefore, simulations performed suggest that introducing an asymmetry in antenna geometry in an electrically small antenna not only affects the match frequency [22], but also impacts radiation efficiency.

3.5 Characterization of the Reconfigurable Element

After the inductively loaded sector antenna was analyzed and configured for frequency tuning, a study of the tuning ability of the antenna was necessary. The required frequency tuning range of the antenna is very large, so determining how well the structure at this point reconfigures will govern how the problem will be addressed.

To determine the antenna's characteristics at different varactor capacitances, simulations were performed by varying the capacitance across the "lumped RLC" boundary as defined in Chapter 3. This "lumped RLC" boundary models the change in varactor capacitance for different DC bias voltage. Similar to prior simulations, an infinite ground plane was defined and a constraint was placed such that convergence occurs only when radiation efficiency changes by less than 1% on successive adaptive passes.

A diagram of the simulated antenna is provided in Figure 3.33 and simulated results of VSWR versus frequency from a fast sweep performed with a 2 MHz step size are presented in Figure 3.34. In addition, the data was plotted on a Smith chart and presented as Figure 3.35. Finally, the impedance bandwidth was determined and tabulated in Table 3.3, and HFSS calculated results for radiation efficiency and maximum gain are presented in Table 3.4.

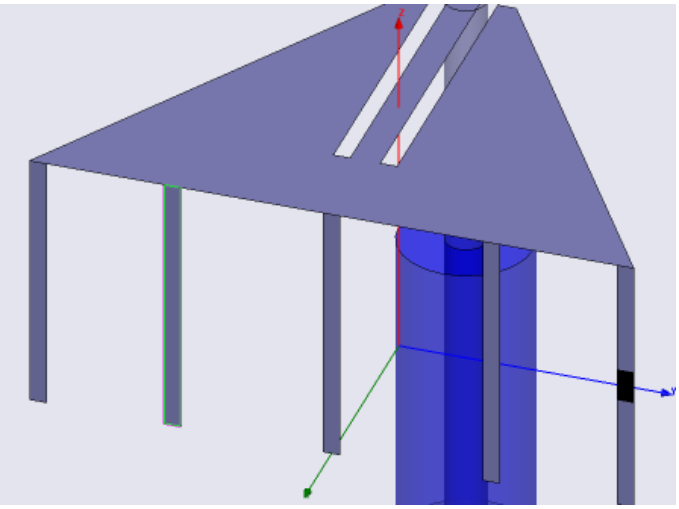

Figure 3.33: Simulated antenna with varying capacitance (Graphics from HFSS).

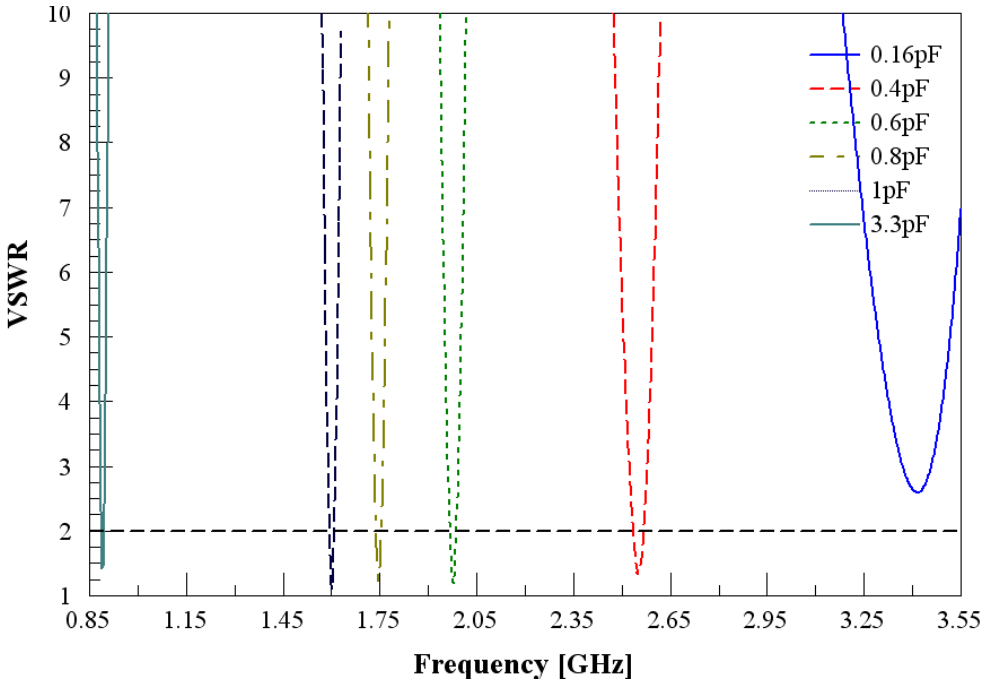

Figure 3.34: Simulated plot of VSWR versus frequency with changing capacitance values.

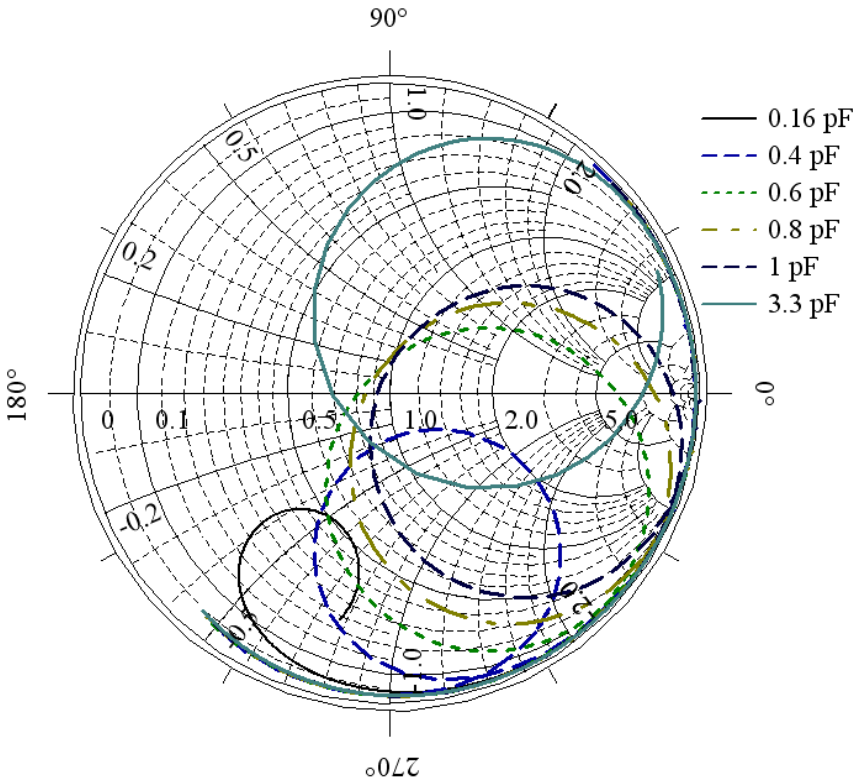

Figure 3.35: Simulated Smith chart plot from 0.85 to 3.55 GHz with changing capacitance values.

Table 3.3: Antenna impedance match and bandwidth.

Capacitance [pF]	Match frequency [GHz]	VSWR	Bandwidth [MHz]
0.16	3.416	2.59	0
0.4	2.552	1.32	32
0.6	1.978	1.18	18
0.8	1.746	1.18	14
1	1.602	1.09	14
3.3	0.89	1.41	10

Table 3.4: Antenna efficiency and gain.

Capacitance [pF]	Match frequency [GHz]	Radiation efficiency	Gain [dBi]
0.16	3.416	90%	5.109
0.4	2.552	66%	3.16
0.6	1.978	47%	0.657
0.8	1.746	37.5%	-0.968
1	1.602	30%	-2.45
3.3	0.89	16%	-10

Examination of Figure 3.34 and Table 3.3 indicates that by varying the capacitance between 0.4 and 3.3 pF, a good impedance match with at least 10 MHz bandwidth is achievable from 0.89 GHz to 2.552 GHz, encompassing the full range of application frequencies except for WiMAX at 3.5 GHz. The simulation results indicate that at frequencies of 3.42 GHz and above, the impedance match is poor and therefore additional analysis needs to be performed in order to properly realize the 3.5 GHz band.

Furthermore, analysis of Figure 3.35 indicates that as varactor capacitance increases, the total antenna impedance becomes more inductive. This increase in the antenna's overall inductance can be explained by how the currents present on the antenna change with varactor capacitance. For high capacitance values (lower frequencies) the capacitor effectively reduces the reactance present on the corner inductive load; this reduction in reactance causes more current to be "pulled" to the corner of the antenna, increasing the effective length of the antenna and causing current to be concentrated to only two of the five inductive loads. This in turn increases the overall inductance of the structure because only two of the loads are effectively contributing to the antenna impedance. This result can be shown in Figure 3.36 for the varactor capacitance equal to 3.3 pF at a frequency of 0.89 GHz.

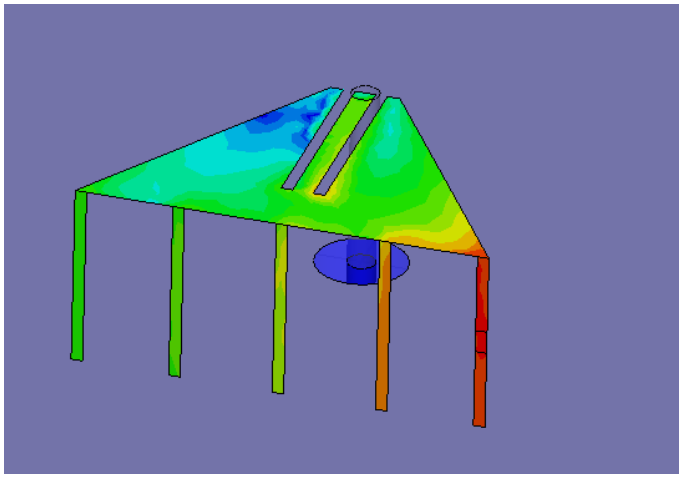

Figure 3.36: Surface current magnitude for antenna with varactor equal to 3.3 pF (Graphics from HFSS).

Finally, data in Table 3.4 indicates that antenna radiation efficiency ranges from 16% to 90% when measured from 0.89 GHz to 3.5 GHz, respectively. Both antenna gain and radiation efficiency increase with match frequency as expected due to the fundamental limits associated with electrically small antennas.

Even though additional tuning is required to achieve a good impedance match at 3.5 GHz, it is unlikely that this is obtainable with a single varactor. Since a capacitance of smaller than 0.16 pF (C_{low}) is needed to achieve an impedance match at 3.5 GHz and a capacitance of 3.3 pF (C_{high}) is required for an impedance match at 0.89 GHz, the tuning ratio C_{high}/C_{low} is at least 20.6. This is unachievable since commercially available varactors typically do not have tuning ratios above 11 [23] for such small tuning capacitance values. Furthermore, commercially available varactors that tune to 0.16 pF and below are incredibly difficult to manufacture because the typical package capacitance of most varactor diodes is on the order of 0.1 pF [24]. For frequency reconfiguration from 0.89 to 2.55 GHz, however, a tuning ratio of 8.25 is necessary, and a candidate varactor is Microsemi's GC15008 varactor, which is able to tune from 0.4 pF to 4.4 pF [24].

3.6 Results

In summary, the modifications performed on the electrically small, inductively loaded, dual sector antenna for frequency reconfiguration are detailed. These include antenna miniaturization and inclusion of additional vertical inductive loads. Furthermore, a simple bias network was proposed and the effect of varactor placement on antenna performance in both the inductive feed and the vertical inductive loads was determined. Consequently, the antenna as proposed in configuration 3 is shown to have the most promise for frequency reconfiguration, and simulations are performed to determine its response to different capacitances.

It was shown that the previously designed inductively loaded sector antenna with a single varactor placed at a corner inductive load indeed produced an antenna that could frequency reconfigure from 0.89 to 2.5 GHz while maintaining acceptable gain and efficiency figures.

However, in order to achieve full frequency tuning from 0.9 GHz to 3.5 GHz, additional changes to the antenna's structure are made in Chapter 5 to increase the structure's sensitivity to changes in varactor capacitance.

Chapter 4

GROUND PLANE SIZE EFFECTS

4.1 Effect of Ground Plane Size on Antenna Performance

When performing simulations for electrically small antennas, it is often helpful to assume an infinite ground plane so that just the behavior of the antenna element can be analyzed. However, for practical designs, especially when dealing with electrically small antennas, an analysis of how the antenna performs with respect to different ground plane sizes is necessary. When the ground plane on which the antenna is mounted becomes small enough to not be considered infinite, it can be difficult to determine without careful observation the true radiation source associated with the design. Too often, it is the ground plane itself and not the antenna element that is providing the main source of radiation [25].

Most of the previous studies and simulations for this thesis were performed utilizing an infinite ground plane, which does not provide practical operating performance of the antenna on realistic platforms. A simulation study was performed using HFSS to observe how the antenna behaved when the ground plane length was reduced from a standard 65 mm to 25 mm in steps of 10 mm.

Image theory predicts that as the size of the ground plane decreases from infinity, the antenna becomes less similar to a monopole over an infinite ground plane, and more akin to a dipole. Also, as the ground plane size is reduced, the ground plane becomes a part of the antenna structure, which then contributes to the impedance match of the antenna. Figures 4.1 and 4.2 show the difference in surface current magnitudes between the 25 mm and 65 mm ground plane sizes. As predicted, as the ground plane decreases in size (Figure 4.1) the currents present on the ground plane increase significantly. The higher current density present on the ground plane signals that it is now a part of the radiating structure. Conversely, for the larger ground plane size (Figure 4.2), the currents present on the ground plane are confined to the area immediately surrounding the antenna element, illustrating that the antenna itself is the main source of radiation in this case.

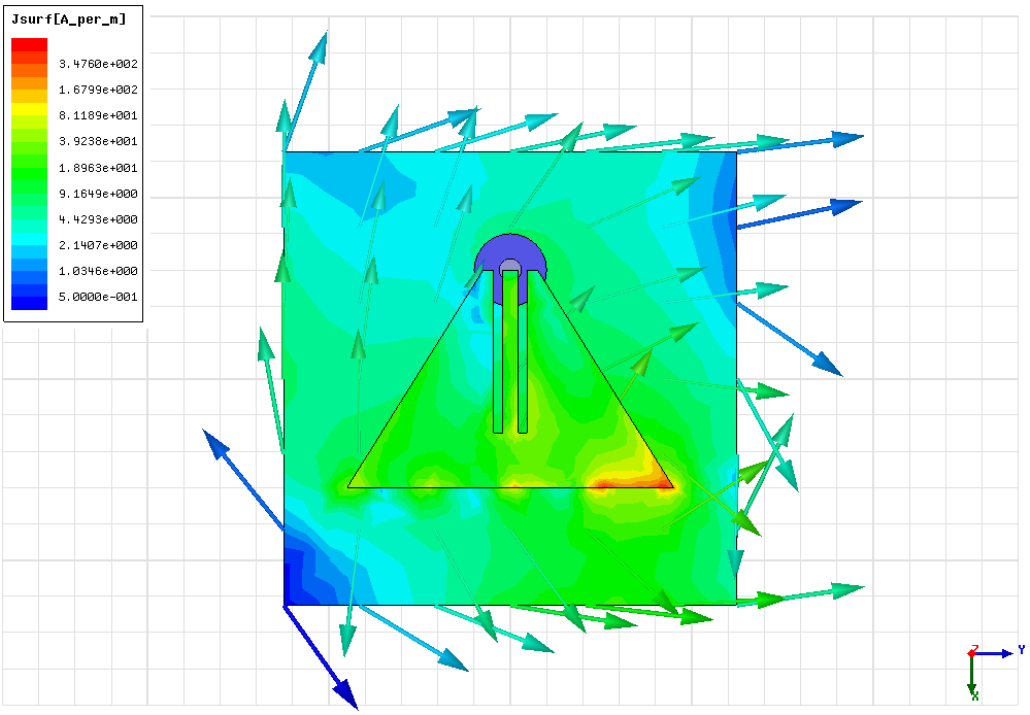

Figure 4.1: Surface currents with 25 mm ground plane size (Graphics from HFSS).

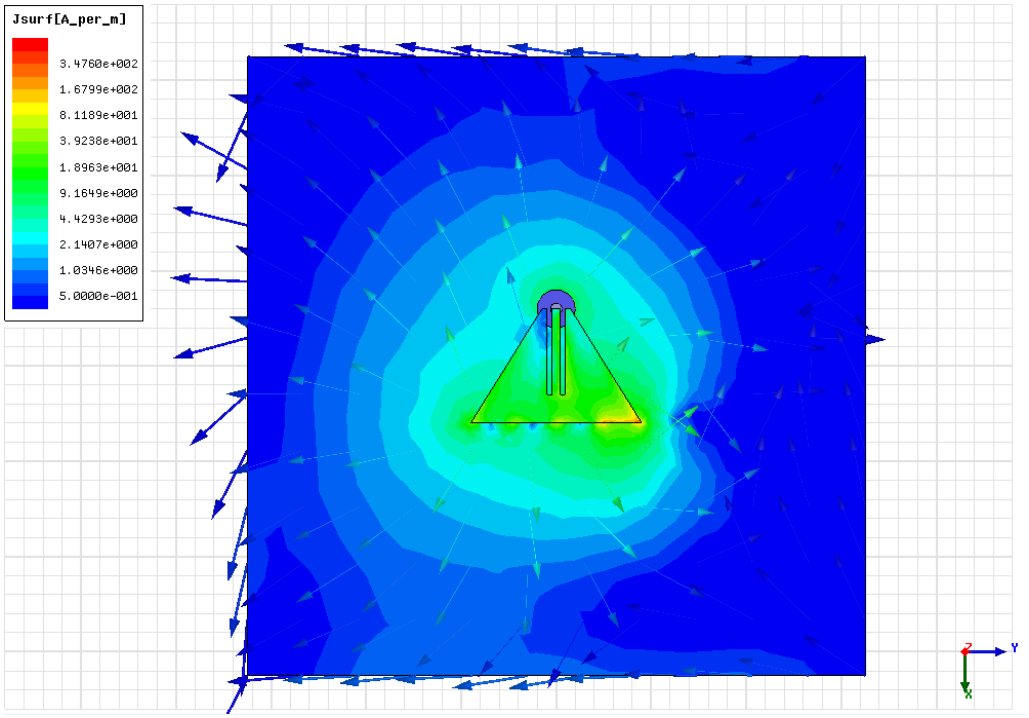

Figure 4.2: Surface currents with 65 mm ground plane size (Graphics from HFSS).

The simulations when examining VSWR vs. frequency indicated a phenomenon where the impedance match of the antenna for the small ground plane was better than that of the larger ground planes. The phenomenon was observed at most frequencies over the tuning range, but was the most prevalent in the high frequency (0.16 pF varactor) range case. In general, these effects were most pronounced for the case where the varactor capacitance was smallest (providing the smallest conductance), which resulted in more spreading of the current as compared to larger varactor values. That is, cases with larger varactor values also exhibited some of these characteristics, but not to the extent of the cases with smaller values. Therefore, in order to determine the origin of these effects, a study was performed considering the case where this disparity was the greatest.

For the simulation of the corner varactor at 0.16 pF, both the VSWR plot (Figure 4.3) and the Smith chart (Figure 4.4) show that the smaller ground planes (25 mm and 45 mm) give a slightly better impedance match than the larger ground planes (65 mm, 75 mm, and 85 mm). The improvement between large and small ground planes, even in this extreme case, is fairly modest (a difference between a minimum VSWR is from ~2.6 for the largest ground plane size to ~1.9 for the second smallest ground plane size).

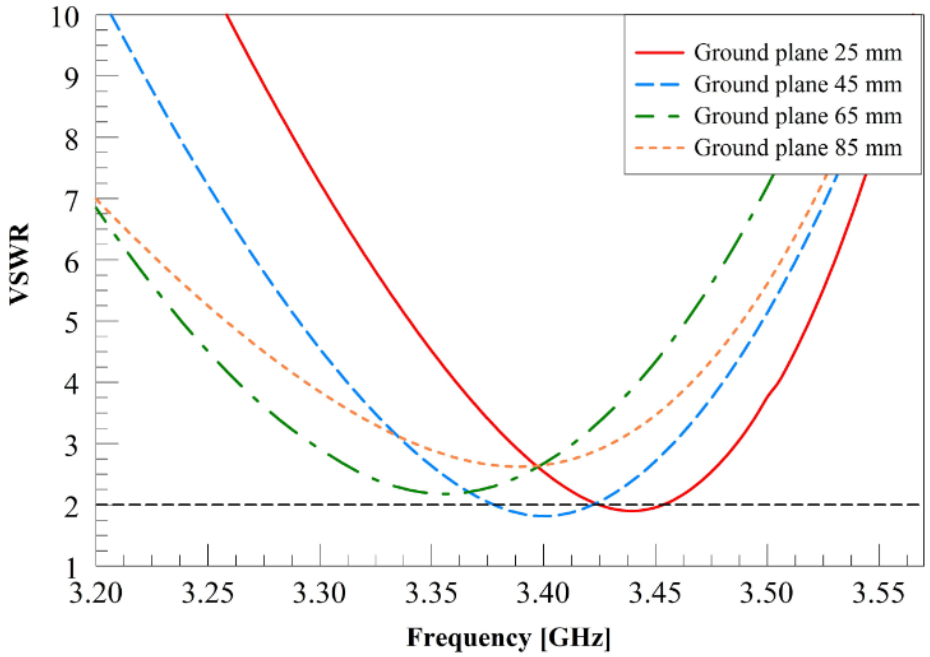

Figure 4.3: Simulated plot of VSWR versus frequency with changing ground plane size.

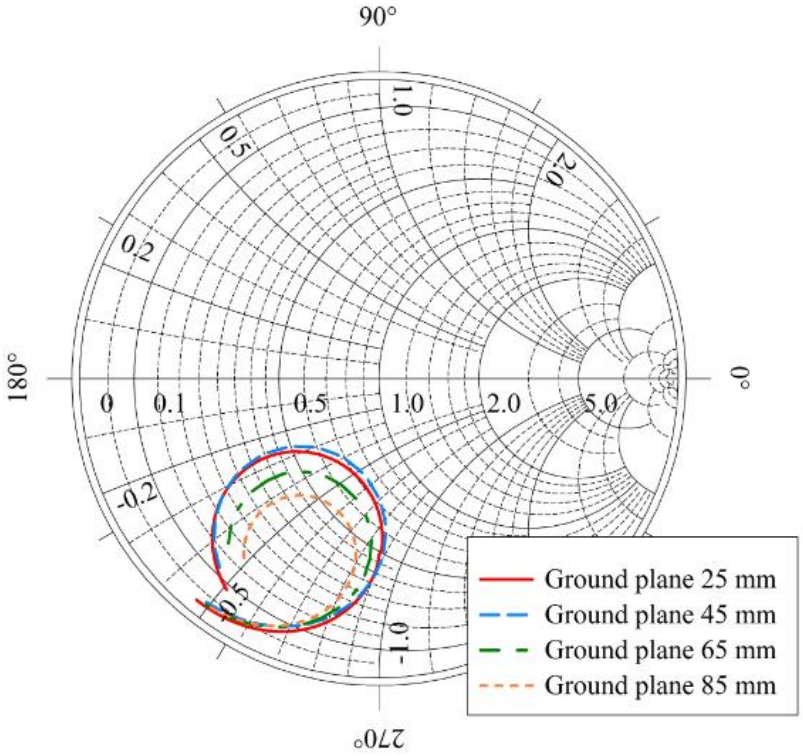

Figure 4.4: Simulated Smith chart plot from 3.2 to 3.575 GHz with varying ground plane size.

Examination of the surface current distribution of the different ground plane sizes as well as the radiation patterns of the antenna shows a few noticeable results. The largest portion of the current on the structure is being pulled through the inductive load that contains the varactor. This is no surprise because when the impedance created by the capacitance is small in comparison with the impedance presented by the inductance of the load, it creates a lower impedance path. For the 25 mm case, however, the ground plane itself is a significant part of the radiating structure and therefore helps maintain a better impedance match. The currents on the ground plane also contribute to the radiation effects of the overall antenna structure, accounting for the difference in impedance match observed in Figure 4.4.

4.2 Pattern Considerations

Along with the analysis of how the impedance match changes with ground plane size, observing how the radiation pattern of the antenna varied as a function of ground plane size was also desired. As the ground plane size decreases, a shift in the pattern of the antenna element can be observed. The major factor in the shift is due to the fact that when the ground plane approaches the size of the antenna, the entire antenna behaves as a dipole instead of a monopole. Figures 4.5 -4.7 are simulated gain plots for both the 25 mm and 65 mm ground plane sizes. Gain Θ and gain Φ are represented at 3.43 GHz for the 25 mm ground plane and 3.36 GHz for the 65 mm ground plane.

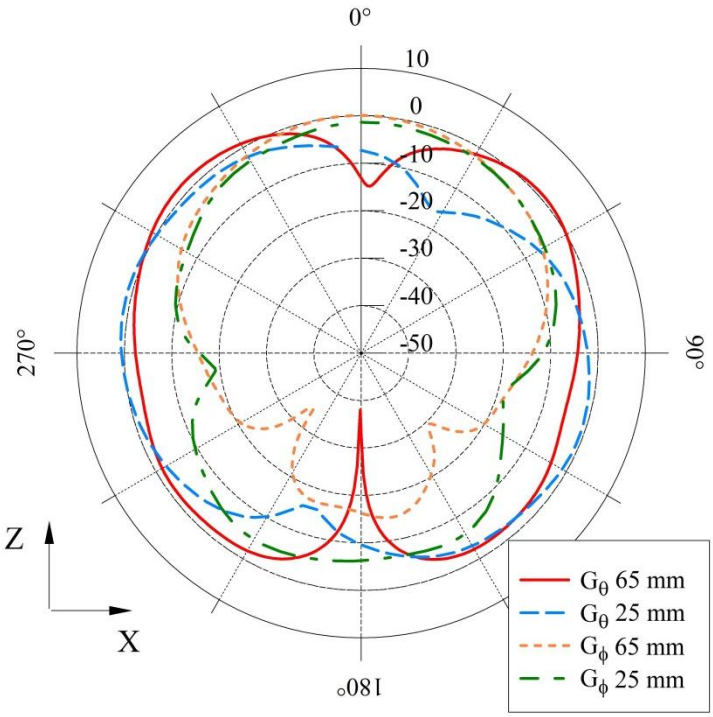

Figure 4.5: Simulated antenna gain patterns on the $\Phi = 0^0$ plane at various ground plane sizes. Patterns are taken at 3.43 GHz for a 25 mm wide ground plane and 3.36 GHz for a 65 mm ground plane.

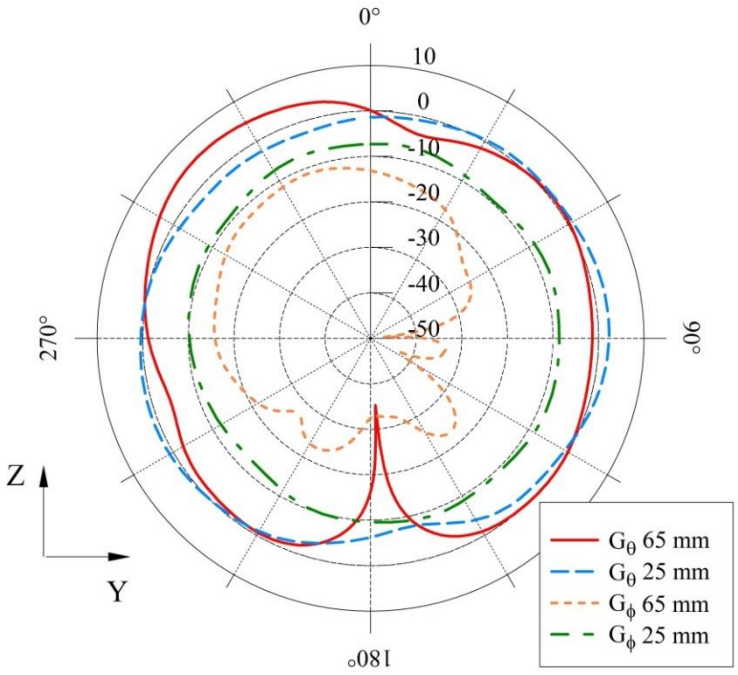

Figure 4.6: Simulated antenna gain patterns on the $\Phi = 90^0$ plane at various ground plane sizes. Patterns are taken at 3.43 GHz for a 25 mm wide ground plane and 3.36 GHz for a 65 mm ground plane.

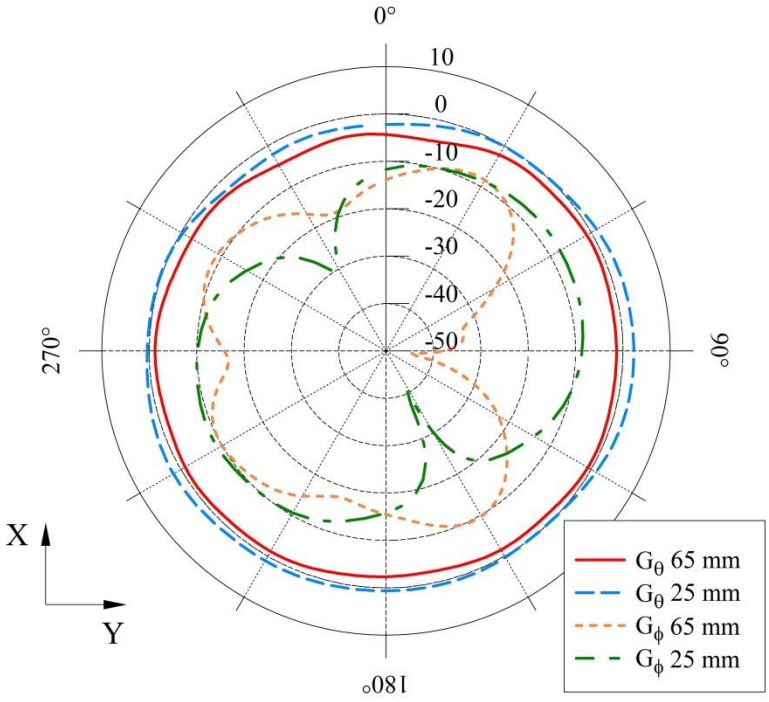

Figure 4.7: Simulated antenna gain pattern on the azimuth. Patterns are taken at 3.43 GHz for a 25 mm wide ground plane and 3.36 GHz for a 65 mm ground plane.

The cut planes reveal that, as hypothesized, the 25 mm ground plane pattern behaves more as a tilted dipole than a monopole over a ground plane. Likewise, the 65 mm case shows a pattern more consistent with a monopole, though its pattern is slightly tilted due to the off-center feeding and asymmetric currents on the antenna structure.

Another useful visualization to understand the different ground plane patterns is to examine the gain plotted as a three-dimensional figure. Figures 4.8 and 4.9 show G_Θ for both the 25 mm and 65 mm cases at 3.43 and 3.36 GHz, respectively. Again, the difference between the monopole type pattern of the larger ground plane and the dipole "doughnut" pattern of the smaller ground plane are easily observed.

The previous study on ground plane sizes was performed only with the antenna described in Chapter 3. The effect of the ground plane size on the final antenna design is detailed in Chapter 8.

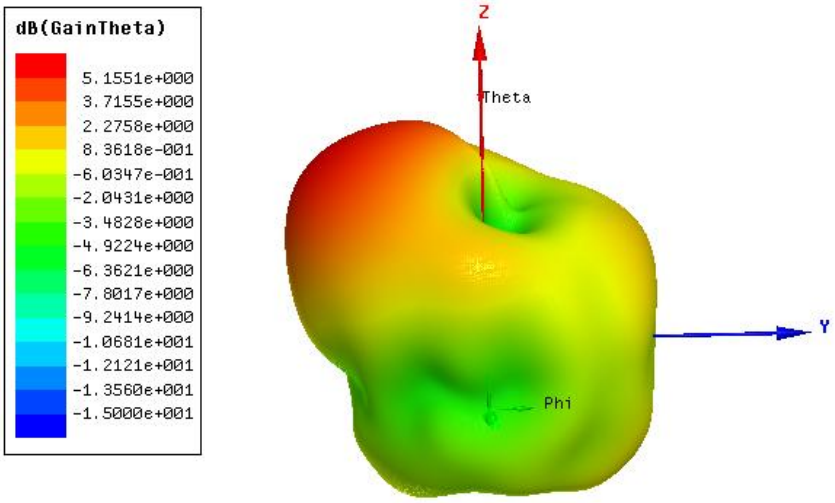

Figure 4.8: Simulated G_Θ at 3.36 GHz with 65 mm ground plane (Graphics from HFSS).

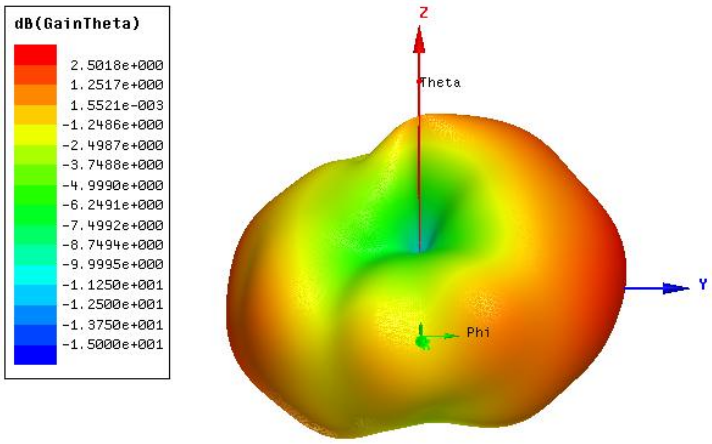

Figure 4.9: Simulated G_Θ at 3.43 GHz with 25 mm ground plane (Graphics from HFSS).

Analysis of how the antenna element performs relative to ground plane size yields a clearer understanding of how the antenna can be practically situated. In light of these results on the effects of ground planes, the earlier justifications for the antenna design stand. Knowing that at small ground plane sizes the antenna behaves much more like a dipole will greatly enhance the knowledge of where the radiation energy is going. The understanding gained from the study can be used to modify the base design so that the insertion of the varactors results in tuning over the desired range. Since the effects of ground plane size on radiation patterns are predictable, the effects can also be taken into account once a package size is specified.

Chapter 5

TUNING RANGE STUDY

5.1 Improving Maximum Antenna Tuning Range

The end of Chapter 3 described an inductively loaded sector antenna design that could continuously tune from 900 MHz to 2.4 GHz utilizing a varactor ranging from 3.3 pF to 0.4 pF. Achieving this amount of frequency tuning is impressive; however, this design does not address the full desired tuning range of the project (900 MHz to 3.5 GHz). Because of this, a study to analyze the further modifications needed to achieve the full tuning range was necessary.

A series of studies was performed on the antenna structure to determine the best possible way to increase the frequency tuning range of the antenna. Parametric studies performed on the antenna's geometry noted that certain structural changes produced shifts in frequency and increased performance over certain frequency ranges. After observing closely which changes held the best possibility to increase the frequency range, three different geometric changes were chosen to study how they could be used to increase the antenna's tuning range. The three studies are presented below and concern the antenna's sector tilt (cant angle), sector back edge length, and sector height above the ground plane.

5.1.1 Cant angle study

The antenna sector tilt, or cant angle as depicted in Figure 5.1, was a design feature that was removed in the initial geometry modifications of the antenna design. Originally, this angle was used as a tuning mechanism in the electrically small, inductively loaded, dual-sector antenna to control the capacitance between the two antenna sectors in order to increase the antenna's bandwidth [3], [4]. However, since the goal of this project is to achieve frequency reconfiguration and not maximum bandwidth, the cant angle was originally removed to ease antenna fabrication.

Simulations were performed in HFSS incorporating the cant angle back into the antenna geometry to determine its potential in increasing the overall tuning range. Figure 5.1 shows a side view of the antenna indicating the cant angle, and Figures 5.2 and 5.3 present VSWR and the input impedance of the antenna in the high frequency range (3.1 to 3.7 GHz and varactor capacitance equal to 0.16 pF), respectively. The cant angle (Ψ) was varied from 0^o to 20^o in both Figures.

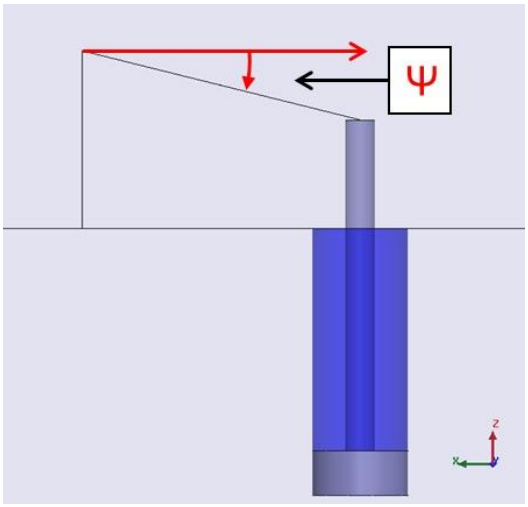

Figure 5.1: Side view of antenna indicating sector cant angle (Graphics from HFSS).

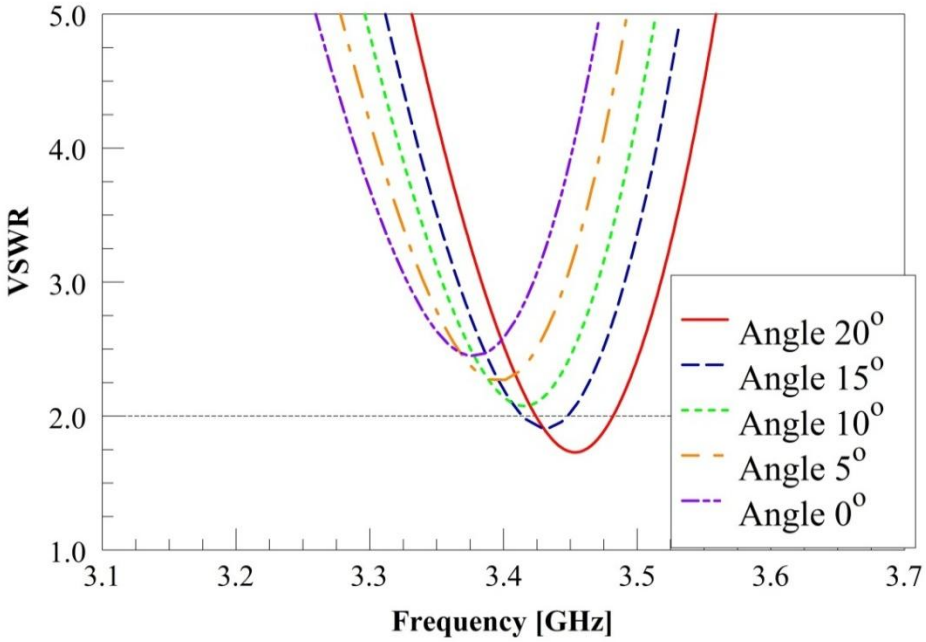

Figure 5.2: Simulated plot of VSWR versus frequency of antenna with capacitor at 0.16 pF and varying cant angles.

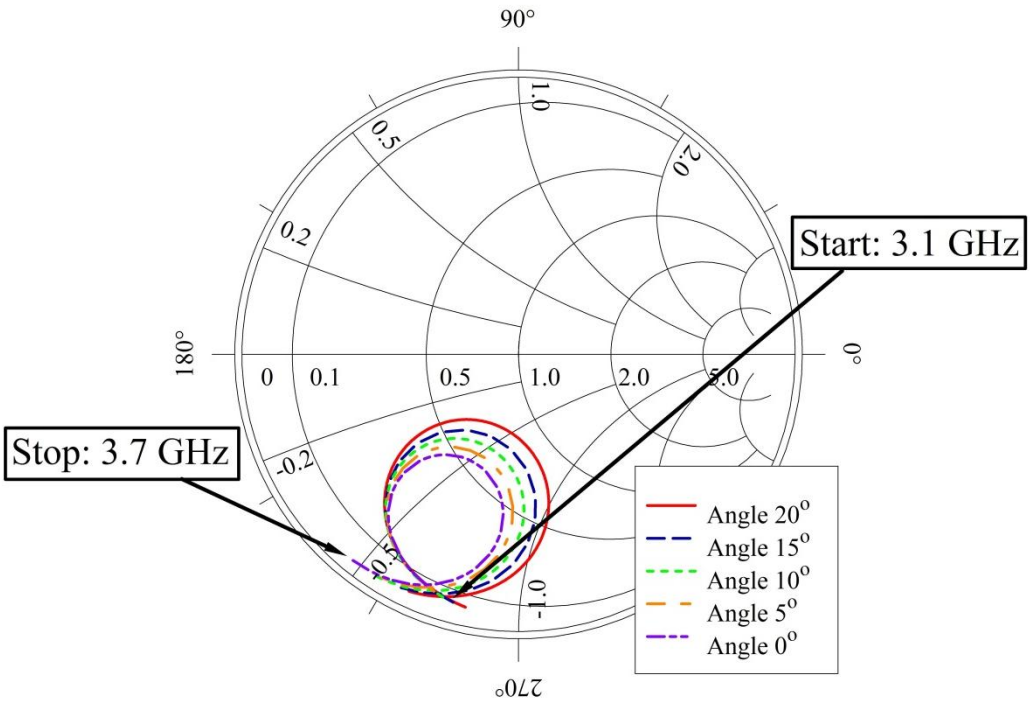

Figure 5.3: Simulated Smith chart plot from 3.1 to 3.7 GHz of antenna with capacitor at 0.16 pF and varying cant angles.

Figures 5.2 and 5.3 indicate an upward frequency shift and improvement in the antenna's impedance match at the higher frequencies as the cant angle is increased. In addition, at a cant angle of 15^{o} - 20^{o}, the antenna achieved a VSWR < 2 within the simulated frequency range, demonstrating that this method does allow for an impedance match for all desired frequencies. The addition of the sector tilt has the effect of making the antenna structure slightly shorter in front-to-back length, thus decreasing the total antenna capacitance and making the antenna appear more inductive. Consequently, the radius of the impedance circles on the Smith chart increase, resulting in both the observed frequency shift and improvement in impedance match as the angle increases.

In addition to the high frequency range, the impedance characteristics at the low frequency range (0.86 to 0.92 GHz and varactor capacitance equal to 3.3 pF) were examined while the cant angle was again varied from 0^{o} to 20^{o}. Figures 5.4 and 5.5 present the simulated results.

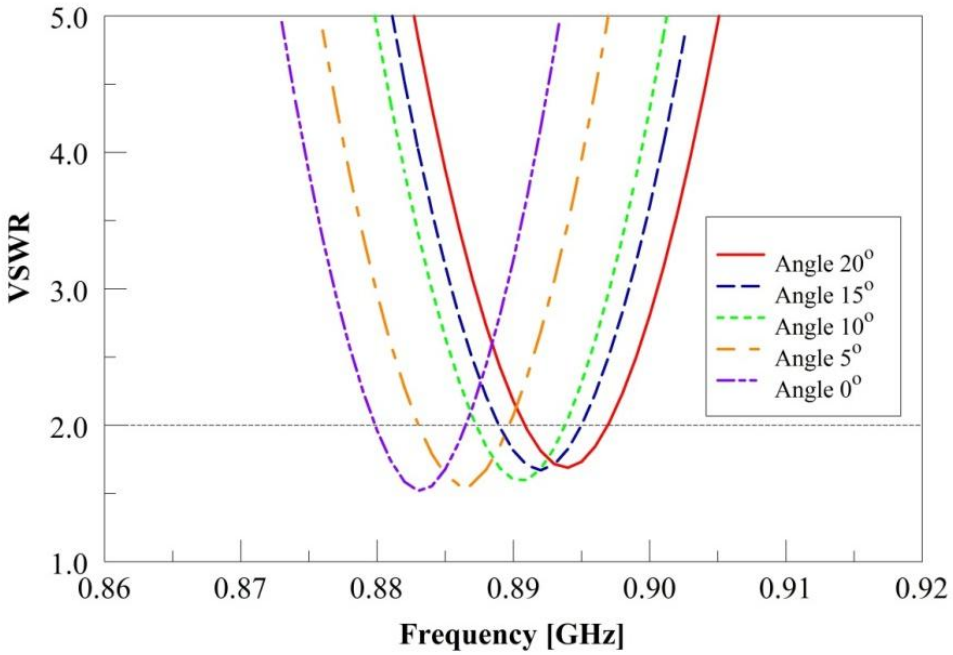

Figure 5.4: Simulated plot of VSWR versus frequency of antenna with capacitor at 3.3 pF and varying cant angles.

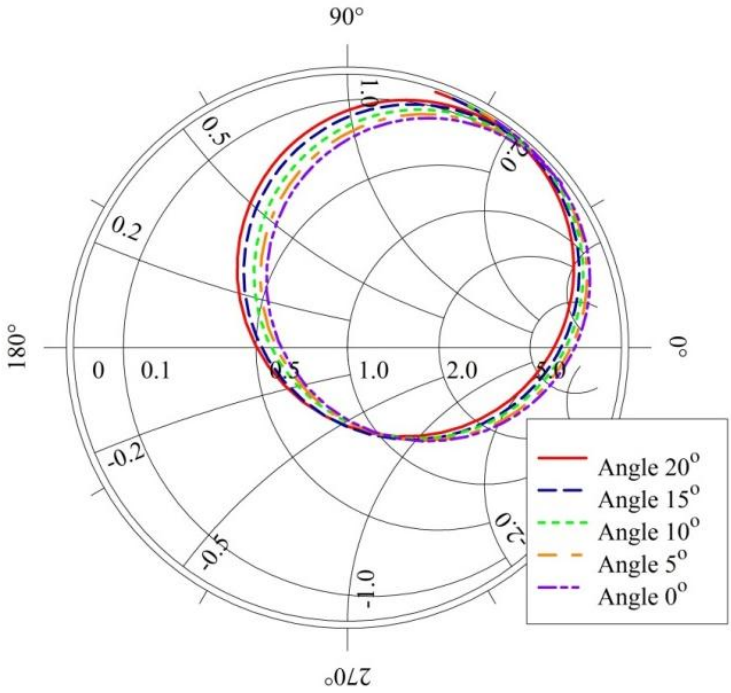

Figure 5.5: Simulated Smith chart plot from 0.86 to 0.92 GHz of antenna with capacitor at 3.3 pF and varying cant angles.

Comparisons of Figures 5.2 to 5.5 indicate that, unlike the higher frequency range, the antenna's impedance match decreases as the sector tilt angle increases at the low frequency range. This reduction in VSWR match and frequency shift can be explained by examining the Smith chart in Figure 5.5. While the sizes of the Smith chart circles stay relatively constant with changes in sector tilt, the variation in sector length introduced by the addition of the cant angle produces a frequency shift that moves the impedance circle away from the center of the Smith chart. With this decrease in VSWR, the bandwidth of the low frequency range is decreased to approximately 5 MHz, approximately half of the 10 MHz minimum bandwidth requirement specified for the project. Finally, Table 5.1 summarizes the simulated results pertaining to tuning range and cant angle, indicating that the tuning impedance match range increases to 2.56 GHz at a sector tilt of 20 degrees.

Table 5.1: Overall tuning range improvement with increasing cant angle. (Denotes unacceptable instantaneous bandwidth.)

Cant angle [degrees]	Maximum tunable range [GHz]
0	2.5 (0.88-3.38)
5	2.51 (0.88-3.39)
10	2.52 (0.89-3.41)
15	2.54 (0.89-3.43)
20	2.56 (0.89-3.45)

Even though the reintroduction of the cant angle increases the impedance matched tunable range, for the angles that deliver a good impedance match at 3.5 GHz, an unacceptable instantaneous bandwidth is observed at 900 MHz. Also, the antenna requires a varactor that can change its capacitance from 0.16 pF to 3.3 pF, a capacitance ratio of over 20. Since varactors typically have a capacitance ratio of 11 or less, the improvement in tuning range achieved by adjusting the sector cant angle is unachievable with the current varactor diodes on the market.

5.1.2 Sector back edge study

Preliminary parametric studies with the antenna structure indicated that varying the back edge width of the antenna resulted in a frequency shift that did not degrade the impedance match over the frequency range. These previous studies were used to determine the original back edge length of the antenna of 18 mm. However, it was unknown if changing the width of the back edge would have any effect on the antenna's sensitivity to alterations in capacitance and thus an improvement in tuning range. For this study, the back edge width was varied in the manner depicted in Figure 5.6 to determine its effects on the frequency agility of the antenna.

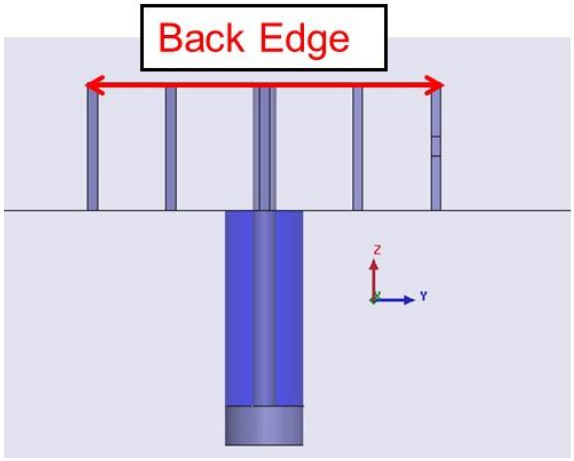

Figure 5.6: Rear view of antenna structure indicating variations to the width of the back edge (Graphics from HFSS).

Figures 5.7 and 5.8 depict the impedance characteristics of the antenna with varactors at 0.4 pF, whereas Figures 5.9 and 5.10, respectively, plot the VSWR and Smith chart of the antenna with varactors at 3.3 pF. Shortening the back edge width shrinks the length of the current path on the structure at all frequencies. Because of this reduction in the current path length, Figures 5.7 and 5.9 indicate an upward shift in match frequency while the impedance match remains relatively constant for both capacitances. This frequency shift manifests itself in the impedance plots as rotations of the impedance circles on the Smith charts as illustrated in Figures 5.8 and 5.10.

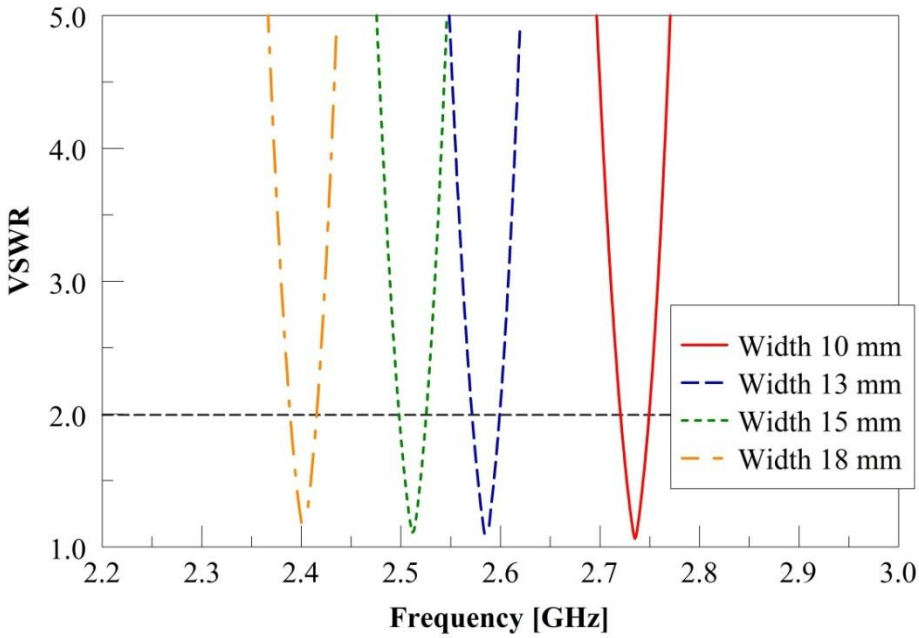

Figure 5.7: Simulated plot of VSWR versus frequency with capacitor at 0.4 pF and varying back edge width.

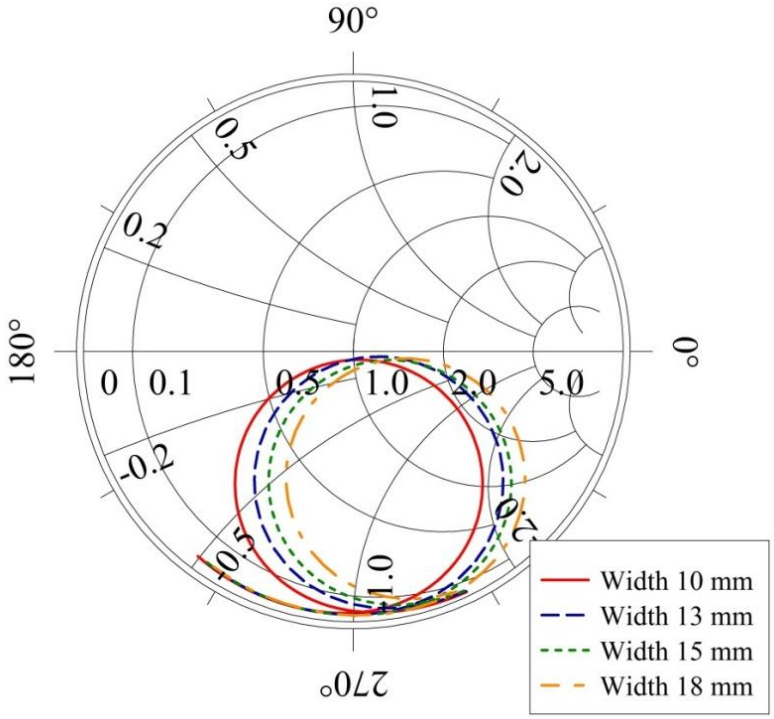

Figure 5.8: Simulated Smith chart plot from 2.2 to 3 GHz with capacitor at 0.4 pF and varying back edge width.

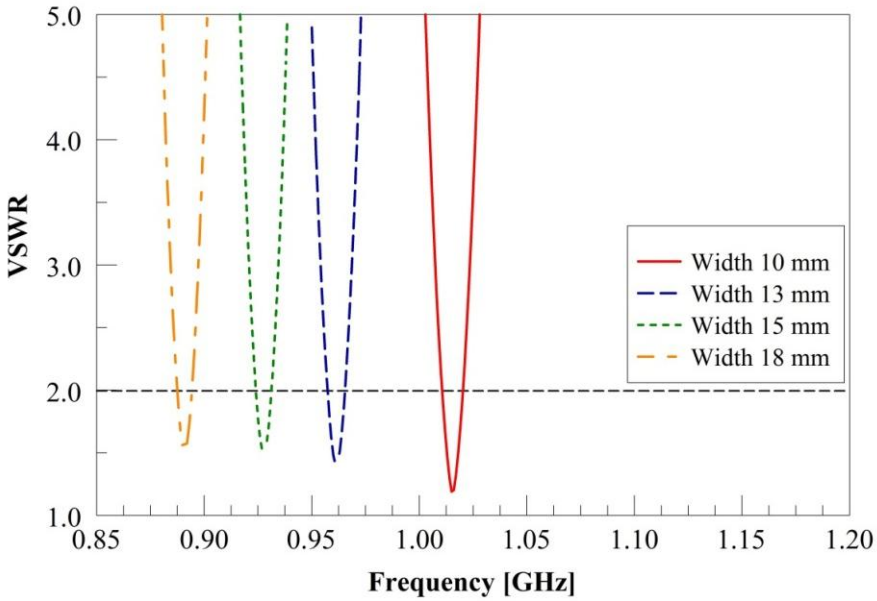

Figure 5.9: Simulated plot of VSWR versus frequency with capacitor at 3.3 pF and varying back edge width.

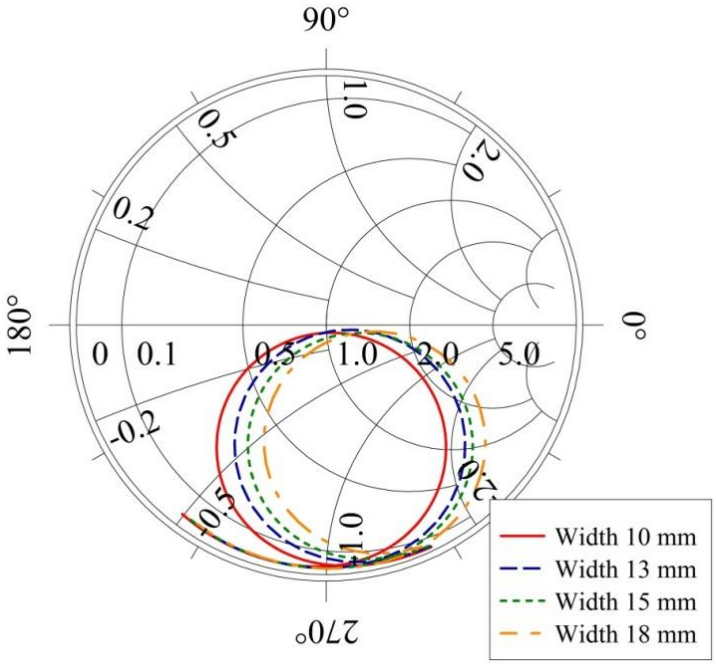

Figure 5.10: Simulated Smith chart plot from 0.8 to 1.2 GHz with capacitor at 3.3 pF and varying back edge width.

It is worthwhile to note, however, that in addition to the frequency shift, varying the width of the back edge changes the maximum tuning range of the antenna. In fact, the smaller the back edge width, the more sensitive the structure becomes to alterations in capacitance. The results of this sensitivity are summarized in Table 5.2. It is shown that as the back edge decreases, the tuning range of the antenna increases. As a result of this finding, varying the back edge width is a good candidate for increasing the maximum tuning range of the antenna.

Table 5.2: Overall tuning range improvement with decreasing back edge width.

Back Edge [mm]	Maximum Tunable Range [GHz]
10	1.72 (1.02 - 2.74)
13	1.62 (0.96 - 2.58)
15	1.58 (0.93 - 2.51)
18	1.51 (0.89 - 2.40)

5.1.3 Sector height study

Finally, variations to the antenna sector height were investigated as a means to improve the antenna's frequency agility. Similar to changing the width of the sector's back edge, prior work indicates that changing the sector height produces a frequency shift while maintaining constant VSWR match and bandwidth. Consequently, the sector height was chosen as another possible mechanism to increase the antenna's sensitivity to changes in capacitance. Figure 5.11 demonstrates how the sector height was varied for this study in simulation. Figures 5.12 and 5.13 present the impedance characteristics with varying height with 0.4 pF capacitance, and Figures 5.14 and 5.15, respectively, plot the VSWR and input impedance of the antenna with 3.3 pF capacitance.

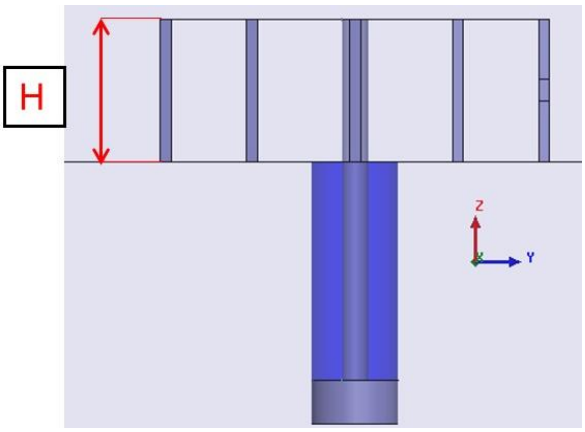

Figure 5.11: Rear view of antenna structure with changing sector height (Graphics from HFSS).

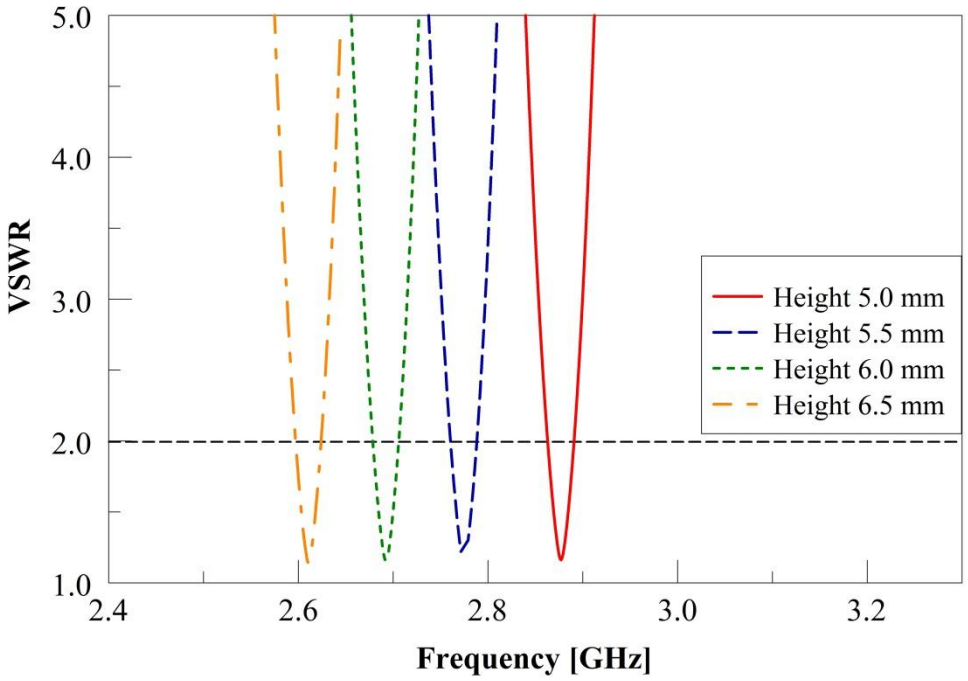

Figure 5.12: Simulated plot of VSWR versus frequency with capacitor at 0.4 pF and varying height.

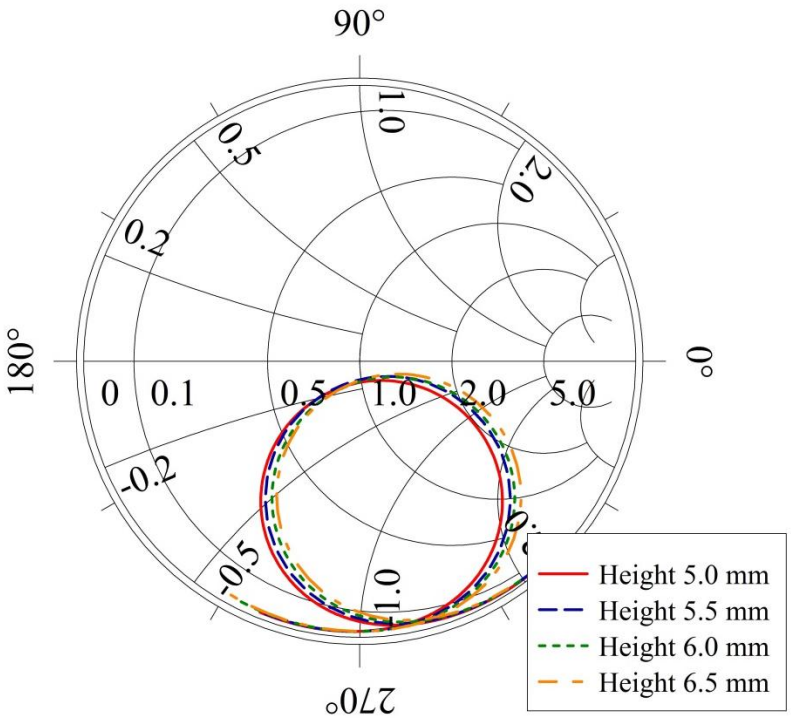

Figure 5.13: Simulated Smith chart plot from 2.4 to 3.4 GHz with capacitor at 0.4 pF and varying height.

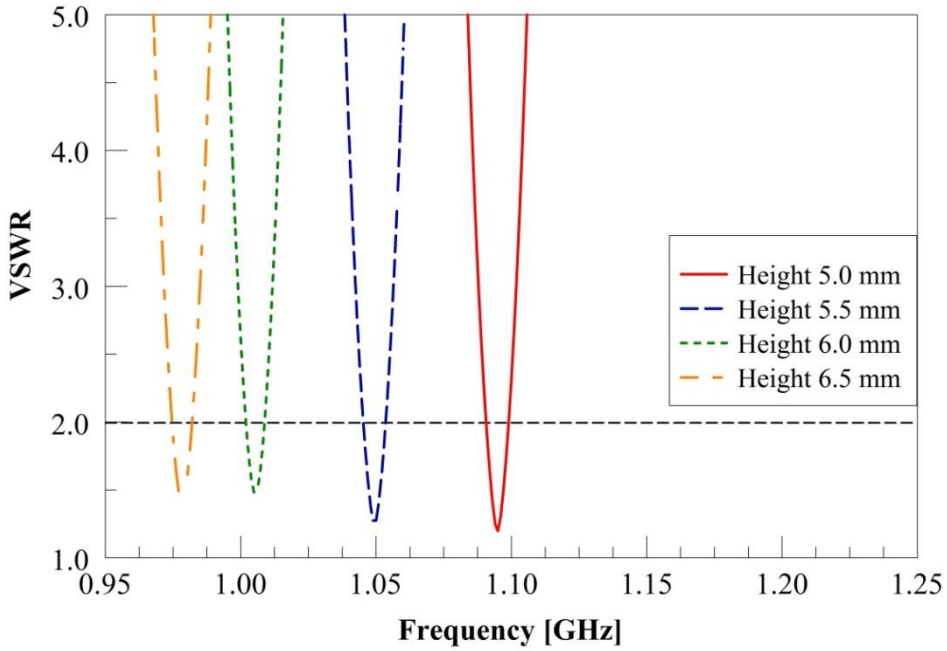

Figure 5.14: Simulated plot of VSWR versus frequency with capacitor at 3.3 pF and varying height.

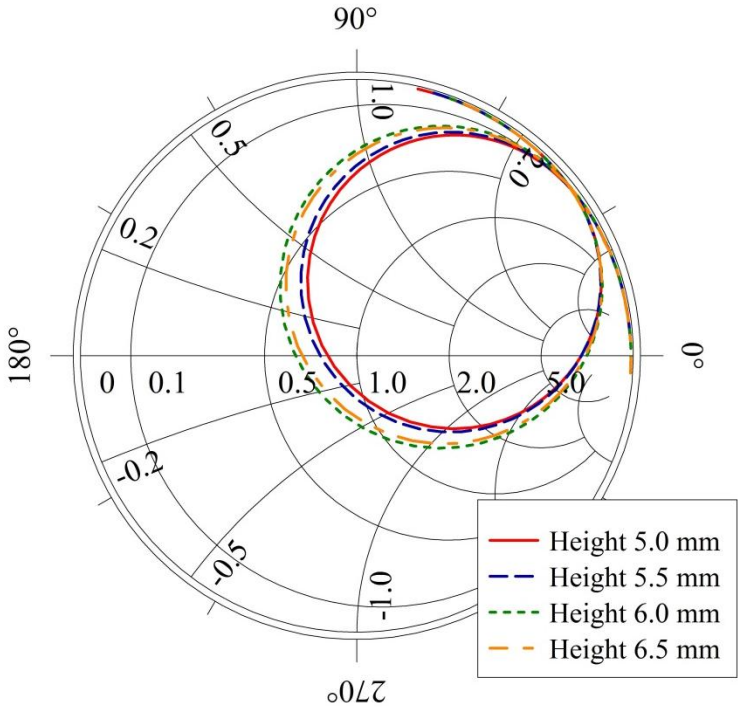

Figure 5.15: Simulated Smith chart plot from 0.95 to 1.25 GHz with capacitor at 3.3 pF and height.

Examination of Figures 5.12 to 5.15 indicate that reducing the height of the sector with respect to ground plane decreases the antenna's electrical size and results in an upward shift in the frequency of operation. In addition, the VSWR match and bandwidth remain constant in both the high and low frequency ranges. However, as with the back edge test, the observed frequency shift is not linear, resulting in an increase to the antenna's tuning range. Table 5.3 summarizes the changes in tuning range with decreasing sector height.

Table 5.3: Overall tuning range improvement with decreasing sector height.

Sector Height [mm]	Maximum Tunable Range [GHz]
5.0	1.81 (1.10 - 2.91)
5.5	1.75 (1.05 - 2.80)
6.0	1.72 (1.00 - 2.72)
6.5	1.66 (0.98 - 2.64)

5.2 Single Varactor Maximum Tuning Design

A single varactor maximum tuning design (SVMTD) was developed using the results of the previous three studies. This design was modified for maximum tuning range while maintaining constant VSWR match and acceptable bandwidth. The SVMTD design is pictured in Figure 5.16. The major changes to the antenna structure are the shortening of the back edge from 18 mm to 10 mm, and the lowering of the sector height from 8 mm to 5 mm. This design was then simulated to determine the SVMTD antenna tuning performance. Figures 5.17 and 5.18 present the simulated results pertaining to impedance match. With the new design, the antenna can now tune the full frequency range from 900 MHz to 3.5 GHz while maintaining a good impedance match and acceptable bandwidth.

Comparison of the SVMTD with the antenna element described in Chapter 3 indicates that the SVMTD is electrically smaller. For the original design presented in Figure 3.1, page 12, the *ka* of the antenna was 0.986 at 3.5 GHz and 0.254 at 900 MHz. For the SVMTD, however, the *ka* of the antenna decreased to 0.680 at 3.5 GHz and 0.175 at 900 MHz.

This decrease in *ka* is due to the shortening of both the sector's height and back edge length, which was necessary to enable the antenna to tune across the full frequency range. However, since there is no change in the antenna's operating frequencies, this reduction in size decreases the antenna's *ka* value.

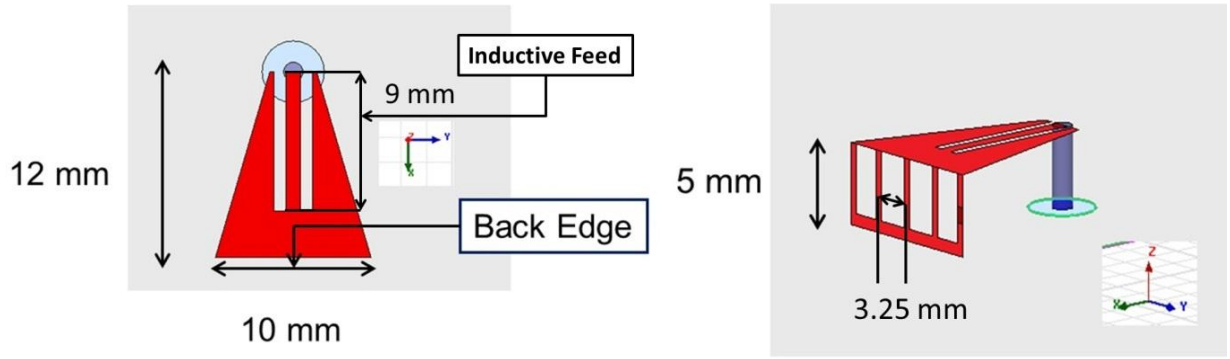

Figure 5.16: Single varactor maximum tuning design (SVMTD) geometry (Graphics from HFSS).

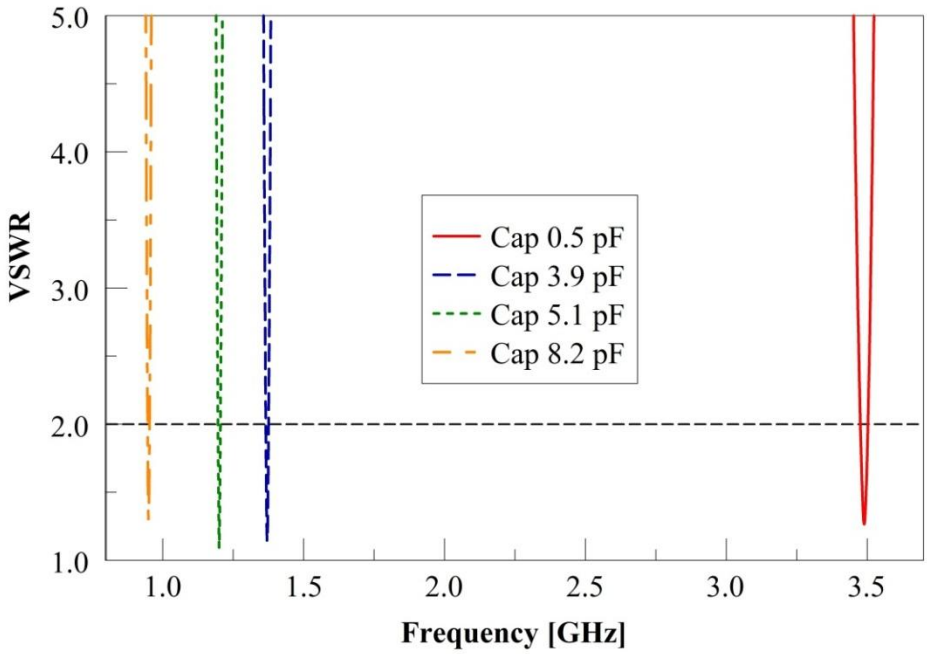

Figure 5.17: Simulated plot of VSWR versus frequency of SVMTD with varying capacitance showing good impedance match across tuning range.

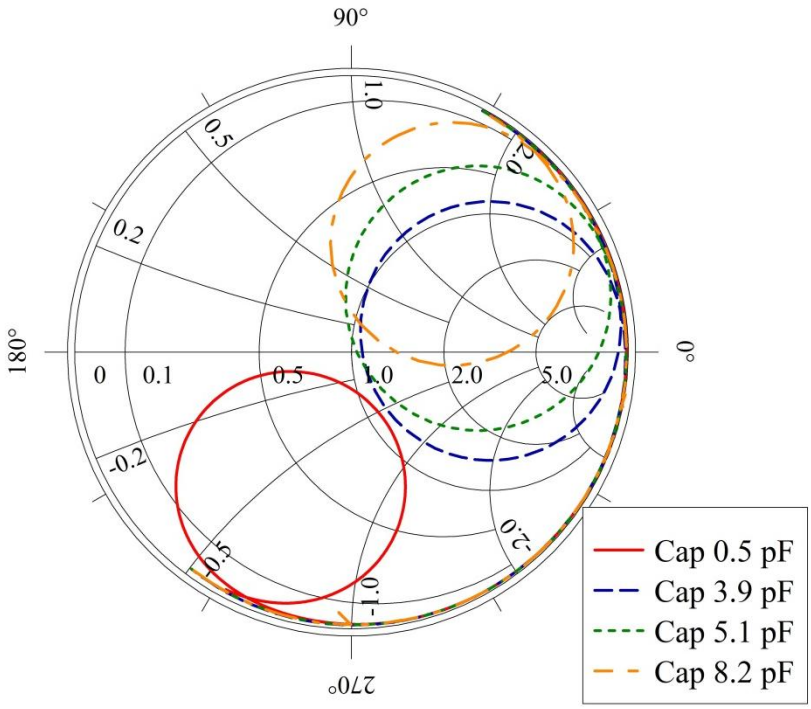

Figure 5.18: Simulated Smith chart plot of SVMTD from 0.9 to 3.5 GHz with varying capacitance.

The capacitor values for Figures 5.17 and 5.18 represent physical chip-capacitors soldered to the antenna to simulate the capacitance of the tuning varactor. In order to tune the SVMTD to a frequency of 900 MHz, a capacitor with the value of 8.2 pF was needed. Previously, the antenna only needed a capacitance of 3.3 pF to tune to 900 MHz, but this design was unable to achieve an impedance match at 3.5 GHz. Taking the knowledge gained from the three tuning studies, the SVMTD was created. This composite design is capable of maintaining a VSWR match over the entire desired frequency range, while using varactor capacitances ranging from 0.5 pF to 8.2 pF.

5.2.1 Radiation efficiency and gain of the SVMTD

Tables 5.4 and 5.5 present the simulated efficiencies and gain for the original antenna design (Chapter 3) and the SVMTD respectively. Compared with the gain of the original antenna, a few differences are notable. The overall radiation efficiency of the SVMTD decreased as a whole when compared to the original antenna's radiation efficiency. This is due to the miniaturization of the antenna footprint, decreasing the radiation resistance of the antenna, resulting in smaller radiation efficiency.

Also, antenna gain decreases with reductions in radiation efficiency and the electrical size of the structure. Since both the electrical size of the antenna and the radiation resistance are reduced in the SVMTD, a noticeable drop in gain is observed. Also, the original antenna was simulated on an infinite ground plane versus a finite ground plane for the SVMTD. With an infinite ground plane the antenna looks larger due to image theory, resulting in more radiation in the upper half plane. When a finite ground plane is used, however, radiation in the direction of the backplane reduces the overall radiation propagating in the upper half space. This backplane radiation can contribute to the reduction of antenna gain observed in the SVMTD.

Table 5.4: Original antenna efficiencies and Gain for select capacitor values.

Capacitance [pF]	Match frequency [GHz]	Radiation efficiency [%]	Gain [dBi]
0.16	3.416	90	5.109
0.4	2.552	66	3.16
0.6	1.978	47	0.657
0.8	1.746	37.5	-0.968
1	1.602	30	-2.45
3.3	0.89	16	-10

Table 5.5: SVMTD efficiencies and gain for select capacitor values.

Capacitance [pF]	Match Frequency [GHz]	Radiation Efficiency [%]	Gain [dBi]
0.4	3.5	56	2.253
1.8	2.5	19	-1.935
2.5	1.5	3.2	-8.85
6	1.0	1	-14.27
7.3	.900	0.8	-15.56

5.3 Measured Results for the SVMTD

To validate the simulated results, the SVMTD was fabricated in the lab and measured. CF series chip capacitors from Dielectric Laboratories [26] were soldered in place of the varactor diode for proof-of-concept measurements. Figure 5.19 presents a picture of the fabricated structure, and Figures 5.20 and 5.21 plot the antenna's measured VSWR and impedance, respectively.

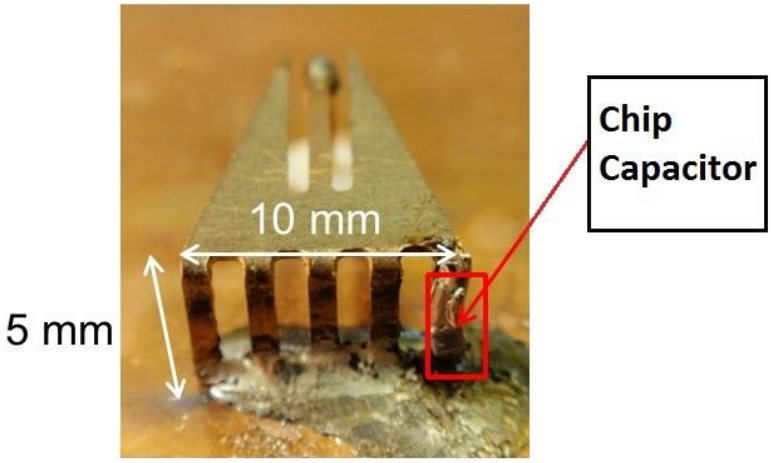

Figure 5.19: Picture of fabricated SVMTD.

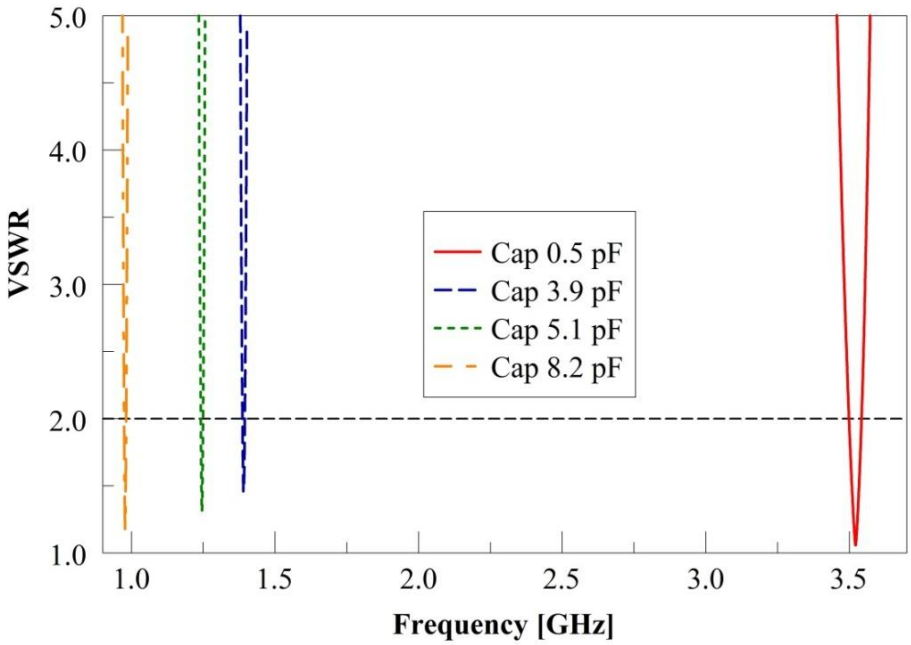

Figure 5.20: Plot of measured VSWR versus frequency of SVMTD with varying capacitance.

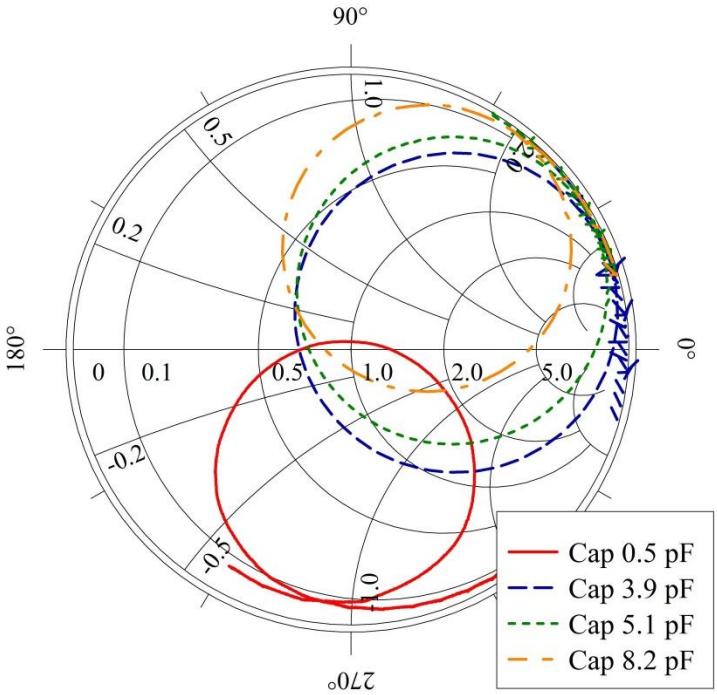

Figure 5.21: Smith chart plot of measured impedance of SVMTD from 0.9 to 3.6 GHz with varying capacitance.

Figures 5.20 and 5.21 indicate that the antenna tunes across the entire desired frequency range with capacitances varying from 0.5 pF to 8.2 pF. In addition, comparison of Figures 5.17, 5.18, 5.20 and 5.21 illustrates that data from both simulation and measurement are in good agreement. Finally, the capacitance values in Figure 5.20 depict that a capacitance ratio of 16.4 is necessary to achieve the full tuning range. While this is an improvement over the original capacitance ratio of > 20, the tuning ratio still exceeds that of commercially available varactors for these values. Therefore, alternate means must be utilized to allow for the incorporation of practical components.

5.4 Double Varactor Design

From the results in Section 5.3, it became apparent that the capacitance ratio required in order to achieve the full tuning range was not practically achievable using only a single varactor. In order to obtain full frequency range tuning, further modifications to the tuning mechanisms of the antenna needed to be performed.

However, results from the DC blocking capacitor study in Chapter 6 indicate that capacitors placed in the other inductive loads may produce a secondary frequency match when the corresponding capacitance was selected appropriately. This secondary frequency match along with careful design and selection of two separate varactors could lead to a practical full frequency range design. Additionally, at this stage in the development process it was stated that the antenna need only tune continuously from 1.8 GHz to 3.5 GHz as long as the frequency band surrounding the 900 MHz region still existed. In light of these new specifications a double varactor design was analyzed to realize this new design goal.

Figure 5.22 presents the antenna geometry with two varactors placed in the inductive loads on opposite sides of the antenna. In order for this design to function correctly, one of the varactors (the primary varactor) must tune the match frequency continuously from 1.8 to 3.5 GHz while the other varactor (the secondary varactor) provides a good impedance match at 0.9 GHz. In addition, the impedance match at 0.9 GHz should be present at only one DC bias voltage to avoid dual frequency operation within the band of interest. Simulations performed in HFSS were used in order to determine the capacitance values necessary for successful antenna operation.

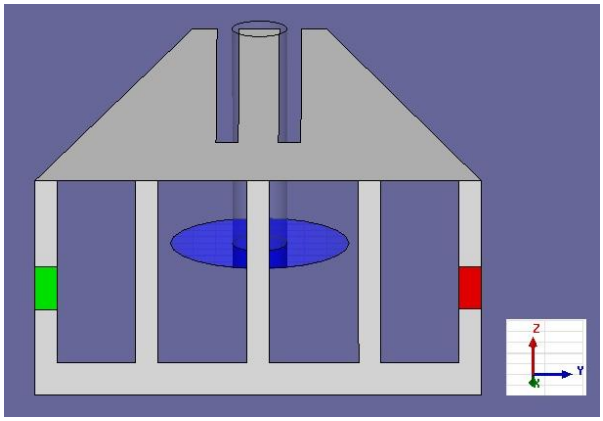

Figure 5.22: Double varactor antenna geometry. The varactor on the left (green, secondary varactor) was held constant at 7 pF and the varactor on the right (red, primary varactor) was varied from 0.4 to 3.3 pF (Graphics from HFSS).

Figures 5.23 and 5.24 depict the impedance characteristics when the secondary varactor was held constant at 7 pF and the primary varactor was varied from 0.4 to 3.3 pF. Figure 5.23 plots the VSWR versus frequency, indicating two operating frequencies when the primary varactor is tuned from 0.4 to 3.3 pF while the secondary varactor is held at 7 pF capacitance, and the presence of dual frequency operation. The first of these frequencies occurs at approximately 0.9 GHz and remains unchanged with varying capacitance, whereas the second match frequency tunes from 1.2 to 3.5 GHz.

Similarly, Figure 5.24 presents two impedance circles for each capacitance on the Smith chart, with the circle associated with the changing primary varactor capacitance traversing around the Smith chart illustrating that the two frequencies can be operated independently. However, since only one match frequency must exist within the frequencies of interest at any given time, the capacitance of the secondary varactor must be tuned to ensure that dual frequency operation does not occur within the desired frequency range. The requirement for single frequency operation is as follows.

When operated in both receive and transmit modes, the antenna may be viewed as a bandpass filter that rejects spurious signals at frequencies outside the impedance bandwidth. In receive mode, dual frequency operation within the desired tuning range fails to attenuate incident signals at undesired frequencies (one of the two dual frequencies), and additional processing might be necessary in the device back-end to remove these interfering signals, especially if their signal

strength is strong. These undesirable signals place additional constraints on the electronics of the device itself, and may severely degrade the overall system performance. Since antennas are reciprocal devices, similar issues exist when operating the antenna in transmit mode. By designing the two varactors to operate independently and only produce one impedance match in the frequency band of interest, the effect of undesired signals can be eliminated.

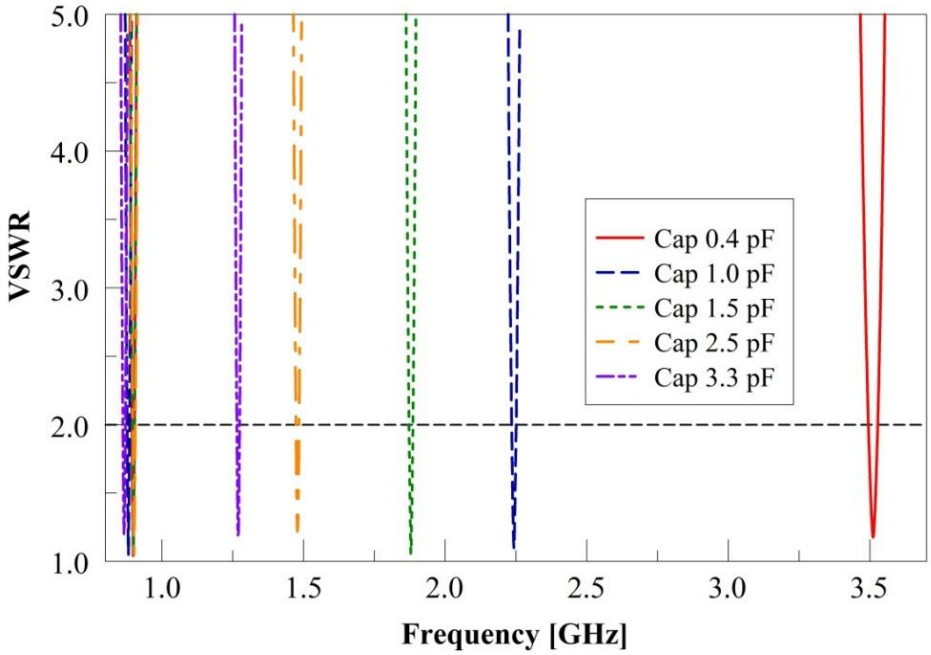

Figure 5.23: Simulated plot of VSWR versus frequency with the secondary varactor held constant at 7 pF and the primary varactor varied from 0.4 to 3.3 pF.

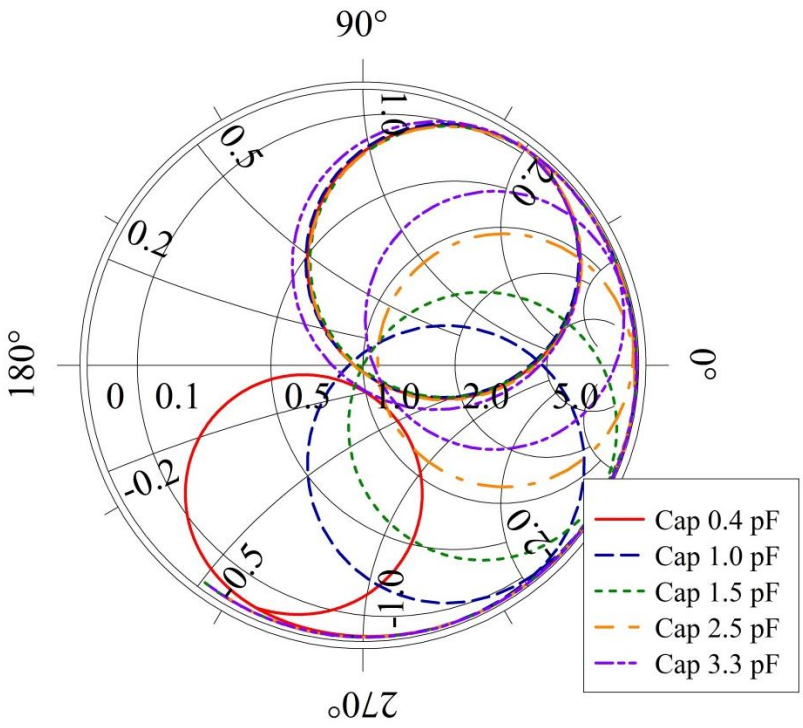

Figure 5.24: Simulated Smith chart plot from 0.9 to 3.5 GHz with secondary varactor held constant at 7 pF and primary varactor varied from 0.4 to 3.3 pF.

Figure 5.25 shows the effect of tuning the secondary varactor from 5 pF and 10 pF. When the capacitance value is increased to a value higher than 7 pF, simulations indicate that the impedance match occurs below the frequency band of interest. In addition, the results from Figures 5.23 and 5.25 indicate that with careful selection of capacitor values, it is possible to design an antenna that tunes the entire frequency band, while simultaneously avoiding dual frequency operation. Sections 5.4.1 through 5.4.3 present the finding that simultaneously tuning both the primary and secondary varactors alleviates the issue of dual frequency operation, yielding only single frequency operation within the tuning range.

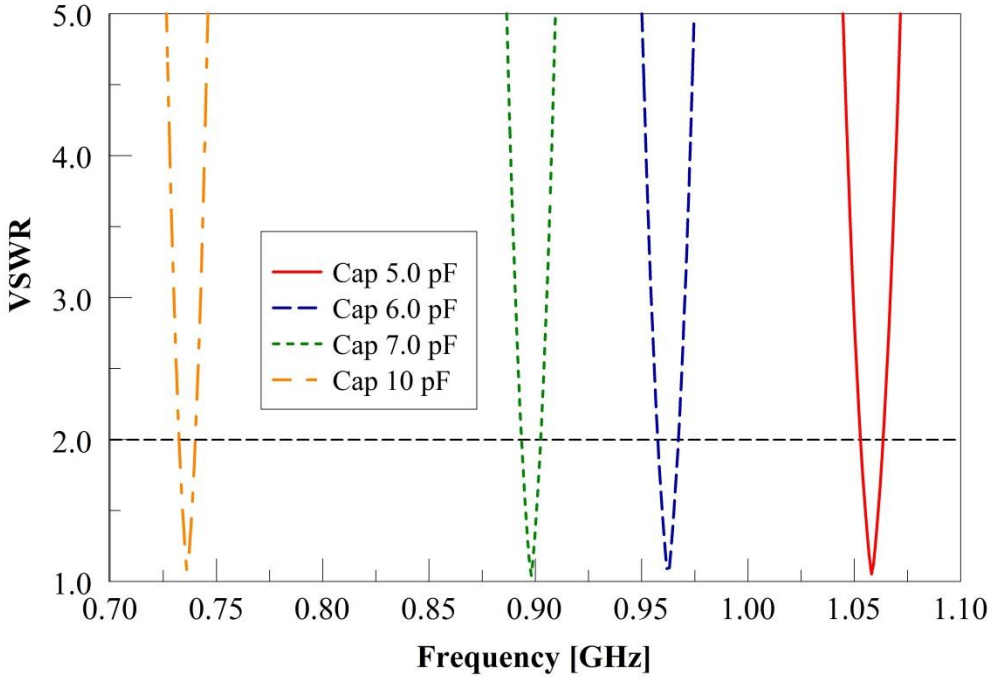

Figure 5.25: Simulated plot of VSWR versus frequency when the secondary varactor was varied from 5 to 10 pF.

5.4.1 Operating physics of the dual varactor antenna

With inclusion of the secondary varactor, it was necessary to ascertain that its addition does not change the original tuning mechanism of the antenna structure. The basis for frequency reconfiguration of this antenna is the varactor's ability to pull different amounts of current to the corner of the structure at various capacitance values, thus altering the effective length of the current path. Theoretically, the incorporation of a second varactor with larger capacitances results in strong current flow in its associated vertical inductive load at lower frequencies, while leaving the current flow at higher frequencies undisturbed.

Figures 5.26, 5.27 and 5.28 plot the surface currents when the primary varactor (varactor on right) was 0.4 pF (3.5 GHz), 1pF (2.25 GHz), and 1.5 pF (1.85 GHz), respectively. In all three plots, the secondary varactor was held constant at 7 pF. These frequencies match the operating frequency of the antenna at the corresponding capacitances.

Examination of all three plots indicates that the secondary varactor pulls significantly less current than the primary varactor at these frequencies. Furthermore, as the capacitance of the

primary varactor increases, the amount of current present on the corresponding edge of the structure increases, while the current flowing through the secondary varactor remains relatively constant. As a result, the antenna can still be continuously tuned from 1.85 to 3.5 GHz by changing only the capacitance of the primary varactor.

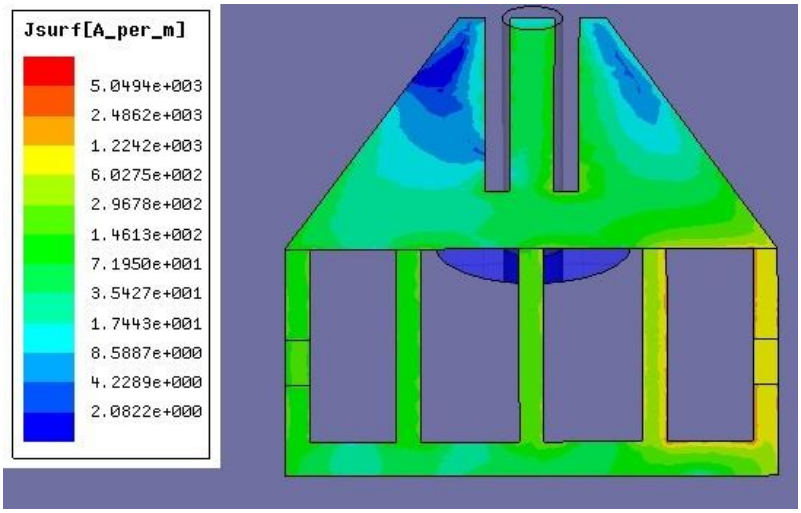

Figure 5.26: Surface current plot of antenna at 3.5 GHz. The primary varactor had a capacitance of 0.4 pF whereas the secondary varactor was kept constant at 7 pF (Graphics from HFSS).

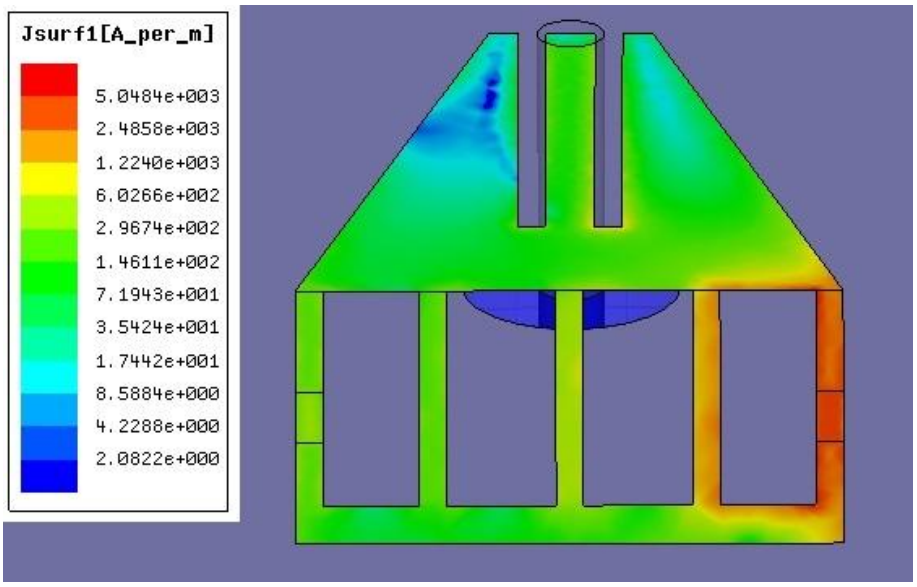

Figure 5.27: Surface current plot of antenna at 2.25 GHz. The primary varactor had a capacitance of 1.0 pF whereas the secondary varactor was kept constant at 7 pF (Graphics from HFSS).

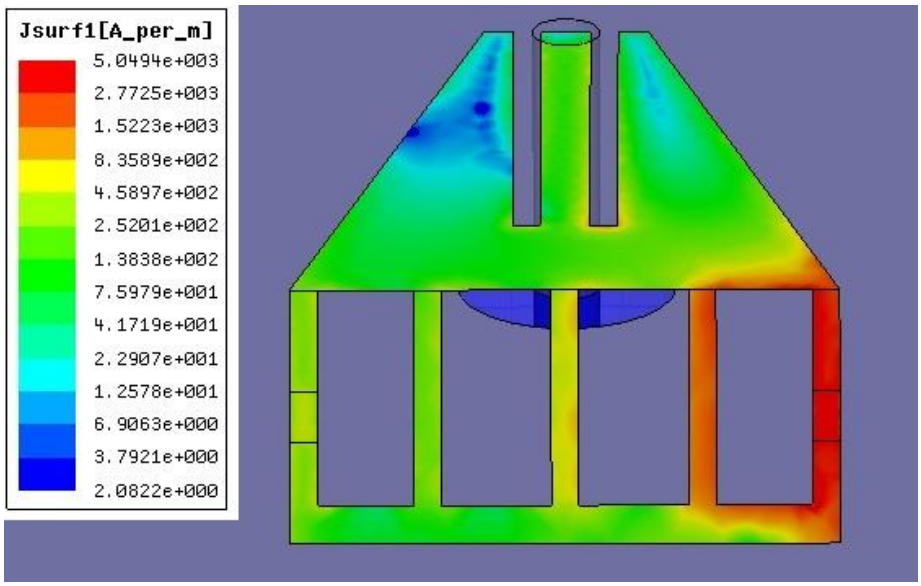

Figure 5.28: Surface current plot of antenna at 1.85 GHz. The primary varactor had a capacitance of 1.5 pF whereas the secondary varactor was kept constant at 7 pF (Graphics from HFSS).

Similarly, Figures 5.29, 5.30 and 5.31 plot the surface currents at 0.9 GHz when the capacitance on the secondary varactor was kept at 7 pF, and the primary varactor had a capacitance of 0.4 pF, 1 pF, and 1.5 pF, respectively. Examination of all three plots indicates that the current distributions across the antennas do not vary appreciably with changing primary varactor capacitances, and most of the current flows through the secondary varactor. As a result, the operating frequency of the antenna stays at 0.9 GHz, irrespective of the primary varactor capacitance.

Results from Figures 5.26 to 5.31 demonstrate that with the chosen capacitance values, the current flows on both varactors are unaffected by each other at their associated match frequencies. Because of this independence, the addition of a secondary varactor enables antenna tuning to 0.9 GHz without affecting the impedance match at higher frequencies. Candidate varactors that enable frequency reconfiguration across the whole tuning range are determined in the following section.

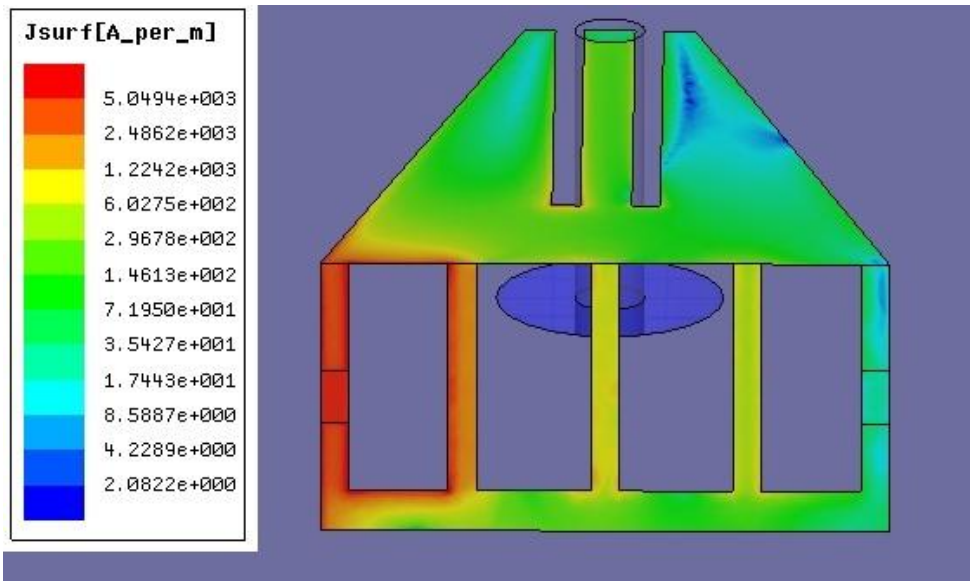

Figure 5.29: Surface current plot of antenna at 0.9 GHz. The primary varactor had a capacitance of 0.4 pF whereas the secondary varactor was kept constant at 7 pF (Graphics from HFSS).

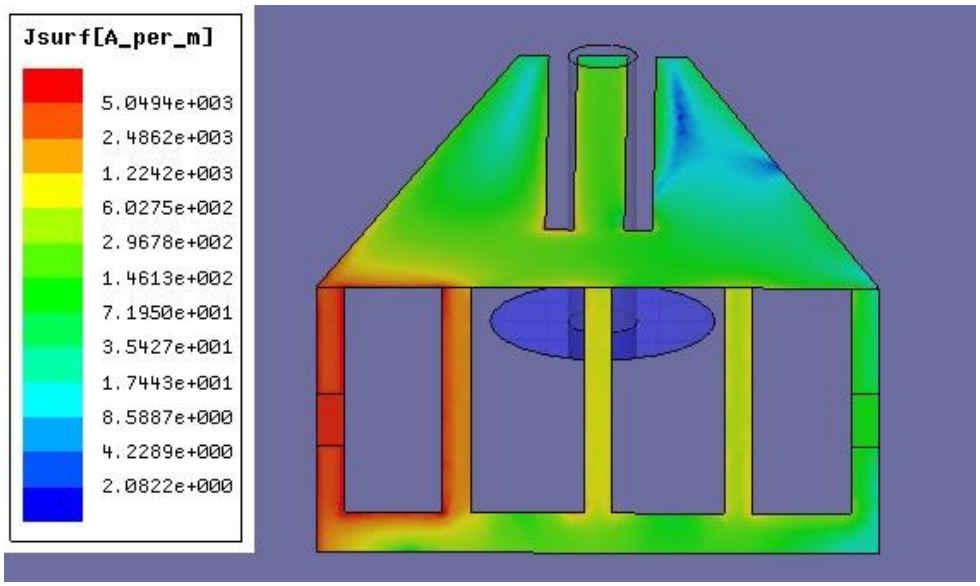

Figure 5.30: Surface current plot of antenna at 0.9 GHz. The primary varactor had a capacitance of 1 pF whereas the secondary varactor was kept constant at 7 pF (Graphics from HFSS).

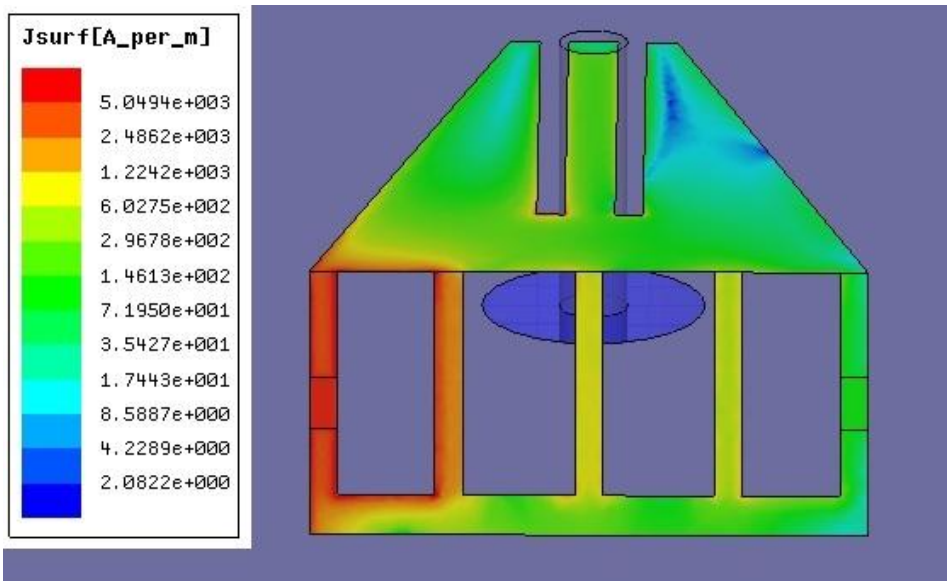

Figure 5.31: Surface current plot of antenna at 0.9 GHz. The primary varactor had a capacitance of 1.5 pF whereas the secondary varactor was kept constant at 7 pF (Graphics from HFSS).

5.4.2 Candidate varactors for frequency tuning

Since the double varactor design allows for full frequency tuning, a search was performed to find commercially available varactors that would fit the design parameters for the antenna system. One such candidate for the primary varactor is the Microsemi GC15002 [24] varactor that can tune from 2.4 pF (C_{high}) to 0.3 pF (C_{low}) with bias voltages ranging from 2 V to 20 V. This enables the antenna to tune continuously from 1.4 GHz to past 3.5 GHz.

For the secondary varactor, multiple options exist that enable tuning in only the 0.9 GHz band. Two such candidates are Microsemi's GC15012 and GC15014 [24] varactors. Both these varactors are able to produce a 7 pF capacitance at 20 V, and increase to capacitance values of 30 pF and 50 pF, respectively, at 2 V DC bias. Therefore, at bias voltages below 20 V (and capacitance values of above 7 pF), the match frequency associated with the secondary varactor will be below 0.9 GHz, and the changing capacitance on the primary varactor results in only one operating frequency between 1.4 to 3.5 GHz. However, at 20 V DC, the 7 pF capacitance on the secondary varactor yields a match frequency at 0.9 GHz, whereas the 0.3 pF on the primary varactor produces an impedance match at a frequency above 3.5 GHz. Again, only one operating frequency is present between 0.9 and 3.5 GHz. While both the GC15012 and 15014 are suitable

candidates for the secondary varactor, the design favors the GC15012 diode due to its ability to achieve a higher capacitance similar to the DC blocking capacitors used in the bias network. Even though this biasing scheme does not enable continuous tuning from 0.9 to 1.5 GHz, the project goals were amended to not require impedance match frequencies between 0.9 and 1.8 GHz. Therefore, a combination of the GC15002 with either the GC15012 or the GC15014 varactors is suitable to achieve the full required tuning range. Finally, Figure 5.32 presents a plot of VSWR versus frequency, indicating the frequency range covered by both the primary and secondary varactors.

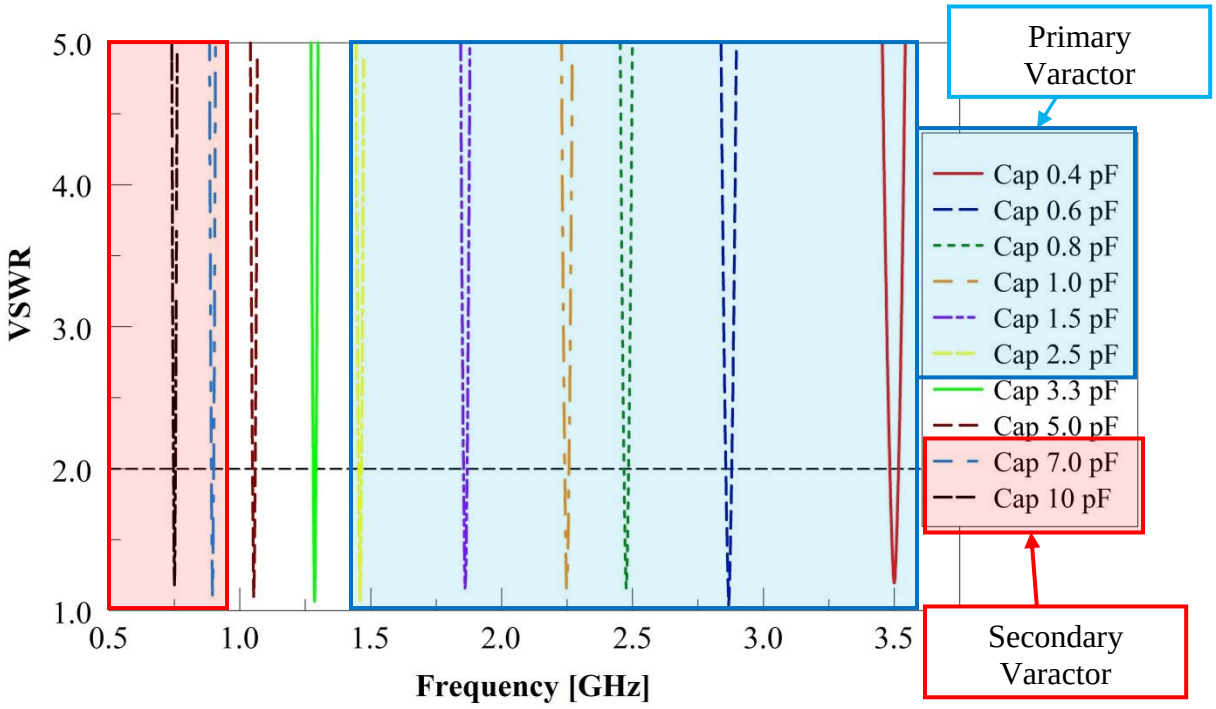

Figure 5.32: Simulated plot of VSWR versus frequency of dual varactor antenna indicating achievement of full tuning range.

5.4.3 Results

To improve the maximum tuning ability of the antenna, multiple changes in the geometry of the structure were made and analyzed. It was found that the previously removed sector cant angle allowed for full frequency tuning but with unacceptable bandwidth and unrealistic varactor tuning ratios. Likewise, the combination of the sector back edge length and the sector height allowed for full frequency tuning utilizing a single varactor, but not with commercially available varactors.

Finally, the double varactor design demonstrated that the addition of a carefully chosen second varactor did not interfere with the performance of the original varactor. Using superposition, combination of the two varactors enables realization of the full, required tuning range using commercial varactor values and a DC bias of 2 V to 20 V.

Chapter 6

DC BIAS NETWORK

6.1 Preliminary Bias Network

Unlike for conventional antennas, the design of a bias network and the placement of tuning elements must be very carefully considered for electrically small antennas. Because the antenna is electrically small in comparison to a wavelength, any bias lines or tuning elements that are not designed or chosen correctly will become a part of the antenna and begin to radiate, reducing efficiency and causing shifts in the radiation patterns.

The original proposed bias network for the sector antenna is depicted in Figure 6.1. It consisted of a bias "tee" where the DC bias voltage and the RF power was to be fed to the antenna through the probe feed. This allowed for a DC bias voltage to be present on the structure of the antenna without the need to carefully design bias lines so that they do not radiate. With this configuration a varactor could then be DC biased when placed in the inductive load of the antenna utilizing the ground plane of the antenna as the DC and RF ground.

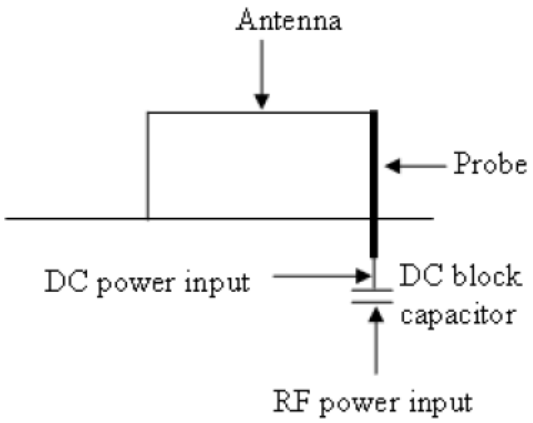

Figure 6.1 Original proposed bias network.

However, during the modification of the structure to allow for frequency reconfiguration, multiple inductive loads were added to the back edge of the antenna structure for impedance matching purposes. These extra vertical loads helped achieve a realizable design for frequency reconfiguration, but in the process introduced multiple DC shorting paths to ground which, if the

original bias network was kept, would not allow for a DC bias to be maintained on the structure. In order to properly bias the varactor(s), a new DC bias system was required.

In order to achieve a bias voltage on the antenna, the addition of DC blocking capacitors into the additional inductive loads was proposed. A DC blocking capacitor takes advantage of how a capacitor's impedance changes with frequency. An ideal capacitor's impedance changes according $Z = 1/\omega C$. At zero frequency (DC), the impedance of an ideal capacitor goes to infinity, effectively creating an open circuit. As the signal frequency increases from DC, the impedance of the capacitor drops as a function of frequency. At high frequencies the impedance of the ideal capacitor approaches zero or a short circuit, illustrating how a capacitor can be utilized to block DC voltages, but allow RF signals to pass unaffected.

6.2 Revised Bias Network

The original intention of the DC bias network was for it to be "invisible" to the antenna to allow for simple element design and biasing. Using ideal components, designing such an "invisible" bias network only involves choosing a capacitance value large enough to maintain reliable short at RF ($Z \leq 2\ \Omega$) [27] and an open at DC. Unfortunately, the chip capacitors intended for use as blocking capacitors are not ideal and contain package parasitic components that drastically affect how the device behaves over frequency.

A typical realistic chip-capacitor can be modeled as the series/parallel resonant circuit shown in Figure 6.2 [27]. This model includes the packaging inductance L_S, equivalent series resistance (ESR) R_S, package capacitance C_P, equivalent parallel resistance R_P, and the diode junction capacitance (tuning capacitance) C_S.

Ignoring the resistance parallel to the capacitance (for most blocking capacitors this value is extremely large and therefore can be considered an open), the model forms a combination series/parallel RLC resonant circuit. The effective behavior of the chip capacitor depends on where the resonances of this series/parallel RLC circuit occur.

When the series RLC circuit resonates this is referred to as the series self-resonance frequency (SSRF) of the capacitor. The SSRF for the blocking capacitor corresponds to the frequency

where the effective reactance transitions from negative (capacitive) to positive (inductive). After the SSRF, the chip capacitor behaves like an inductor instead of a capacitor. This inductive behavior continues until the parallel portion of the circuit resonates at the parallel self-resonant frequency (PSRF) and the effective reactance becomes capacitive again. After the chip capacitor's first set of resonances, the device continues to cycle between series and parallel resonances as frequency increases. The behavior of these series and parallel resonance frequencies can be observed in Figure 6.3.

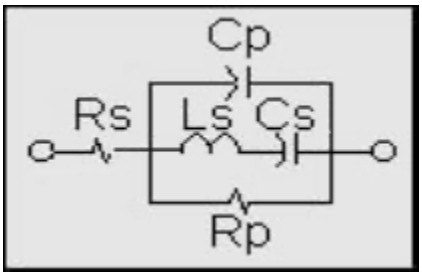

Figure 6.2: Circuit model for DC blocking capacitor.

Even taking the non-ideal behaviors of the chip capacitors into consideration, designing an "invisible" bias network can be accomplished relatively easily for small frequency ranges where the blocking impedance is fairly constant. However, when dealing with large frequency ranges (such as with this thesis), it is often found that the series resonant frequency or a parallel resonant frequency interferes with a desired band of interest.

Because of the frequency dependence inherent with realistic blocking capacitors, careful consideration must be made for their implementation into any sensitive design. With the understanding that the capacitors used in the bias network are not ideal capacitors and contain parasitic effects, a search for possible candidate blocking capacitors was performed.

6.2.1 Candidate blocking capacitors

The inductively loaded sector design is very sensitive to changes in relative impedances (in accordance to its design in Chapter 5), especially when they occur in the inductive loads. Therefore, in order to implement a working DC bias network, candidate blocking capacitors must be chosen so that they do not adversely affect the impedance match of the antenna.

The original option considered for achieving a DC block was the Dielectric Laboratories C11CF510J6TXL 51 pF chip capacitor [27]. This capacitor was originally chosen because it exhibited a low reactance throughout the entire frequency range and would not interfere with the capacitances of the tuning varactors when considering it as an ideal component. In order to characterize the realistic performance of the chip capacitor over the frequency range of 0.9 to 3.5 GHz, Dielectric Laboratories CapCAD modeling software was utilized. As Figure 6.3 shows, when modeled with parasitics included, the 51 pF capacitor undergoes its first series resonance at approximately 1.3 GHz and its first parallel resonance near 2.2 GHz.

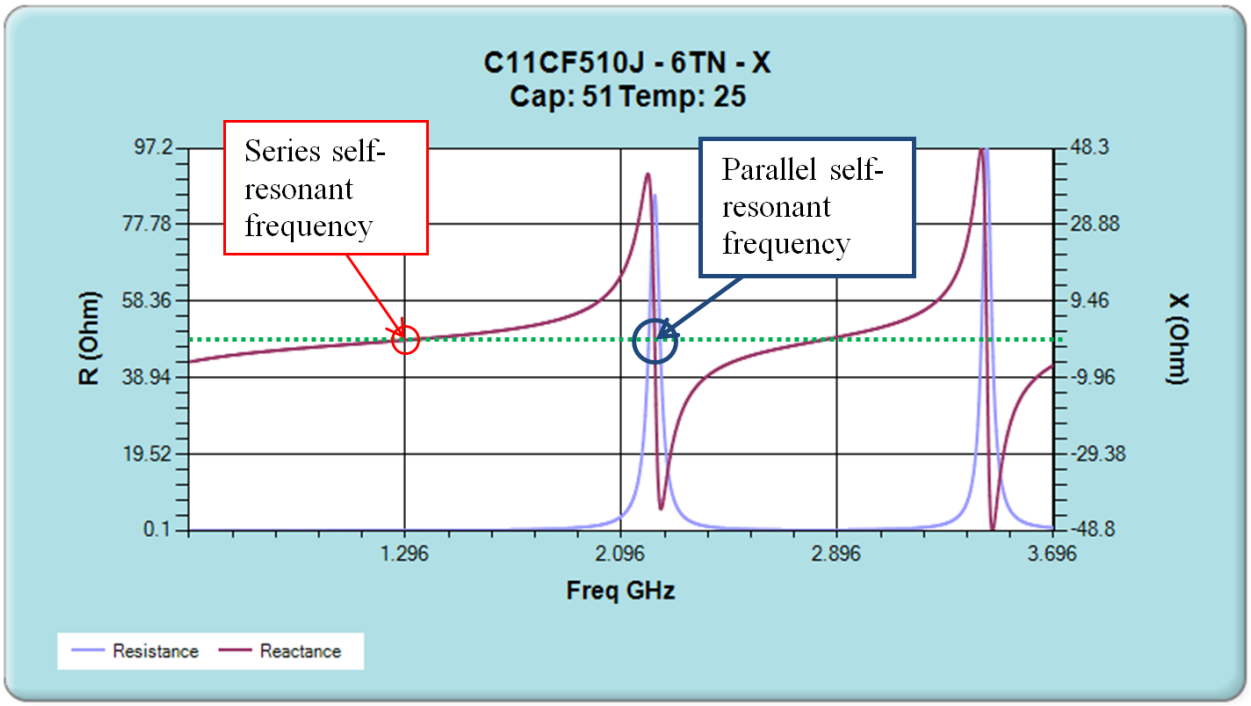

Figure 6.3: Impedance over frequency for the C11CF510J6XTL (From [27]).

Table 6.1 shows the effective component values and effective series resistance of the C11CF510J6TXL at the bands of interest. It is noted that for both the 1.8 GHz and 2.0 GHz bands, the blocking capacitor is inductive. Also, at 3.5 GHz, the effective series resistance is almost 13 Ω. Taking Figure 6.3 and Table 6.1 into consideration, it is apparent that the C11CF510J6TXL will seriously impact the performance of the antenna in several different frequency bands (1.8 GHz, 2.0 GHz, 3.5 GHz), making the implementation of the DC bias network with only this chip capacitor impossible. Considering the troublesome behavior of the C11CF510J6TXL, a search was performed to find a more suitable blocking capacitor.

Table 6.1: Effective values of the C11CF510J6TXL (51 pF) blocking capacitor.

Frequency [GHz]	Effective Component Value	Effective Series Resistance [Ω]
0.9	83.57 pF	0.111
1.8	0.327 nH	0.444
2.0	0.698 nH	1.280
2.4	6.41 pF	1.34
3.5	1.32 pF	12.95

Dielectric Labs manufactures broadband blocking capacitors specifically for applications that require DC blocks while maintaining consistent performance over large frequency ranges. One such capacitor present in the lab was the C06BL851X-1UN-X0T 850 pF broadband blocking capacitor. The broadband blocking capacitors are specifically designed so that their first SSRF occurs at a very high frequency (20 GHz in this case) [27]. Observing the CapCAD model of this capacitor (Figure 6.4), it was noted that over the frequency range of interest both the effective series resistance (ESR) and the effective reactance of the capacitor performed much more consistently than the 51 pF capacitor described previously.

Due to their special design for broadband blocking applications the C06BL851X-1UN-X0T exhibits no series or parallel resonance in any of the bands of interest. Throughout the frequency range the reactance is capacitive, ranging from -0.5 to -1.42 Ω, and the ESR ranges from 1.65 to 1.82 Ω. Table 6.2 shows the effective component values of the C06BL851X-1UN-X0T at the five bands of interest.

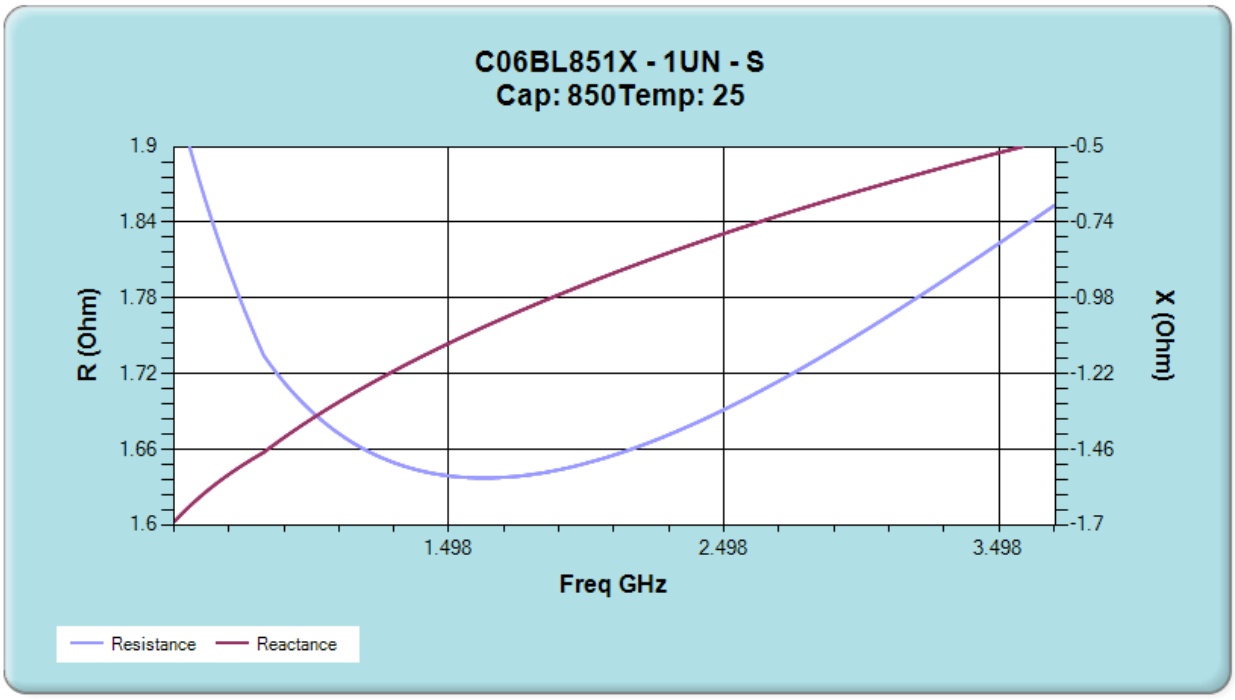

Figure 6.4: Impedance over frequency for the C06BL851X-1UN-X0T (from [27]).

Table 6.2: Effective values of the C06BL851X-1UN-X0T (850 pF) blocking capacitor.

Frequency [GHz]	Effective Component Value	Effective Series Resistance [Ω]
0.9	124.5 pF	1.71
1.8	88.42 pF	1.64
2.0	85.2 pF	1.65
2.4	82.28 pF	1.66
3.5	87.45 pF	1.82

6.2.2 Addition of blocking capacitors

The DC blocking capacitors were inserted into the HFSS design by placing them in the three inductive loads that did not contain varactors. They were modeled by two lump RLC boundaries placed in series, one for the effective reactance and the other for the ESR. The configuration of the antenna with the blocking capacitors can be observed in Figure 6.5. For the pictured configuration, the blue boxes correspond to the varactors, the green boxes correspond to the reactive component of the blocking capacitor impedance, and the red boxes correspond to the ESR of the blocking capacitor.

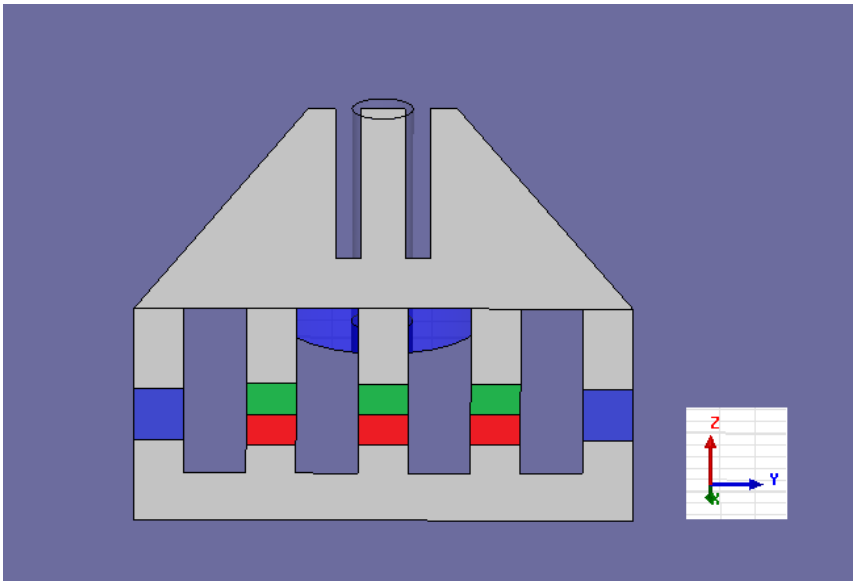

Figure 6.5: Placement of DC blocking capacitors (Graphics from HFSS).

6.3 Characterization of Antenna with Blocking Capacitors

In order to analyze the effect that the realistic blocking capacitors would have on the antenna's performance, simulations were run inserting the effective circuit parameters of the blocking capacitors at specific frequencies and observing how they affected the impedance match of the antenna. For each frequency band, the corresponding effective circuit values listed in Tables 6.1 and 6.2 were used in the simulation. Also, considering how the DC bias network could impact the performance of the entire antenna structure, the simulations were performed on antennas not only with the bias network inserted, but also realistically modeled varactors. The work regarding how the varactors were modeled and their effect on the antenna can be found in Chapter 7, Section 7.2.

The simulation setup for analyzing the bias network is pictured in Figure 6.6. The figure is color coded to indicate which lump RLC corresponds to what effect. Blue corresponds to the varactor capacitance, orange to parasitic inductance for the varactor, green to the effective component value of the blocking capacitor at a specific frequency, and red to the series resistance present in either the varactor or the blocking capacitor.

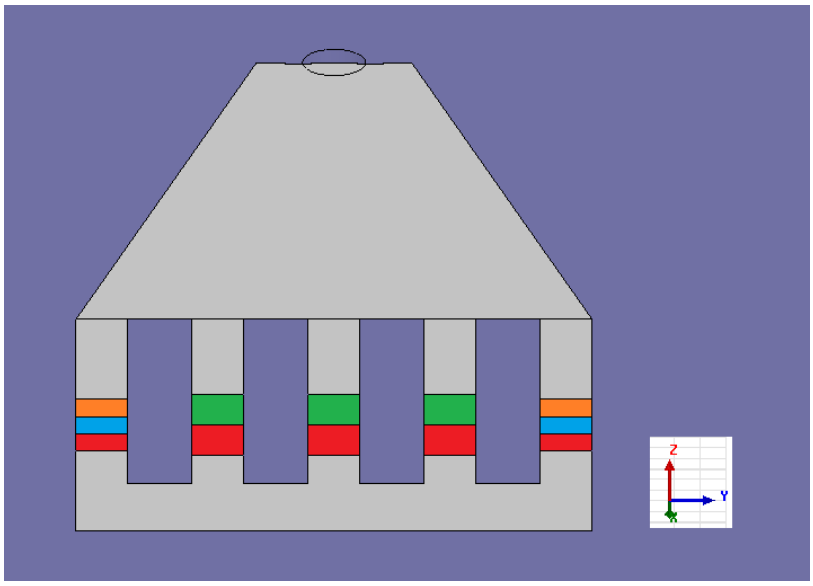

Figure 6.6: DC blocking capacitor simulation setup with realistic varactors included (Graphics from HFSS).

6.3.1 Broadband blocking capacitors

After analyzing the realistic performance of the blocking capacitors over the entire frequency range (Section 6.2.1), it was decided to implement the design with three of the C06BL851X-1UN-X0T 850 pF broadband blocking capacitors due to their consistent performance without any resonances over the bands of interest.

Figures 6.7 and 6.8 show the performance of the antenna over the entire frequency range for the 850 pF blocking capacitor DC bias network. It can be noted from looking at the VSWR match for the low frequency bands (Figure 6.7) that the additional 1.4 to 1.8 Ω of resistance has a significant effect on the antenna's performance. The Smith chart in Figure 6.8 makes clear that the antenna has become more inductive due to the presence of the ESR in the inductive loads which limit the current flowing through each load, thereby shrinking the impedance circles.

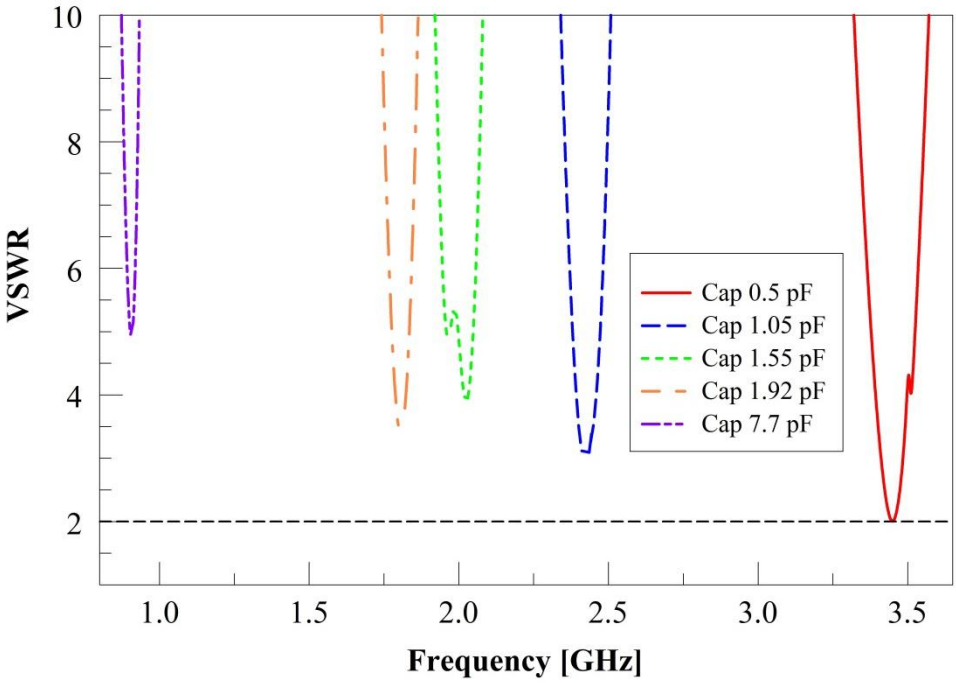

Figure 6.7: Simulated plot of VSWR versus frequency for the DC bias network with broadband capacitors.

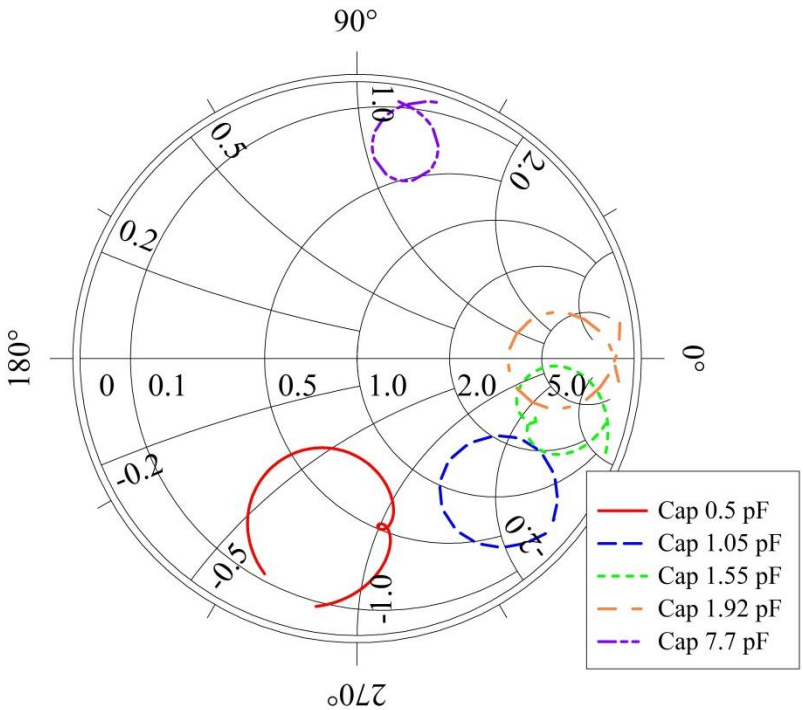

Figure 6.8: Simulated Smith chart plot from 0.9 to 3.5 GHz for the DC bias network with broadband capacitors.

From Figures 6.7 and 6.8, it is clear that the implementation of the DC bias network with the broadband capacitors has a significant effect on the impedance match of the antenna, especially at low frequencies. In order to improve the antenna's performance, changes to the antenna's structure needed to be made.

It was hypothesized that, since the vertical inductive load immediately next to the low frequency varactor has a large amount of surface current present at 0.9 GHz, the added ESR of the blocking capacitor caused the impedance match to degrade. In order to investigate this, the position of the inductive loads with respect to the varactors was varied in order to see if, by reducing the amount of current present on the inductive loads with blocking capacitors, the impedance match of the antenna could be restored.

Figures 6.9 and 6.10 show how the position of the inductive loads affects the match of the antenna as they are varied from 1.25 mm (original position) to 2.0 mm. As predicted, as the inductive load is moved farther from the active varactor, the impedance match is improved, signifying that less current is present on the load. However, it can be noted that even when the inductive load is at 2.0 mm (the farthest from the low frequency varactor) that the impedance match is still unsatisfactory. Therefore, in order to obtain a good impedance match, a different approach was necessary.

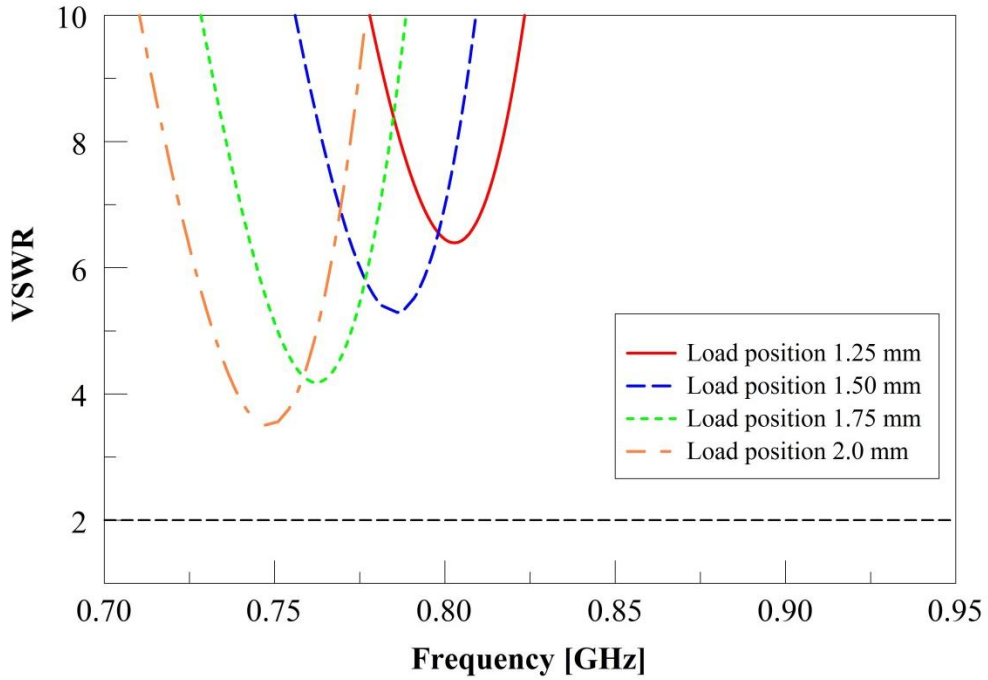

Figure 6.9: Simulated plot of VSWR versus frequency for changing the distance between inductive loads.

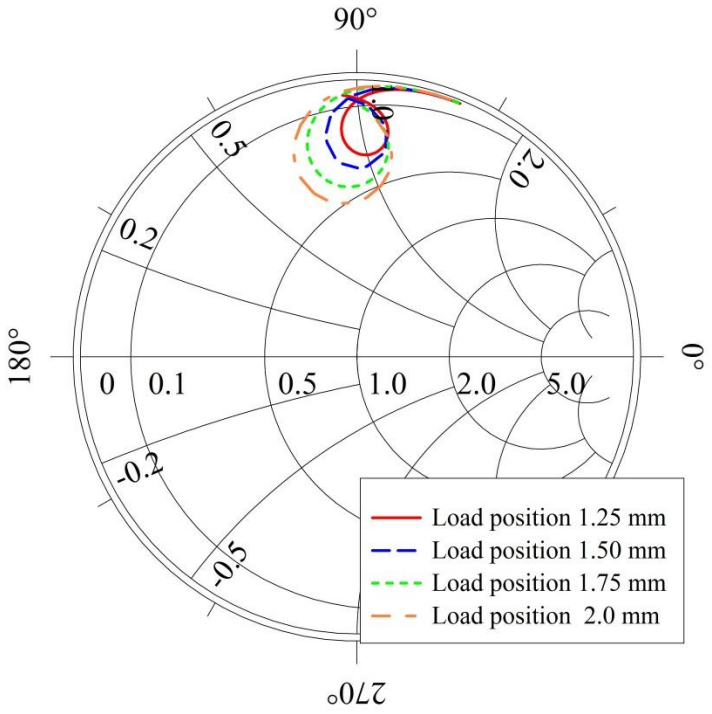

Figure 6.10: Simulated Smith chart from 0.7 to 0.95 GHz for the changing the distance between inductive loads.

6.3.2 Combination of blocking capacitors

The results of the previous section indicate that for the low frequency range, the value of the ESR is critical. Unfortunately, even though the broadband blocking capacitors had a low ESR (1.4-1.8 Ω), it was still too much resistance to maintain an impedance match at 0.9 GHz. To address this, it was hypothesized that by placing a 51 pF capacitor in the load closest to the low frequency varactor and placing 850 pF blocking capacitors in the other two inductive loads, reasonable performance could be realized. This configuration takes advantage of the combination of the behavior of the double varactor design (Chapter 5, Section 5.4.2) and the low ESR at 0.9 GHz (0.111 Ω) of the C11CF510J6TXL to obtain an impedance match at low frequencies while minimizing the impedance degradation of the higher frequency bands.

In Section 6.3.1 it was found that moving the inductive loads adjacent to the varactors toward the center load resulted in an improvement in the impedance match of the antenna. Using these results, the inductive loads were positioned 0.8 mm from the center post (2.0 mm from the varactors) in order to achieve the best possible impedance match. Another small change to the structure is the reduction in width of the inductive loads containing the blocking capacitors. To decrease the inductance of the structure as much as possible, the widths of the parallel inductive loads were decreased to 0.8 mm, the feature size limit of the fabrication method used.

The simulation test utilizing both blocking capacitors is pictured in Figure 6.11. The notable change to the structure is that the leftmost blocking capacitor is now the C11CF510J6XTL 51 pF capacitor (yellow and pink), while the other two blocking capacitors remain the C06BL851X-1UN-X0T 850 pF (green and red).

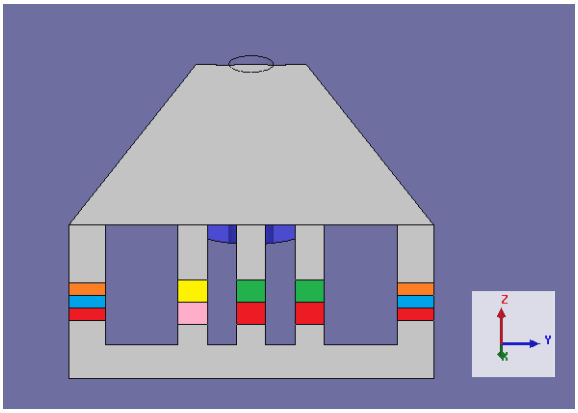

Figure 6.11: DC bias network simulation setup with two types of blocking capacitors (Graphics from HFSS).

Figures 6.12 and 6.13 show the results of the combinational bias network simulation. It can be noted that an impedance match is now able to be obtained at 0.9 GHz; also this match is maintained over the entire frequency range.

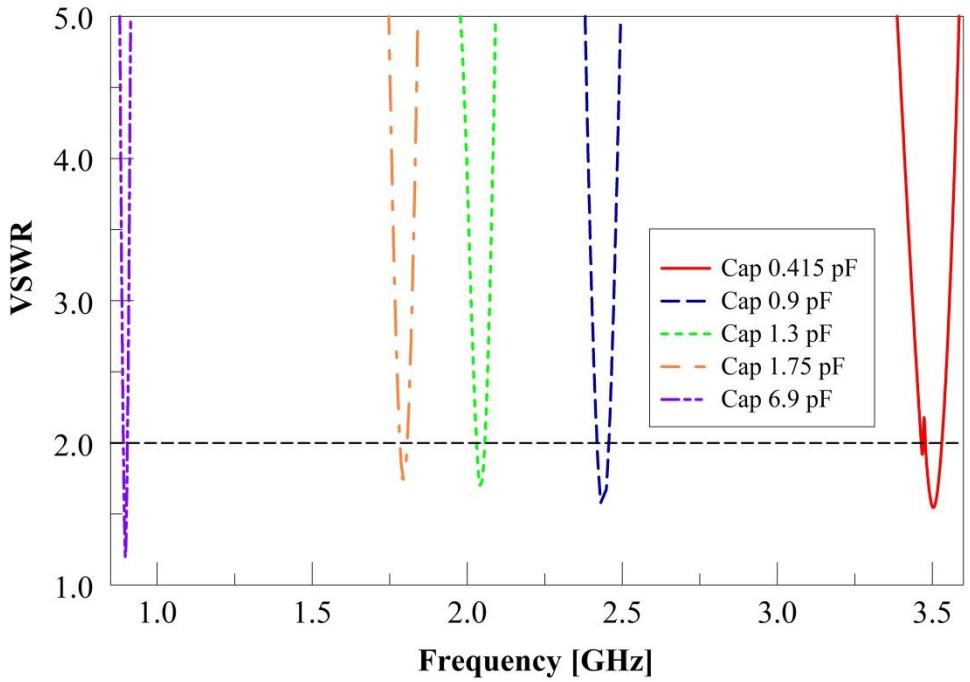

Figure 6.12: Simulated plot of VSWR versus frequency for combinational bias network.

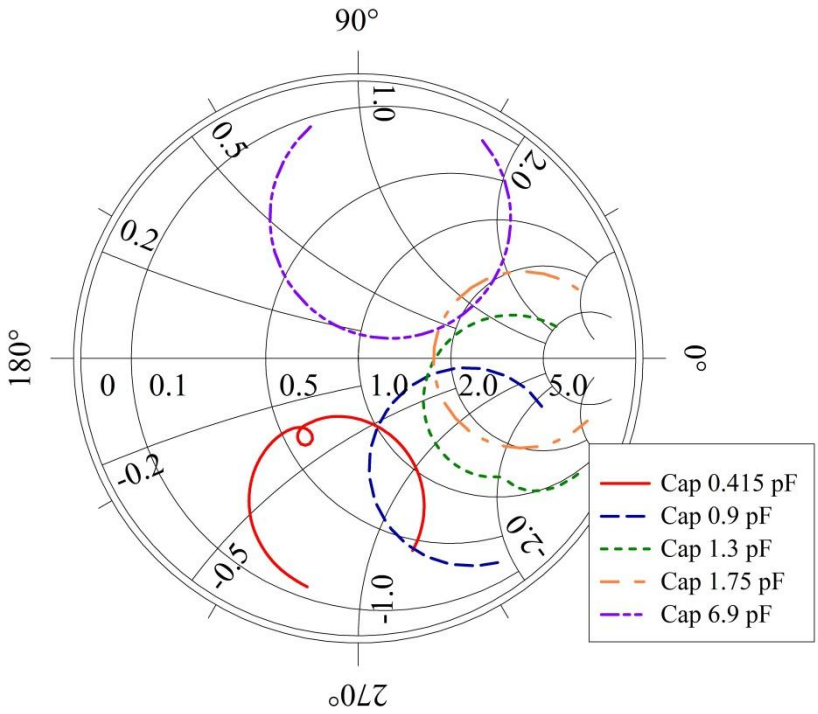

Figure 6.13: Simulated Smith chart plot from 0.9 to 3.5 GHz for the combinational DC bias network.

In order to visualize the effect on antenna performance of surface currents present on the different inductive loads, Figures 6.14 and 6.15 show the surface currents on the structure for 0.9 GHz and 3.5 GHz, respectively. First, as predicted, moving the leftmost inductive load away from the low frequency varactor reduces the amount of current present, thereby reducing the impact of the blocking capacitor contained in that load. Similarly, Figure 6.15 demonstrates that at 3.5 GHz little current is present on the load with the 51 pF capacitor, allowing for undisturbed performance at this frequency.

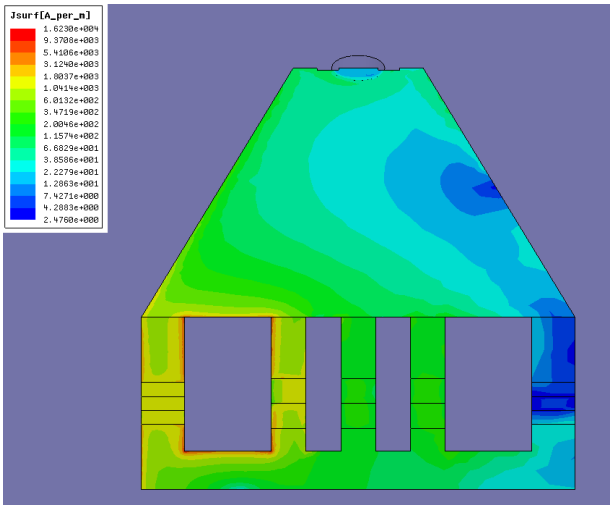

Figure 6.14: Surface currents present at 900 MHz for combinational bias network (Graphics from HFSS).

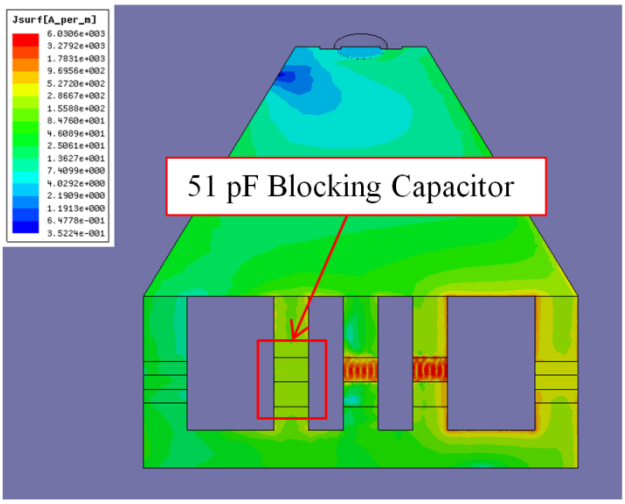

Figure 6.15: Surface currents present at 3.5 GHz for combinational bias network (Graphics from HFSS).

6.4 Practical Construction Considerations

With the newly proposed DC bias network, considerations for antenna fabrication must be taken into account. Due to the small size of the structure as well as the small chip capacitors used as DC blocks, the construction of the antenna, while easily manufacturable using industry standards, is somewhat tedious in the current lab setting.

The device requires each of the blocking capacitors on all inductive shorting straps to be soldered at two nearby points. Since the entire antenna structure is highly conductive (brass), careful soldering is required to attach the chip capacitor and the antenna to the ground plane. Also, the top sector of the antenna is fabricated with the inductive loads parallel to the sector. After the entire sector plus the loads is milled out, the loads are bent 90 degrees toward the ground plane.

Figure 6.16 shows a concept model that was built and tested for the antenna structure utilizing a single varactor placed in the corner load. The test antenna in this photograph is scaled to be 1.5 times the size of the HFSS model. The highlighted box shows the gap where the varactor is soldered. The dimension of the gap is on the order of tenths of a millimeter, illustrating the need for precise soldering. To construct the antenna with all five loads containing either a chip-capacitor or varactor, the amount of soldering needed to ensure good DC isolation is large enough to warrant a different approach to the fabrication of the inductive loads. To address this construction difficulty, a shorting strap was introduced to help alleviate half of the difficult solder points.

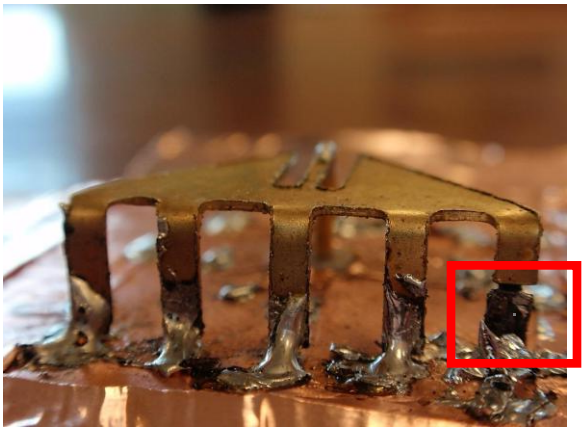

Figure 6.16: Proof of concept fabricated model.

Instead of each leg connecting directly to the ground plane at one point, all five inductive loads will be milled out with a narrow strip of material (the shorting strap) connecting them together. In addition to easing the milling process, this allows for a solid connection to ground while allowing heat to dissipate more easily during the soldering of the blocking capacitors. This configuration can be observed in Figure 6.17 where the shorting strap is highlighted in red.

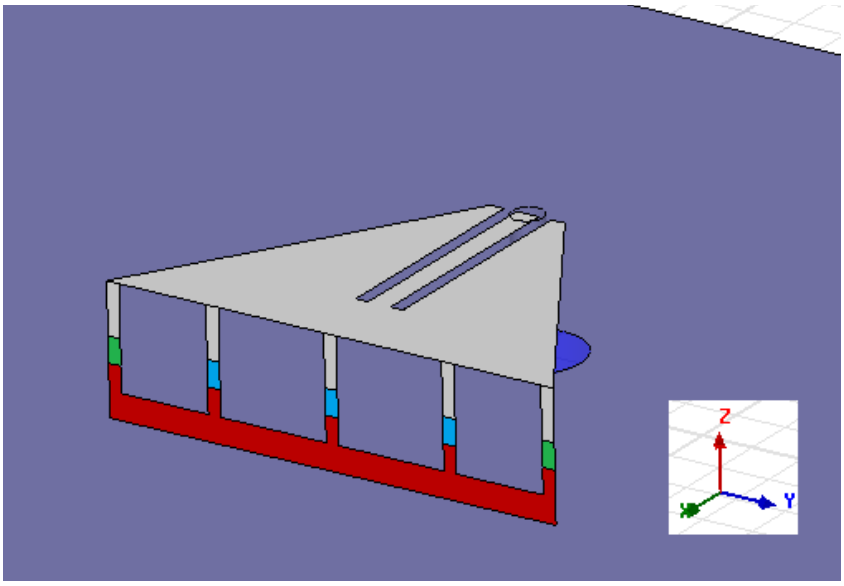

Figure 6.17: Antenna geometry with shorting strap (Graphics from HFSS).

The addition of the shorting strap does have a small effect on the performance of the antenna. Increasing the shorting strap width effectively changes the length of the inductive loads, shortening them and therefore making them less inductive. This has the effect of slightly increasing the frequency of operation of the antenna, similar to the shift in operating frequency observed by reducing the height of the antenna above the ground plane. Because this frequency shift is directly related to the height of the antenna, increases in operating frequency from the addition of the shorting strap can be countered by increasing the height of the antenna above the ground plane. In effect, the shorting strap gives another fine frequency tuning mechanism for the design.

6.5 Results

The design of a realistic DC bias network that does not affect impedance match of the antenna is a difficult problem. In order to reliably predict the performance of the network, incorporation of the frequency characteristics of the specific components is necessary. It was found that in order to ensure proper impedance matching at all frequencies, the blocking capacitors needed to be chosen such that they were not close to a self-resonant frequency. Also, due to the nature of the surface currents present on the structure at different frequencies, it was necessary to place capacitors that had desirable impedance characteristics in the loads immediately adjacent to the active varactor.

By placing the two blocking capacitors correctly and adjusting the position of the inductive loads relative to the two tuning varactors, a DC bias network that did not seriously degrade the impedance match of the antenna was achieved without the use of an external impedance matching network. While this approach increases the complexity of designing the antenna element, it allows the antenna to perform as if the bias network were “invisible.”

Chapter 7

FINAL DESIGN

7.1 Approach

Utilizing the results of the electromagnetic simulations performed for the previous studies, a final antenna design is developed. In accordance with the original project requirements, the antenna is designed to perform for the GSM 900, GSM 1800, 3G, WiFi, and WiMAX bands, which for the purposes of this thesis occur at 0.9 GHz, 1.8 GHz, 2.0 GHz, 2.4 GHz, and 3.5 GHz respectively. In order to achieve a final design that takes into account realistic components, simulations were performed to model the behavior of the varactor diodes used when package parasitics were included.

The results of the realistic varactor modeling and the DC bias network presented in Chapter 6 were then used to determine a final antenna design. Simulations were performed in HFSS to characterize the final design's performance. The antenna was then fabricated and measured in the laboratory to confirm simulation results and observe actual frequency reconfiguration. Finally, results and comparisons between the simulated and measured final antenna design are analyzed.

7.2 Realistic Varactor Modeling

In all of the previous studies (Chapters 3, 4 and 5) involving the antenna structure, the varactors have been modeled as ideal capacitors utilizing a "lumped RLC" boundary condition in HFSS. For the purposes of the aforementioned studies, using an "ideal" capacitor was sufficient in order to characterize the performance of the structure as changes were made. However, as noted in Chapter 6, real circuit components do not behave the same over wide frequency ranges, and the parasitics from the component's packaging can seriously affect the performance of the antenna. For a working frequency tuned antenna, the practical performance of the varactors cannot be ideal [28]. Therefore, realistic varactor modeling must be incorporated into simulations to analyze practical performance issues.

7.2.1 Realistic varactor model

In order to correctly predict realistic varactor performance, a model that takes into account the packaging effects of the component must be used. A typical circuit model for a packaged varactor diode is pictured in Figure 7.1 [29]. In the model, C_J (V) is the tuning junction capacitance of the diode, C_P is the parasitic package capacitance, L_P is the parasitic package inductance, and R_S (V) is the series resistance of the diode.

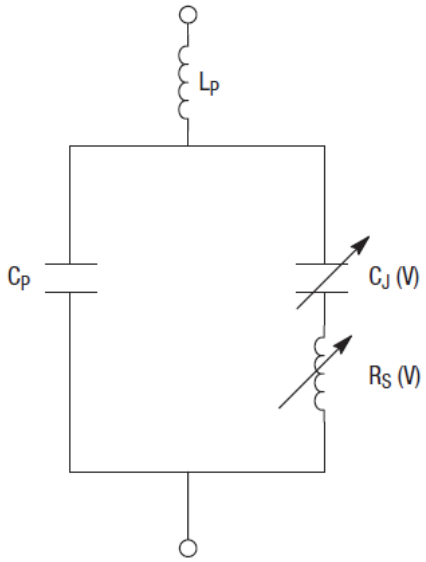

Figure 7.1: Model of a packaged varactor diode.

While R_S does vary with the bias voltage, for the GC15000 series, it remains relatively stable over the frequency range and is thus considered as a static resistance [30] for each varactor. R_S for the varactors can be easily calculated using the measured Q of the varactor at a specific frequency (for the GC15000 series f = 50 MHz). Using this method $R_S = \frac{1}{2\pi f C Q_S}$, where f is the frequency where Q was measured, C is the junction capacitance at 4 V, and Q_S is the measured varactor quality factor at V = 4 and f = 50 MHz.

The other parasitic values for the realistic varactor are given strictly based on the package type. For the 150A package style used in this design, the parasitic component values are listed in Table 7.1 and the package itself is shown in Figure 7.2 [31].

Table 7.1: Parasitic component values for the 150A package style.

	GC15002	GC15012
C_P	0.1 pF	0.1 pF
L_S	0.6 pF	0.6 pF
R_S	2.45 Ω	0.241 Ω

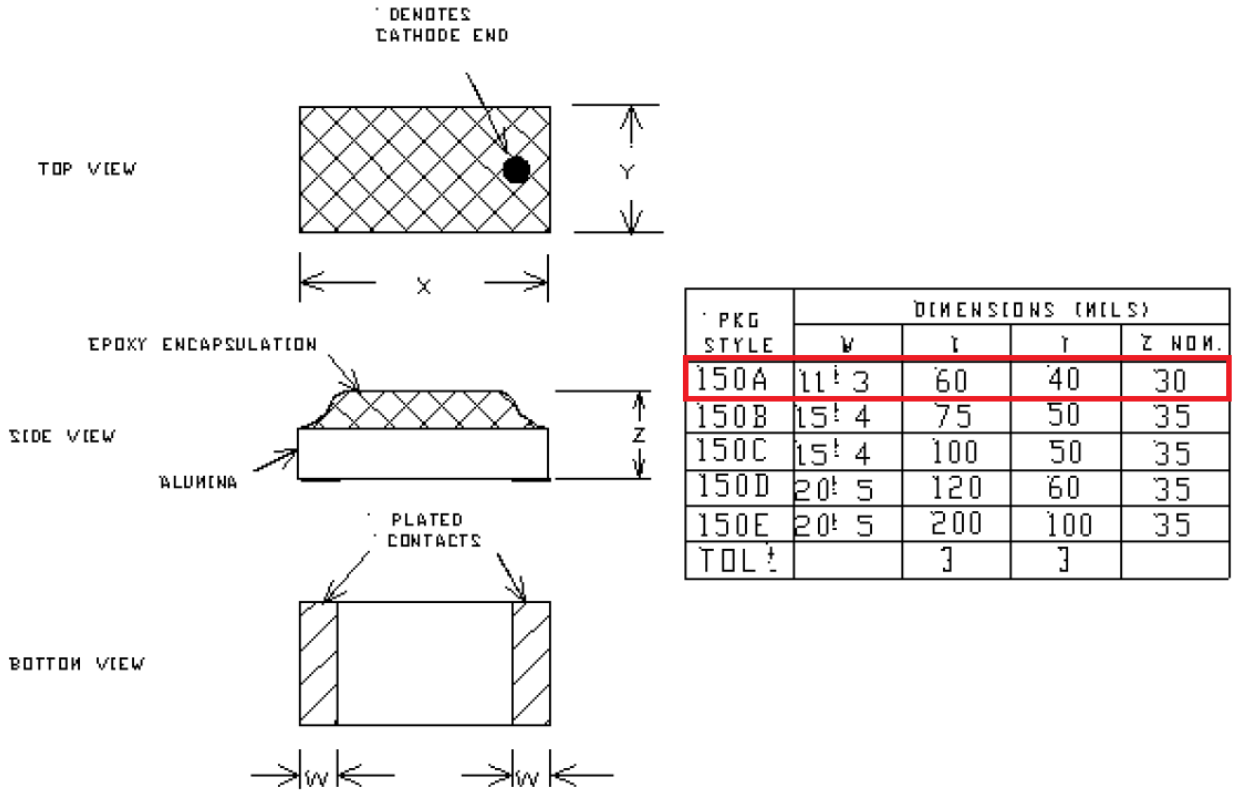

PKG STYLE	DIMENSIONS (MILS)			
	W	X	Y	Z NOM.
150A	11 ± 3	60	40	30
150B	15 ± 4	75	50	35
150C	15 ± 4	100	50	35
150D	20 ± 5	120	60	35
150E	20 ± 5	200	100	35
TOL ±		3	3	

Figure 7.2: Microsemi package style 150A – surface mount (From [31]).

In order to model the realistic varactor in HFSS, a combination of "lumped RLC" boundaries was used. In HFSS the edges of a "lumped RLC" boundary are considered a parallel connection. Because of this, the parasitic package capacitance cannot be easily modeled using the "lumped RLC" boundary; therefore, in order to incorporate the effect of the package capacitance, the value of C_P was simply added to C_J, typical of how capacitors are added in parallel.

Figure 7.3 demonstrates how the realistic varactor model was inserted into the simulation design. Following the circuit model in Figure 7.1, the parasitic inductance is placed at the top, followed by the combination of the capacitances, and lastly the parasitic resistance on the bottom.

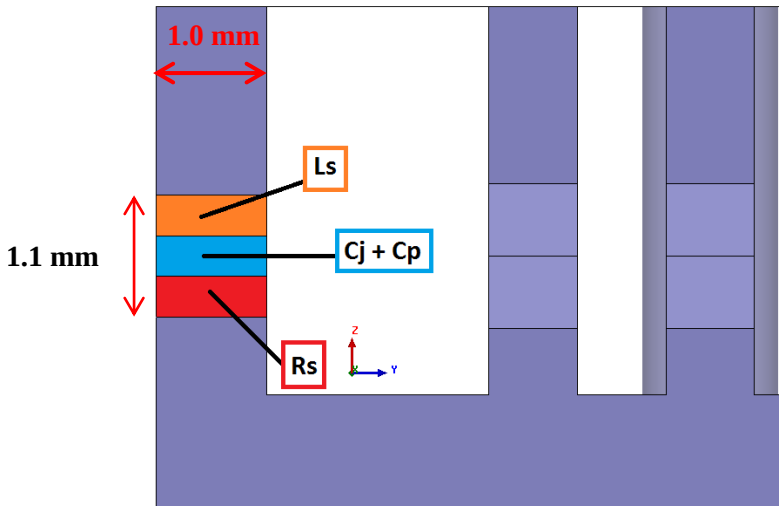

Figure 7.3: Configuration of the "lumped RLC" boundaries to model a realistic varactor (Graphics from HFSS).

Furthermore, in order to assure that the varactor was modeled as accurately as possible, the three "lumped RLC" boundaries are inserted into the same overall dimensions that the actual packaged varactor will occupy when added to the antenna structure (1.1 mm x 1 mm).

7.2.2 Simulations with realistic varactor model

To determine the effect of the realistic varactor model, simulations were performed in HFSS to observe the changes to the overall antenna performance. The parasitic values used for the simulations are given in Table 7.1 and the antenna design simulated is the same as the double varactor design in Figure 5.22, with the new realistic varactor model inserted. Figures 7.4 and 7.5 show the simulated results of inserting the realistic varactor into the existing antenna design.

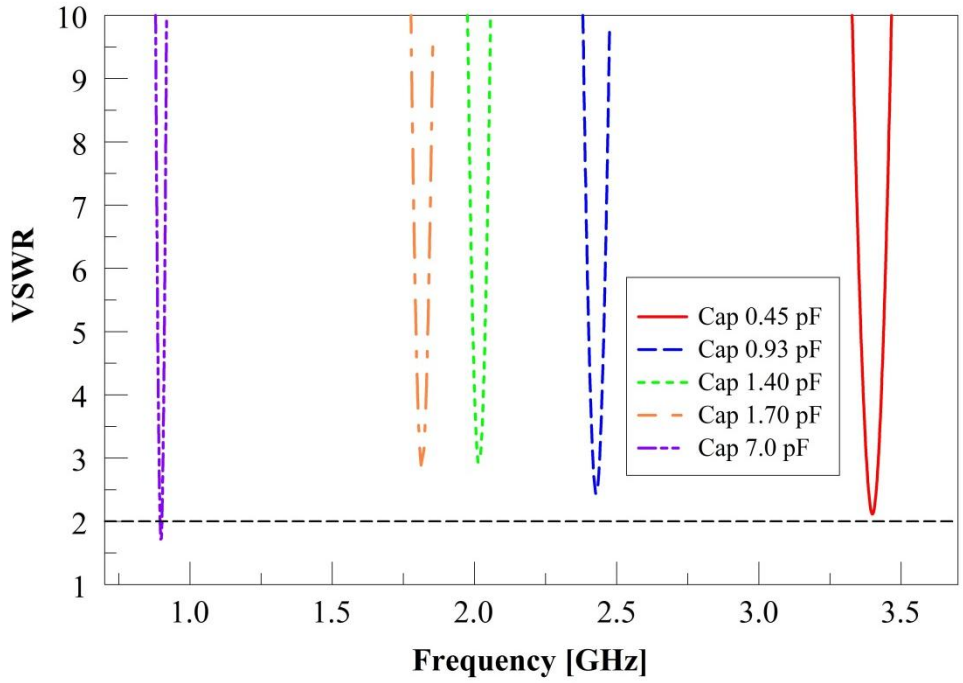

Figure 7.4: Simulated plot of VSWR versus frequency for the realistic varactor model.

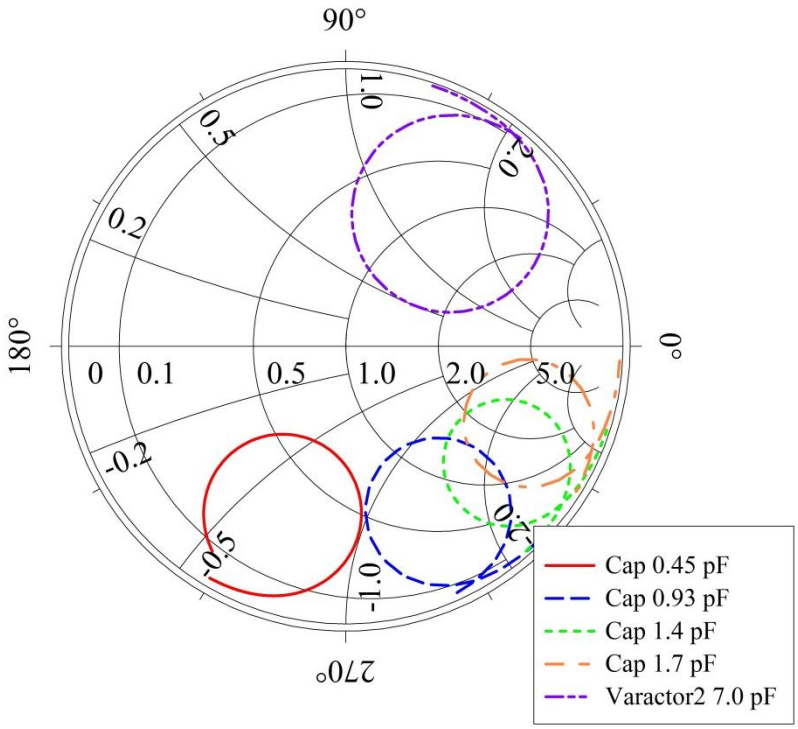

Figure 7.5: Simulated Smith chart from 0.9 to 3.5 GHz for the realistic varactor model.

What is immediately apparent from the addition of the realistic varactor model is that the impedance match of the antenna is seriously degraded (Figure 7.4 and 7.5). Two factors of the model could have a large impact on the overall match of the antenna: the series resistance and the package inductance. Simulations were performed to determine which of these most degraded the impedance match. The results of the simulations showed that the series package inductance L_s had a much more pronounced effect on the impedance match of the antenna than the series resistance. This is consistent with earlier analysis of the antenna structure where it was shown that, in order to obtain a good impedance match, the number, width, and position of the inductive loads needed to be carefully chosen. Any small changes in the inductance of the loads would have a large effect on the overall impedance match of the structure.

In order to counteract the additional inductance of the varactor packages, it was believed that a reduction in the overall inductance of the antenna was necessary. To accomplish this, the inductive feed that was added specifically to increase the inductance of the antenna was varied to see if reducing its length (Figure 7.6) could help with the impedance matching of the antenna. Simulations were performed at the 1.8 GHz band (the band most affected by the addition of the parasitic inductance) for feed lengths between 9 mm and 0.1 mm. The results of this test can be observed in Figures 7.7 and 7.8.

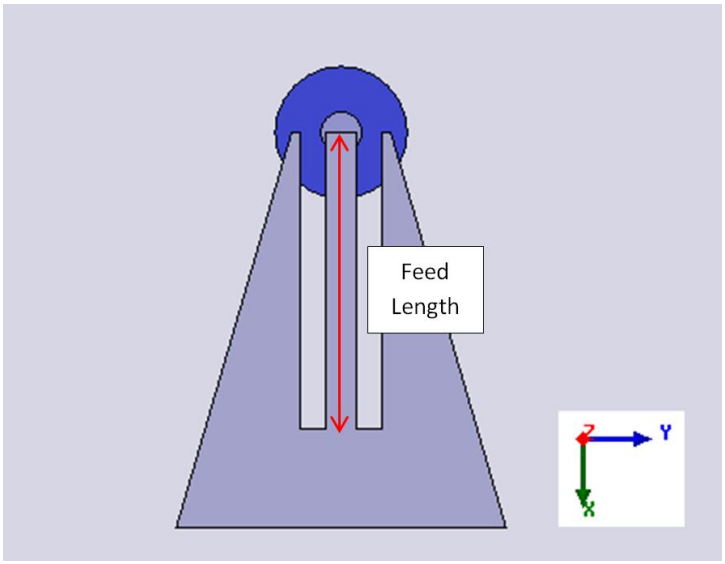

Figure 7.6: Changing the inductive feed length (Graphics from HFSS).

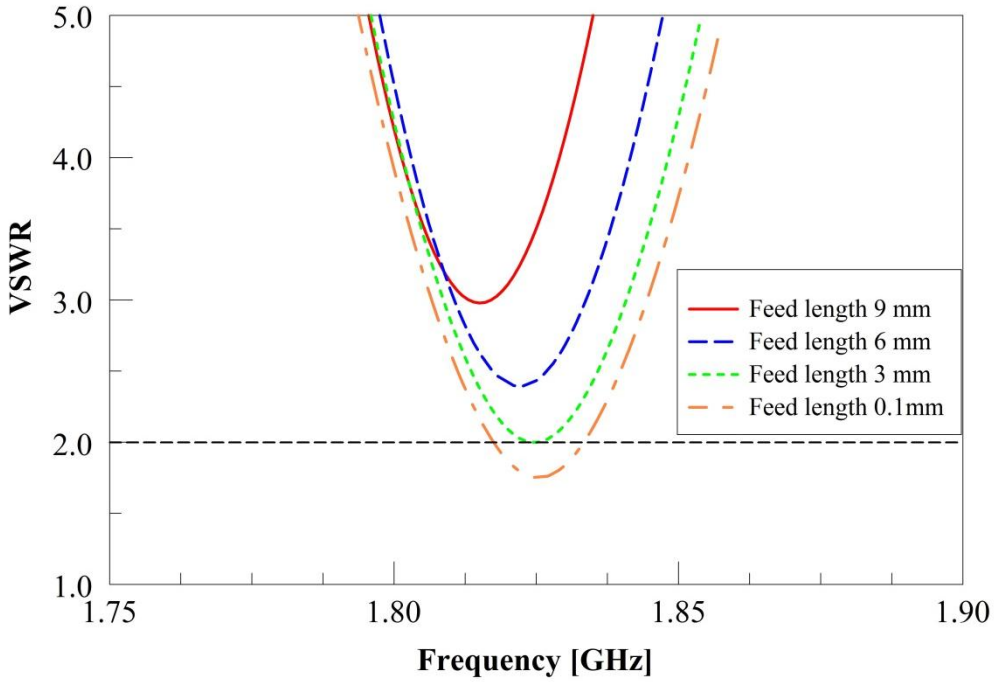

Figure 7.7: Simulated plot of VSWR vs. frequency for changing the length of the inductive feed.

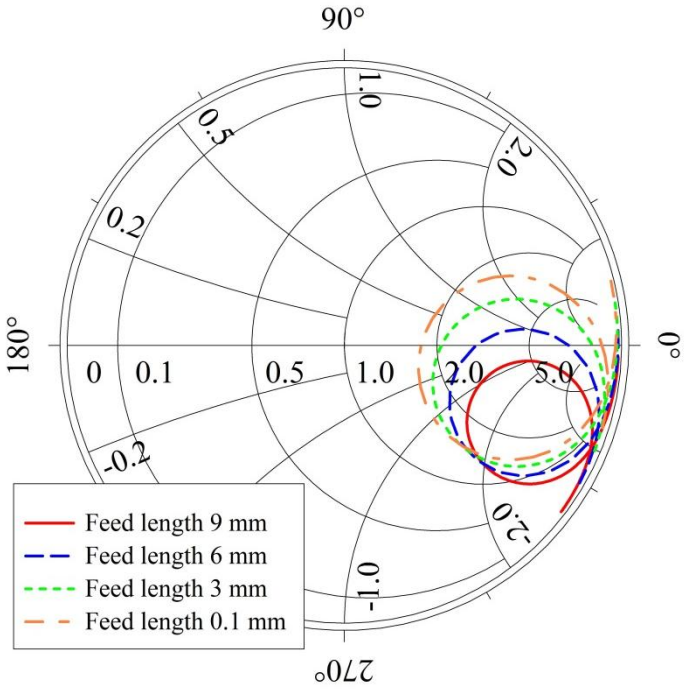

Figure 7.8: Simulated Smith chart from 1.75 GHz to 1.90 GHz for changing the length of the inductive feed.

As predicted, reducing the length of the inductive feed has a dramatic effect on the overall impedance match of the antenna. It was found that removing the inductive feed completely (0.1 mm) would allow for the added parasitic inductance of the realistic varactors to be overcome and the antenna could again maintain a good impedance match for the 1.8 GHz band.

Through the removal of the inductive feed and the narrowing of the center inductive loads, the simulated antenna with the realistically modeled varactors was able to maintain an impedance match at all five bands of interest. Simulations were performed to confirm, and results are shown in Figures 7.9 and 7.10.

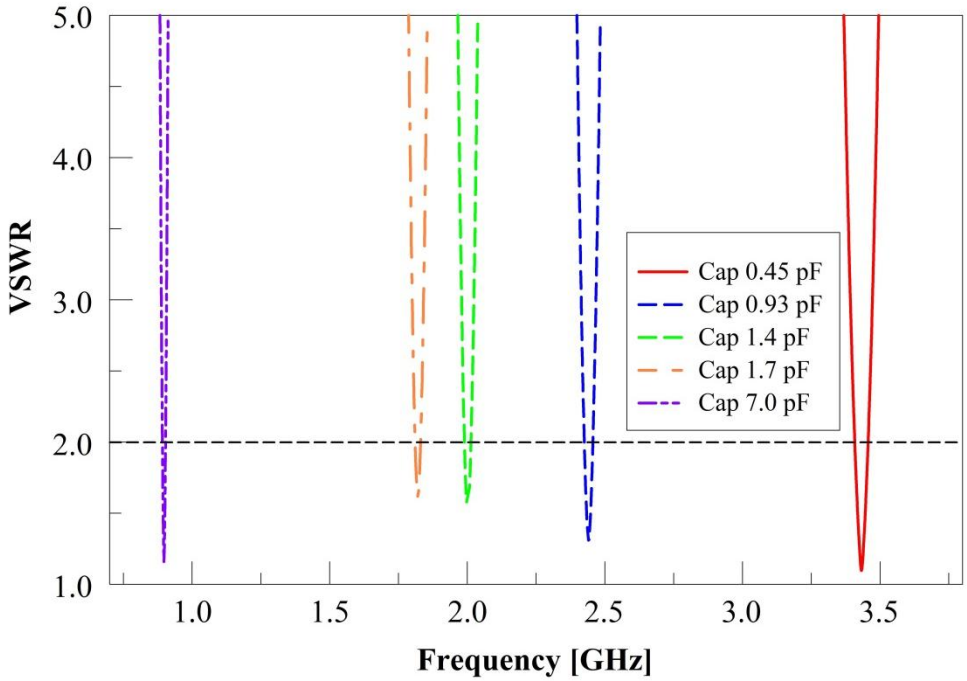

Figure 7.9: Simulated plot of VSWR vs. frequency for the realistic varactor model showing impedance match for all bands.

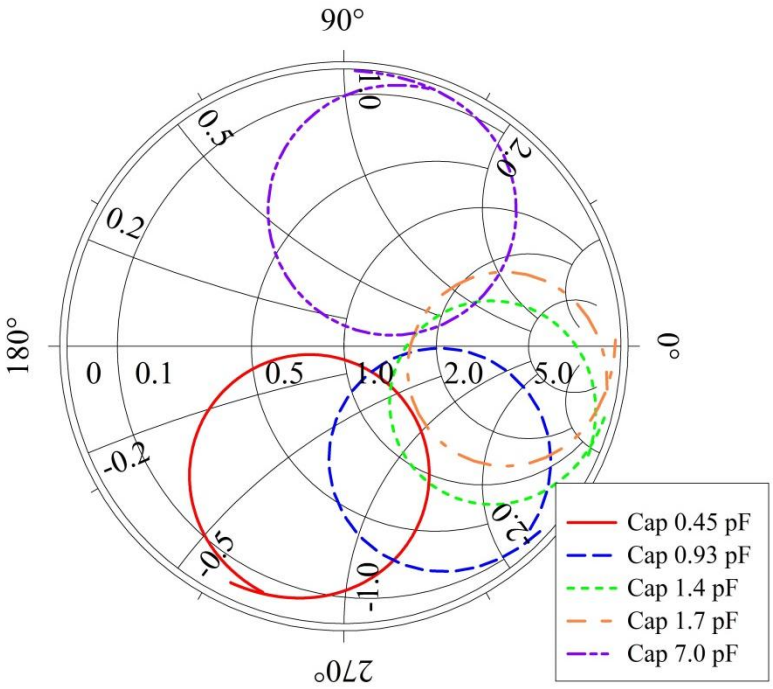

Figure 7.10: Simulated Smith chart from 0.9 GHz to 3.5 GHz for the realistic varactor model showing impedance match for all bands.

7.3 Final Design Simulations

Using the results of the tuning range study, the construction of the DC bias network, and the modeling of the realistic varactors, a final antenna design was developed. The structure dimensions are shown in Figures 7.11 and 7.12. The blue shading corresponds to the varactors and the green shading corresponds to the blocking capacitors. For the dimensions, only the overall size of each component is shown. The simulations included both the realistic varactor model developed in Section 7.2.1 and the realistic DC bias network developed in Section 6.3.2.

The antenna is simulated on a 40 x 40 cm ground plane in order to avoid ground plane radiation effects. A discrete sweep with a 1 MHz step size is used along with the efficiency convergence constraint used in all previous simulations. The varactor values shown indicate the effective capacitance of the varactor without the added package capacitance value of 0.1 pF. Also, as mentioned in the development of the DC bias network, the effective component values of the blocking capacitors are adjusted for each frequency band and inserted into the simulation according to Tables 6.1 and 6.2, respectively.

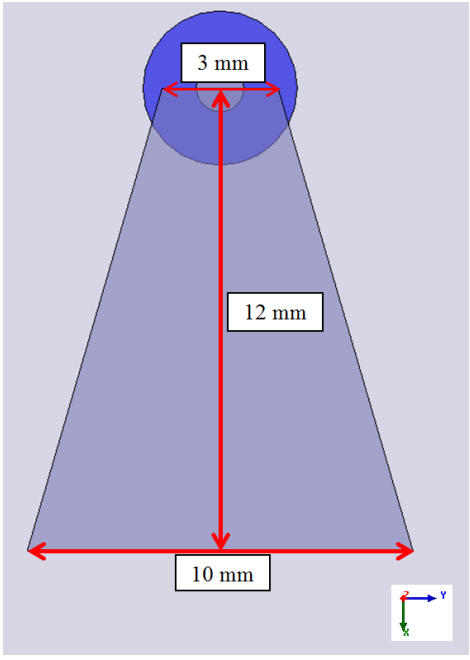

Figure 7.11: Final design dimensions top down (Graphics from HFSS).

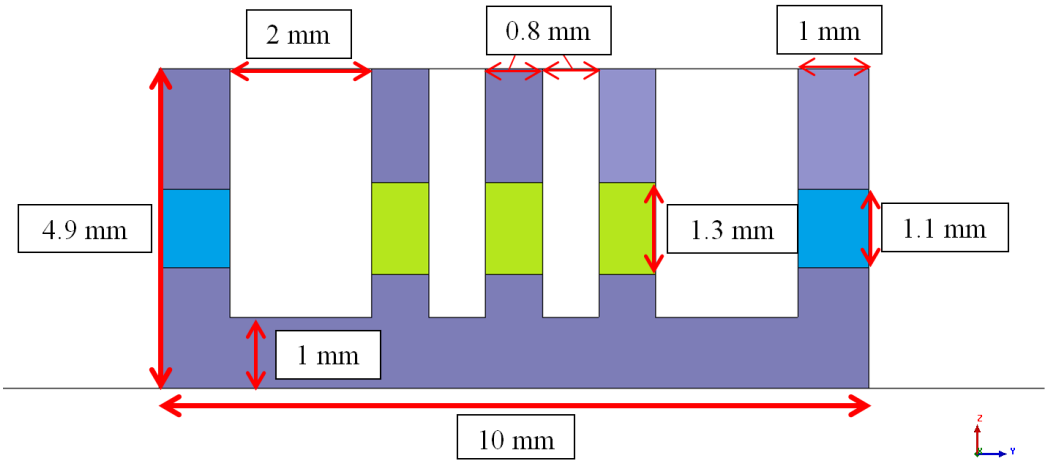

Figure 7.12: Final design dimensions side profile (Graphics from HFSS).

7.3.1 Simulation results

The final structure pictured in Figures 7.11 and 7.12 was simulated to observe the tuning range of the antenna. Figures 7.13 and 7.14 show the VSWR and Smith chart plots of the final design at all five frequency bands. It can be noted that even with the addition of the realistic varactor and blocking capacitor models, a good impedance match can be maintained at all frequency bands.

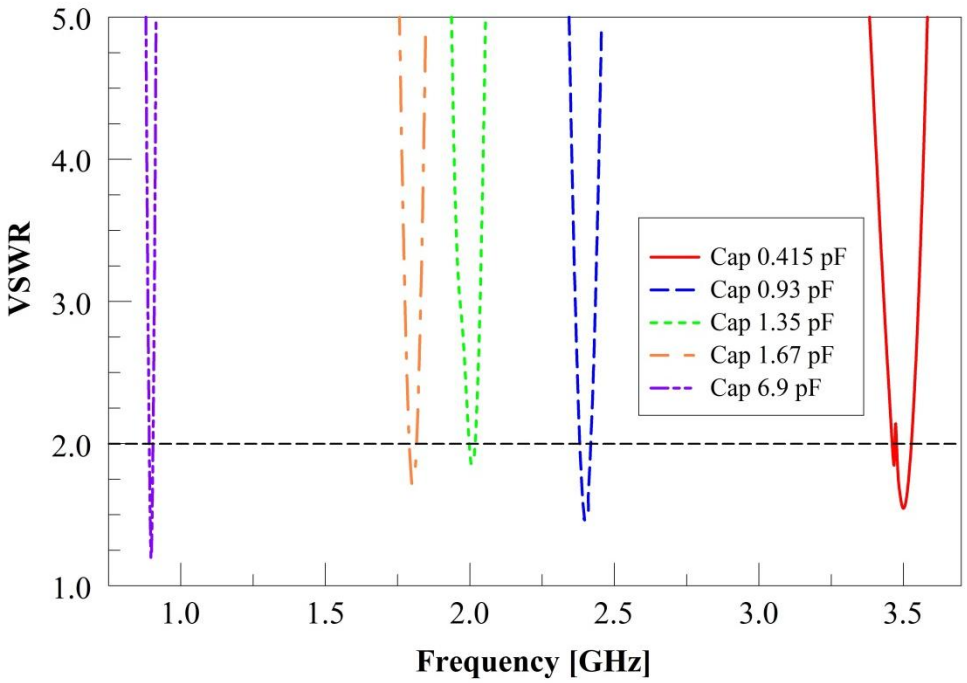

Figure 7.13: Simulated plot of VSWR vs. frequency for the final antenna design simulation.

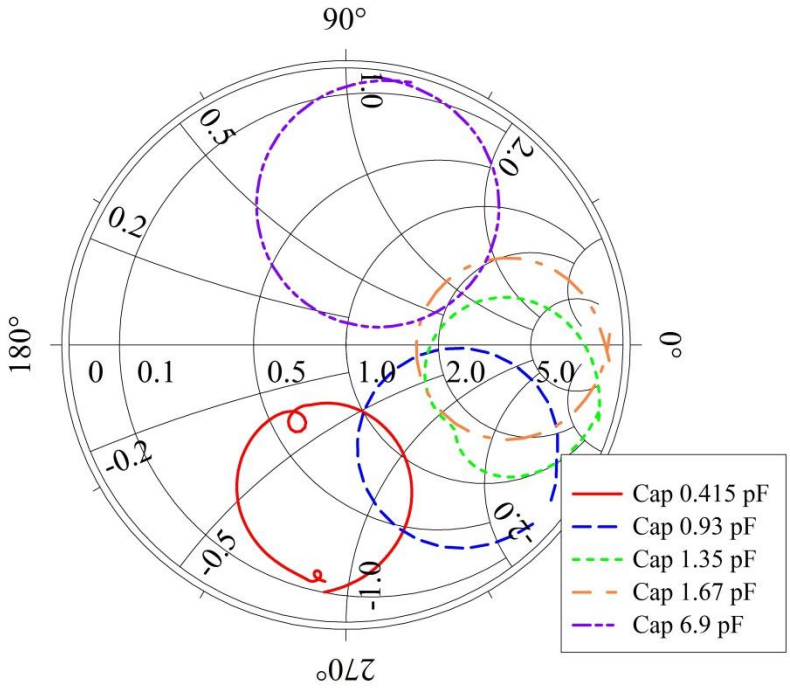

Figure 7.14: Simulated Smith chart from 0.9 GHz to 3.5 GHz for the final antenna design simulation.

In Figures 7.15 through 7.19, the 3D gain plots of the antenna at each frequency band are shown. These figures show the G_ϕ and G_θ for the antenna in dB. Overall the patterns are consistent with a monopole antenna over a ground plane. It should be noted that as the frequency becomes higher, the number of minor lobes of the antenna increases. This pattern 'scalloping' occurs due to currents present on the ground plane. While the ground plane is not radiating significantly, some interference is observed.

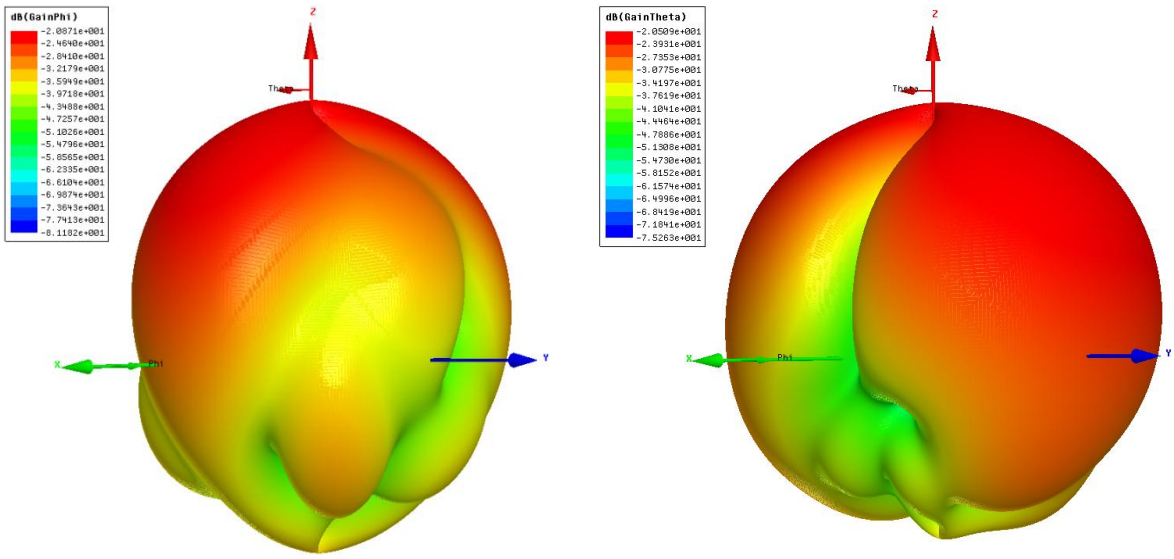

(a) (b)

Figure 7.15: 3D radiation plots at 0.9 GHz for G_ϕ (a), and G_θ (b) (Graphics from HFSS).

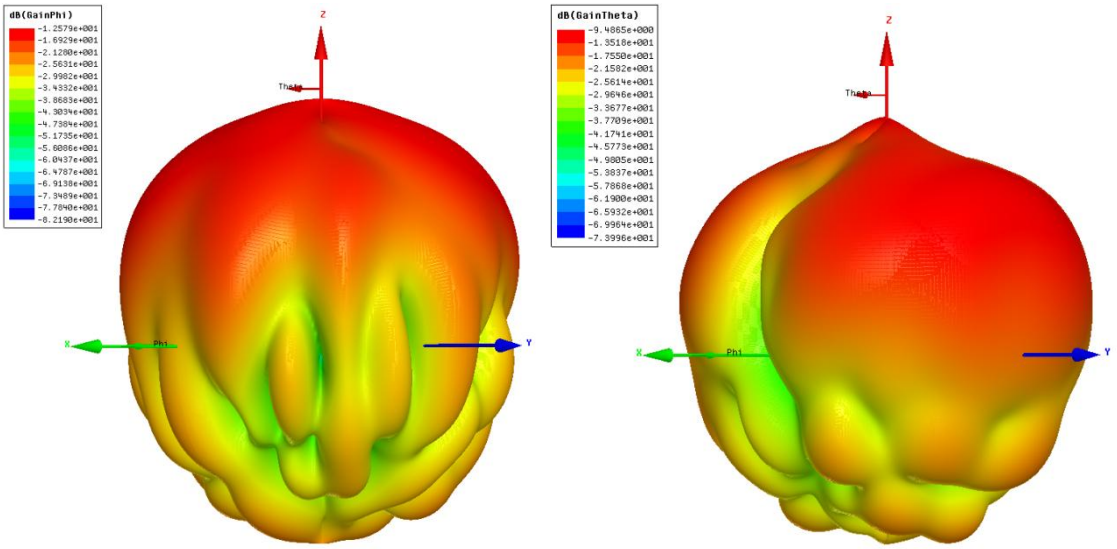

(a) (b)

Figure 7.16: 3D radiation plots at 1.8 GHz for G_ϕ (a), and G_θ (b) (Graphics from HFSS).

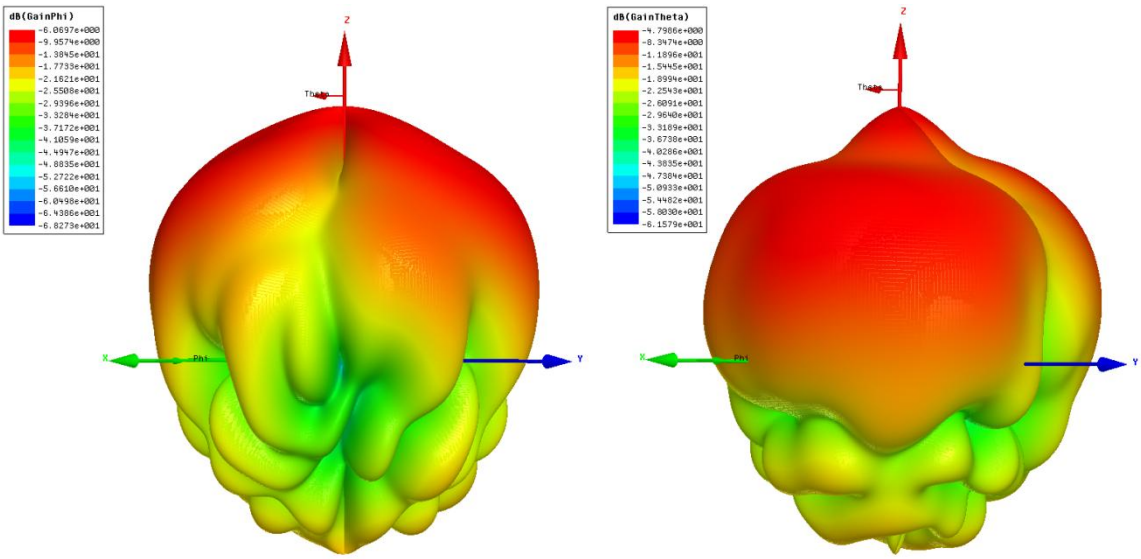

(a) (b)

Figure 7.17: 3D radiation plots at 2.0 GHz for G_ϕ (a), and G_θ (b) (Graphics from HFSS).

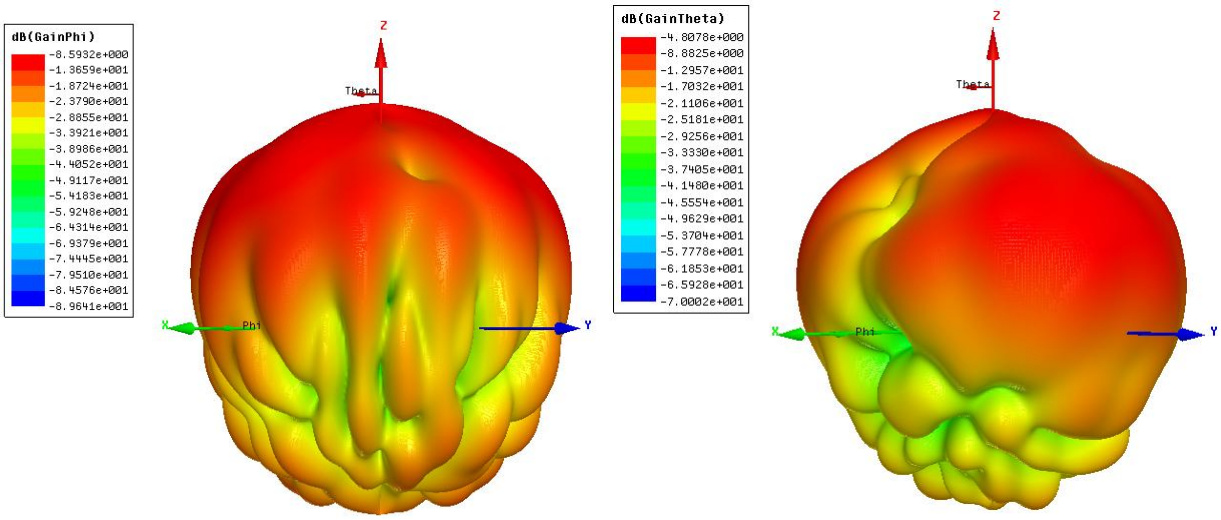

(a) (b)

Figure 7.18: 3D radiation plots at 2.4 GHz for G_ϕ (a), and G_θ (b) (Graphics from HFSS).

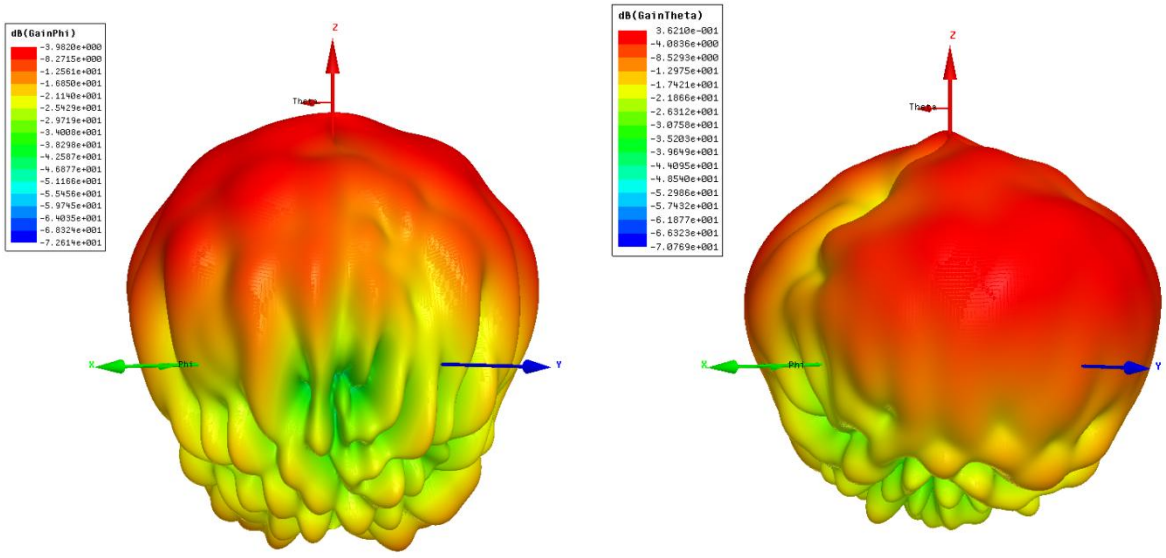

(a) (b)

Figure 7.19: 3D radiation plots at 3.5 GHz for G_ϕ (a), and G_θ (b) (Graphics from HFSS).

7.4 Fabrication and Measurements

7.4.1 Equipment and materials

In order to fabricate the extremely small antenna proposed in the previous sections, precision tools and techniques must be utilized. For the machining of the antenna sector and the inductive loads, a Quick Circuit 5000 milling machine from T-Tech, Inc., was used alongside the ISO-PRO 9000 software package. To use the milling machine, geometry files were imported from HFSS directly to ISO-PRO, allowing for the precision milling of antenna structure.

Because of the extremely small size of the features associated with the antenna structure, a 0.0310 in (0.7874 mm), fishtail router from T-Tech was used to machine the structure out of a 0.45 mm thick brass sheet. Due to the fragility of the 31 mil router, extreme caution was necessary to fabricate the structure successfully without breaking the bit or gouging the metal. The antenna is fed with a standard SMA probe feed soldered to a copper ground plane. In previous designs solder was used to attach the inductive loads and their components to the antenna. Due to the extremely small feature sizes associated with the components (blocking capacitors and varactors) and the spacing between the shorting strap and the bent inductive loads, conductive epoxy was used for better fabrication control. Two different epoxies were used to fabricate the structure: MG Chemicals silver conductive epoxy and Resin Technology Group's Compound Silver 402 epoxy adhesive. Both of these epoxies are designed to cure at room temperature for cold soldering components. The volume resistivity of the MG Chemicals epoxy is 0.38 Ω-cm when cured at 25 ^{o}C and has a curing time of 4 hours at room temperature. The Resin Technology Group's Compound Silver 402 epoxy, on the other hand, has a volume resistivity of 0.030 Ω-cm when cured at 25 ^{o}C and fully cures in 18 hours at room temperature.

A BTS1601 bias tee procured from Federal Custom Cable is used in order to inject both the RF and the DC bias into the feed of the antenna. The bias tee has an operating range of 10-6000 MHz, a maximum insertion loss of 2.2, and 30 dB of isolation. Measurements are performed using an Agilent 8363B network analyzer and Orbit FR 959 antenna pattern measurement software.

7.4.2 Construction

The antenna sector was fabricated in two different pieces: the main sector plus half the length of the inductive loads, and the shorting strap plus the remaining length of the inductive loads. The inductive loads were fabricated according to the design to have two different widths. For the loads containing the varactors a width of 1.0 mm was used, and the loads with the blocking capacitors were 0.8 mm wide. The ground plane was fabricated from a 70 x 70 mm piece of copper with a hole drilled to allow the SMA probe feed's dielectric to be flush with the surface of the ground plane. The hole is drilled such that the physical center of the antenna is at the exact center of the ground plane. To guarantee the correct height of the antenna, the SMA probe feed is carefully measured, cut, and filed.

To assemble the antenna, the probe feed is first soldered to the ground plane using a blow torch to assure a solid connection. Then the inductive loads attached to the sector portion of the antenna are bent to form a 90 degree angle with the sector. The position of the shorting strap is then carefully measured so that it can be attached to the ground plane in the correct orientation. Once the shorting strap is epoxied, a piece of foam is cut and placed such that the sector portion of the antenna is supported horizontal to the ground plane. This ensures that the sector does not tilt and also strengthens the structure. Once the foam support is in place, the sector is soldered to the probe feed and the correct alignment between the two pieces is ensured.

The varactors and the blocking capacitors are all then epoxied by hand to the correct inductive loads. First the epoxy is applied, using a toothpick, to either side of the gap between the sector and the shorting strap. Then the component is carefully lowered onto the epoxy and, once placed, gently nudged into its final position. During the placement of the components great care must be taken to ensure that the epoxy does not accidentally short the component. After each component is placed, a hand-held digital multi-meter is used to test for shorting paths.

After the structure is assembled and fully cured (overnight), a digital multimeter is used again to ensure that a proper DC block has been achieved. Finally, the antenna is inspected for construction defects or errors. Figures 7.20 and 7.21 show the fabricated structure.

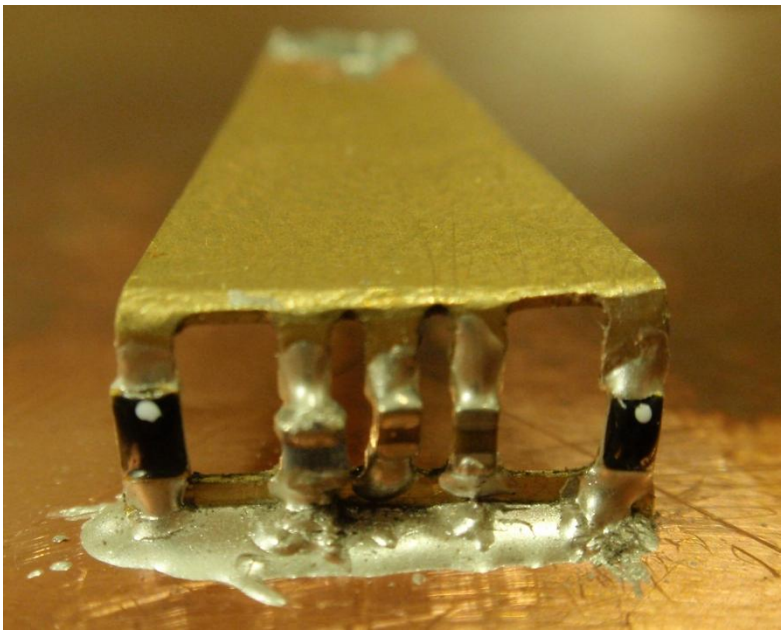

Figure 7.20: Fabricated final design antenna back view.

Figure 7.21: Fabricated final design antenna top view.

7.4.3 Measured results

In order to obtain functional measured results, the construction steps listed in Section 7.4.2 had to be repeated numerous times due to the extremely sensitive nature of the antenna structure to fabrication flaws. During preliminary measurements it was determined that in order to best test the frequency tuning ability of the antenna and produce significant results, two versions of the final design antenna in Section 7.3 needed to be built. The first design is the same as the structure described in Figures 7.11 and 7.12 and the other is a larger modified version of the final design. The final design is extremely electrically small with a *ka* equal to 0.680 at 3.5 GHz and 0.175 at 900 MHz. The incredibly small electrical size of the structure allows the possibility of additional losses either in the components or in the epoxy to severely degrade the performance of the antenna. By making the structure electrically larger, the antenna will hopefully become more insensitive to additional losses from practical construction.

The modified fabricated antenna is shown in Figures 7.22 and 7.23 and pictured in Figures 7.24 and 7.25. The main difference between the modified and final version is the length of the top sector of the antenna. The modified version has been lengthened from 10 mm to 17.5 mm, increasing the structure's electrical size such that *ka* at 3.5 GHz is 0.977. The other modifications to the structure are custom gap sizes on the inductive loads based on caliper measurements of the physical components.

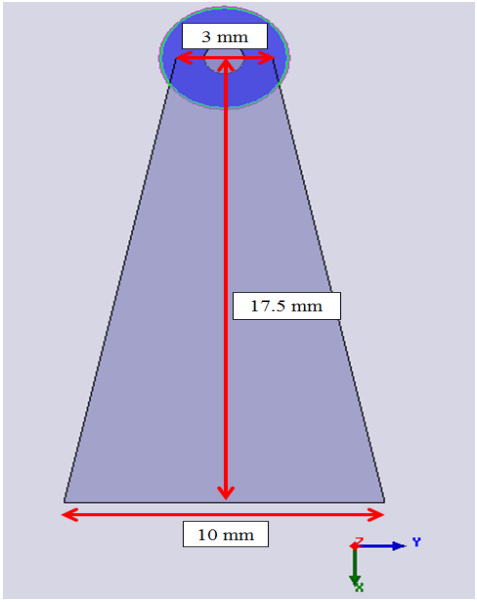

Figure 7.22: Modified final design dimensions top down (Graphics from HFSS).

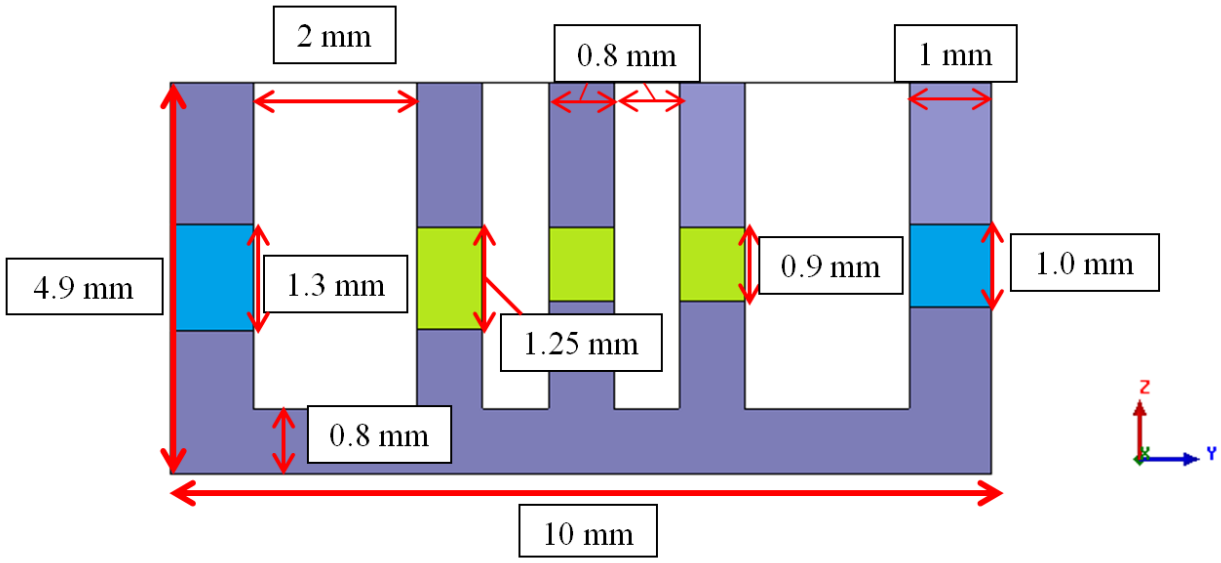

Figure 7.23: Modified final design dimensions side profile (Graphics from HFSS).

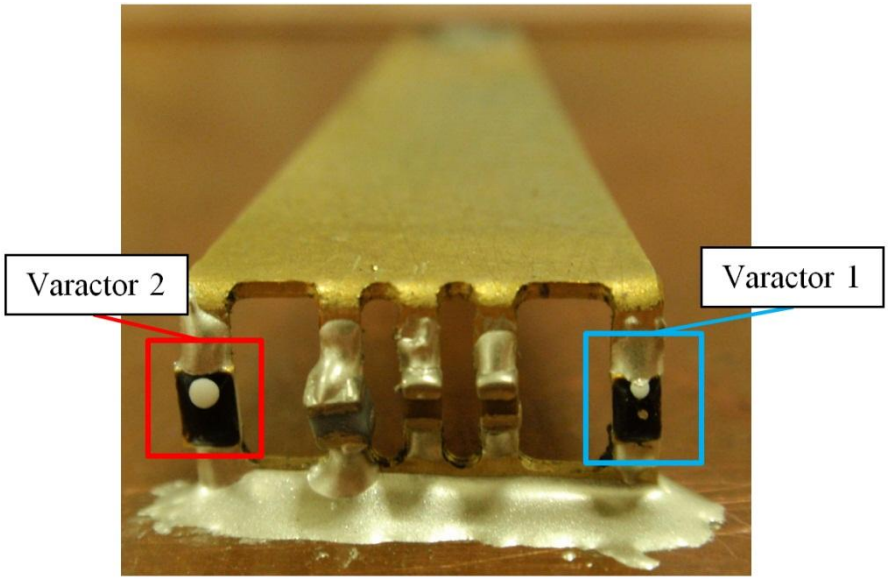

Figure 7.24: Modified final design back view.

Figure 7.25: Modified final design top view.

Both versions of the antenna were fabricated multiple times and tested for performance. During testing it was found that the silver epoxy from MG Chemicals was very brittle and was prone to cracking during testing, making consistent measured results impossible. Only a limited supply of the Compound Silver 402 epoxy was available during the measurement phases; therefore, to improve the chances of obtaining consistent measureable results, the decision to use the modified final design in conjunction with the Compound Silver 402 epoxy was made.

The final fabricated antenna was connected via high-grade microwave cables to the Agilent 8363B network analyzer and measurements were taken from 0.6 to 4 GHz to observe the entire tuning range. The antenna was placed on a large 30 cm round copper ground plane to ensure accurate measurements, and the BTS1601 bias tee was calibrated into the measurement setup. The measured structure's components were the same as previously mentioned except for one part. The Microsemi GC15012 varactor that was shipped to the laboratory was of the package type 150B instead of the expected 150A. The 150B package is larger than the 150A and contains different parasitic component values which might have an effect on the performance of the antenna.

Figures 7.26 and 7.27 show performance of the fabricated antenna for several different bias voltages. It can be noted that the impedance match of the antenna is degraded at several frequencies when compared with the final simulation results in Figures 7.13 and 7.14. The antenna does obtain a match at 13.49 V at 3.5 GHz, but as the antenna tunes lower in frequency the match quickly degrades. It can be noted, however, that the dual varactor design is working

correctly. As the bias voltage increases past 14 V, the low frequency band controlled by Varactor 2 ‘tunes’ into range and the high frequency band controlled by Varactor 1 ‘tunes’ out of the frequency range. This behavior is in generally good agreement with the simulated design.

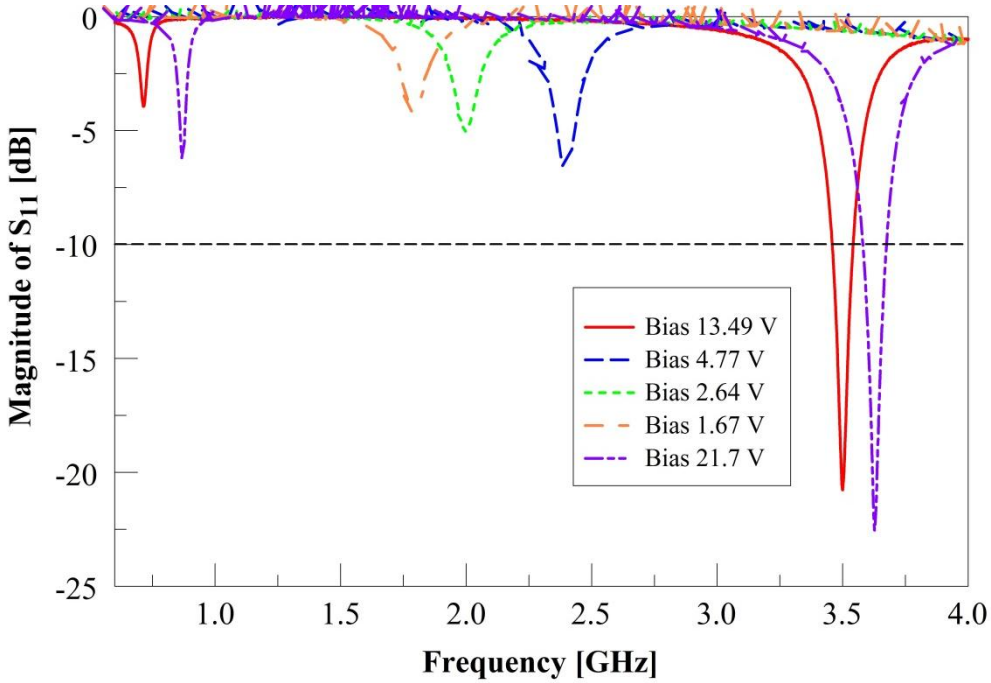

Figure 7.26: Measured plot of the magnitude of S_{11} versus frequency for the modified fabricated antenna at different bias voltages.

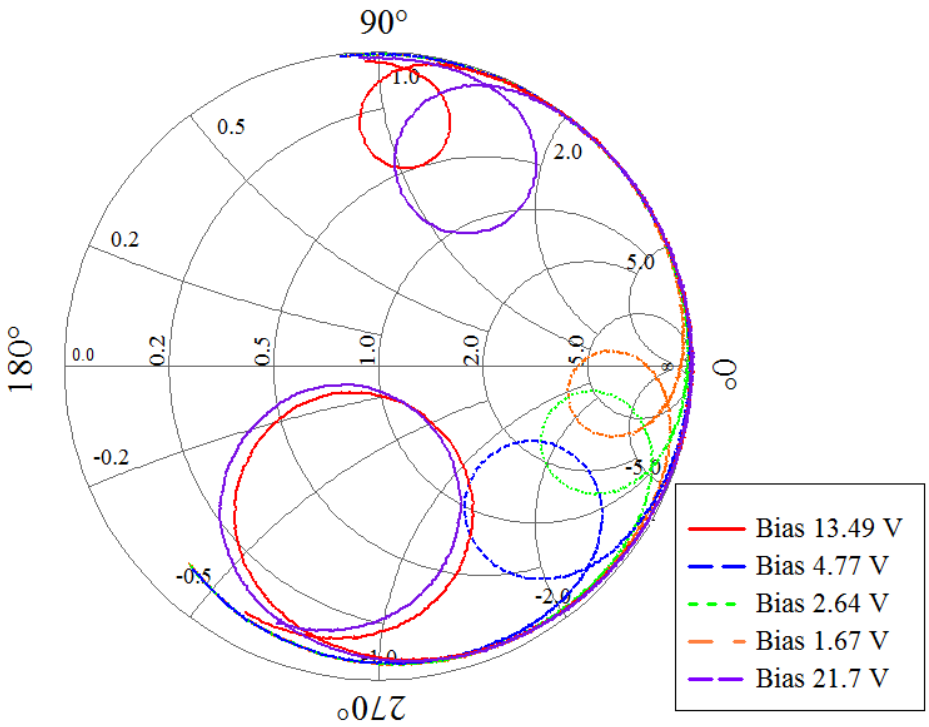

Figure 7.27: Measured Smith chart plot from 0.6 to 4.0 GHz for the modified fabricated antenna at different bias voltages.

As Figures 7.26 and 7.27 show, the measured antenna results are substantially different from the simulated results. The difference between simulation and measurement was thought to be caused by three main factors: fabrication errors (components positioned incorrectly, milling and construction errors), conductive epoxy losses (lower conductivity of epoxy vs. solder and solid electrical connections), and additional varactor losses (series resistance changing as a function of frequency and applied bias voltage). In order to reconcile these differences, a study was performed adding additional losses to the simulated model to approximate the effect of the epoxy and varactor losses.

Using the simulation model in Figure 6.11 on page 88, additional losses were added to each component separately (Varactor 2, 51 pF blocking capacitor, 850 pF blocking capacitors, and Varactor 1) and its effect on antenna performance was observed.

Looking at Figures 7.28 through 7.31, it can be noted that the antenna structure is extremely sensitive to additional losses, especially when the losses occur in a varactor. Figure 7.28 shows that an extra 1 Ω of resistance in Varactor 2 results in an unacceptable impedance match.

Varactor 1 is less sensitive, but Figure 7.30 shows that an additional 2 Ω of loss also results in an unacceptable impedance match.

Changing the amount of resistance in the two different blocking capacitors has the most profound effect whenever the resistance is added in the capacitors closest to the active varactor. At low frequencies when Varactor 2 is active, the resistance of the 51 pF blocking capacitor has the largest impact on the impedance (Figure 7.29). At higher frequencies the 850 pF blocking capacitors have a larger impact on the antenna performance (Figure 7.31).

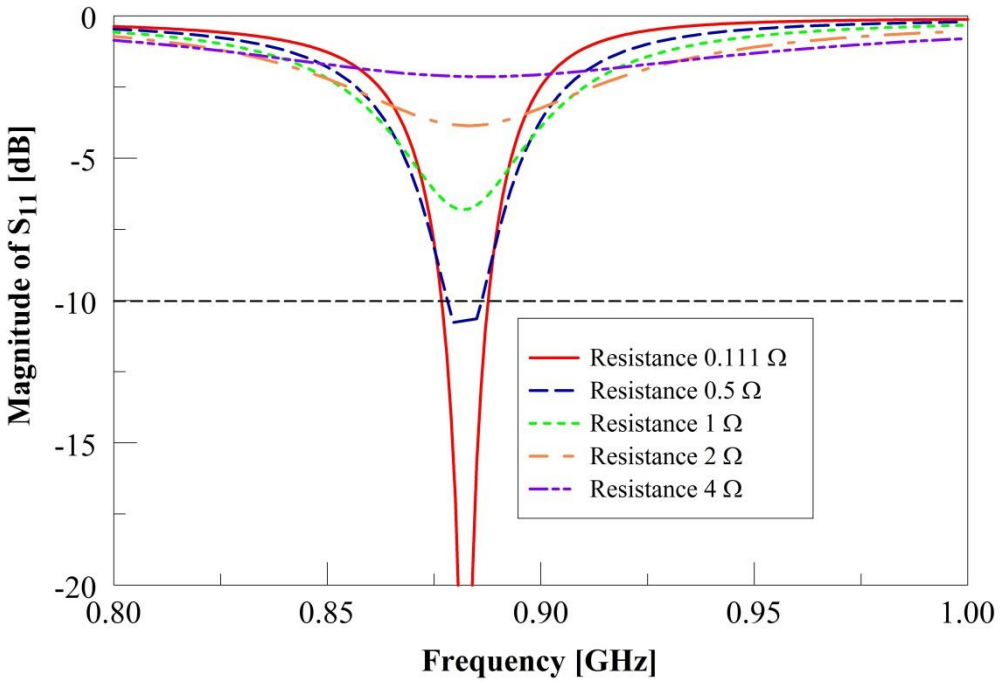

Figure 7.28: Simulated S_{11} plot vs. frequency of additional resistive loss in Varactor 2 from 0.8 to 1.0 GHz.

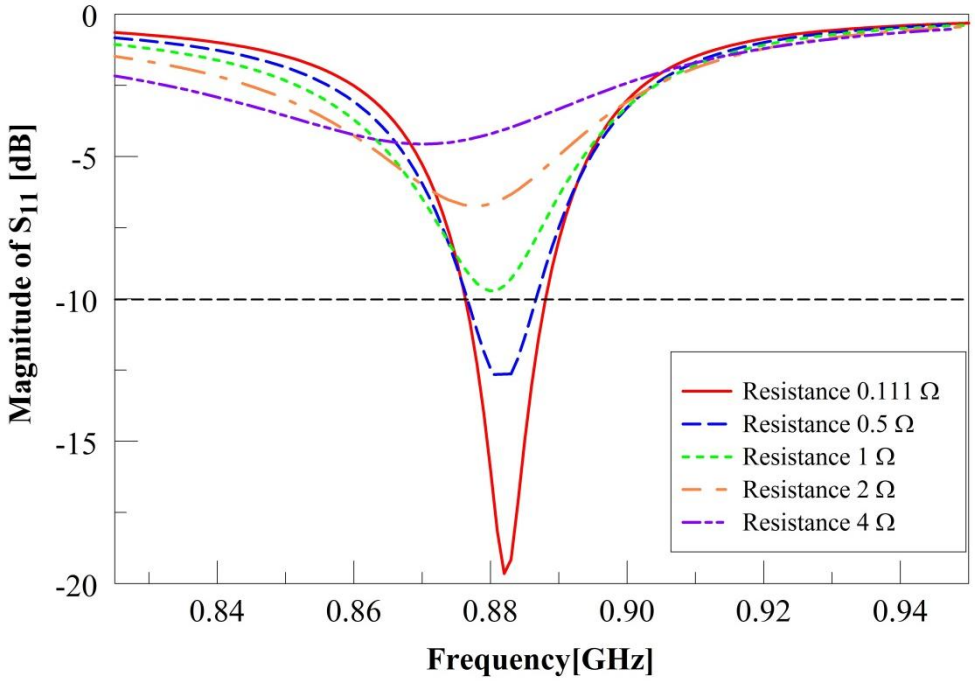

Figure 7.29: Simulated S_{11} plot vs. frequency of additional resistive loss in the 51 pF blocking capacitor from 0.8 to 1.0 GHz.

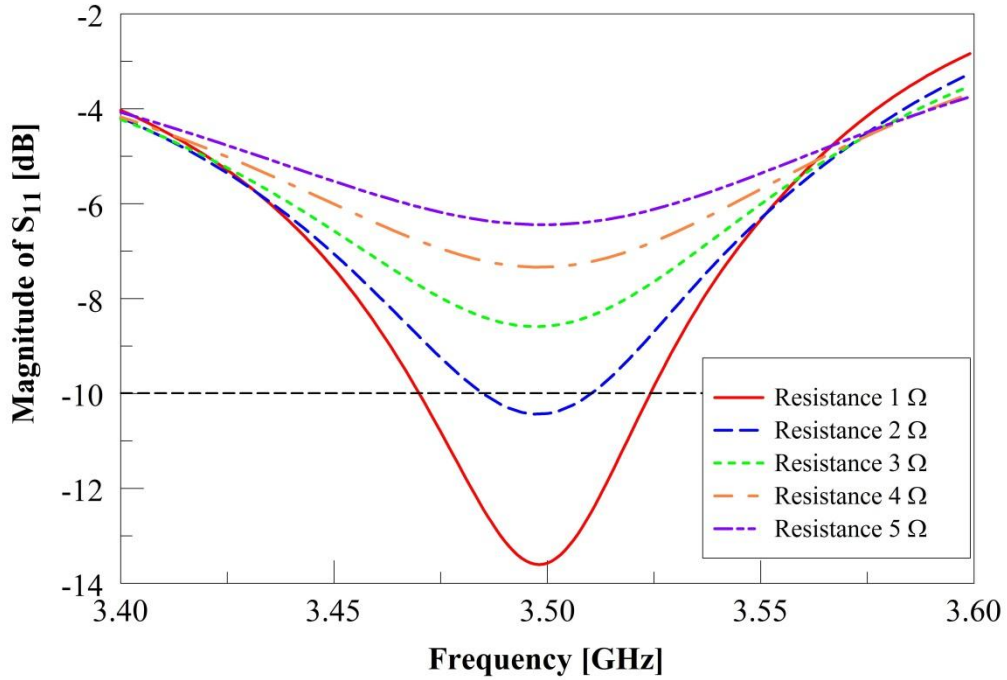

Figure 7.30: Simulated S_{11} plot vs. frequency of additional resistive loss in Varactor 1 from 3.4 to 3.6 GHz.

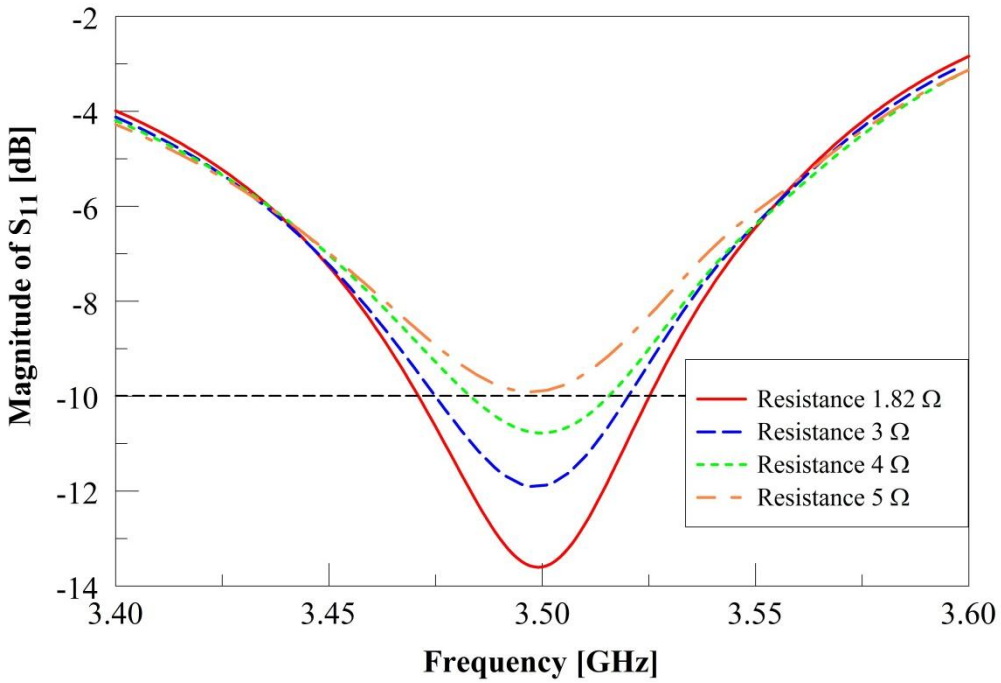

Figure 7.31: Simulated S_{11} plot vs. frequency of additional resistive loss in the 850 pF blocking capacitors from 3.4 to 3.6 GHz.

Figures 7.28 through 7.31 illustrate the extreme sensitivity of this antenna structure due to its small electrical size. To further illustrate the impact that small losses have on the performance of the antenna, Figure 7.32 shows an impedance measurement from the modified final design using the higher-loss MG Chemicals silver epoxy. It can be observed that even the difference between 0.38 Ω-cm and 0.030 Ω-cm in resistive loses is almost 10 dB at 3.5 GHz and nearly 2 dB at 0.9 GHz.

Another interesting observation can be made by observing the performance of the antenna for different bias voltages. Consistently, in both Figure 7.26 and Figure 7.32, the lower bias voltages correspond to the worst impedance matches, and the frequencies at the highest bias voltages (3.5 and 0.9 GHz) correspond to the best impedance matches. This behavior is thought to be explained by the equivalent series resistance of the varactor decreasing with higher applied bias voltages. Unfortunately, Microsemi does not give the resistance performance of its varactor diodes as a function of applied bias voltage.

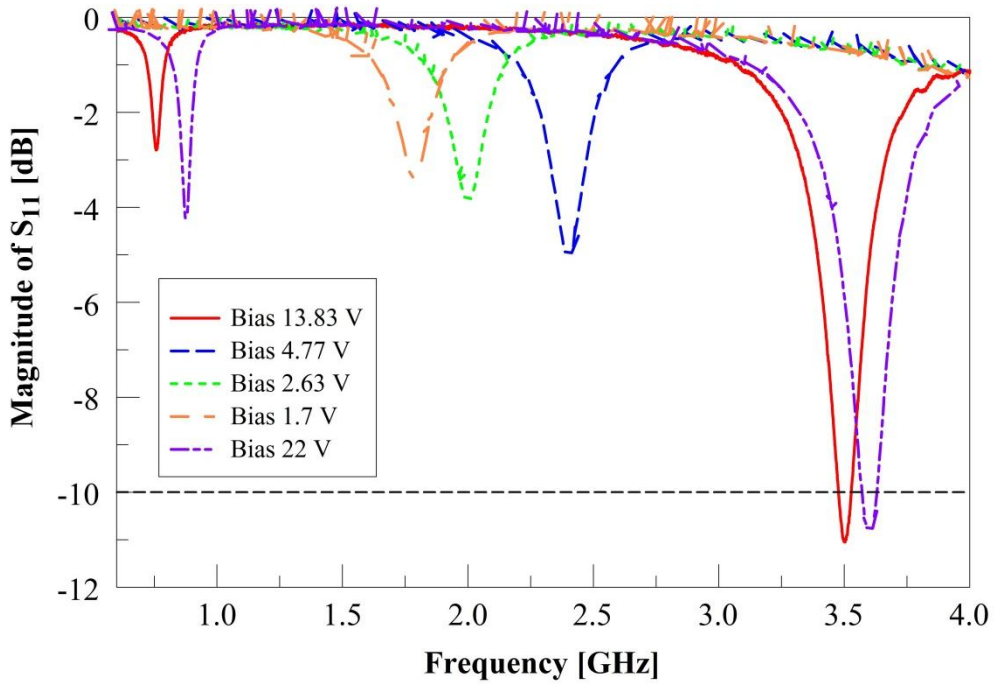

Figure 7.32: Plot of the magnitude of S_{11} versus frequency for the modified fabricated antenna at different bias voltages using the MG Chemicals silver epoxy.

Pattern measurements were also taken for the modified final antenna design. The measurements were taken using the University of Illinois anechoic chamber and Orbit 959 pattern measurement software. Figures 7.33 through 7.42 show the measured patterns (right) versus simulated patterns (left). It can be observed that the measured patterns do correspond reasonably well with the simulated patterns. Backplane radiation and extra noise from DC bias lines are present in most of the measured results in the form of decreased front to back ratios and extra lobes in the patterns. Measurements at each frequency point were taken with the antenna connected and unconnected and the results were compared. By observing what was measured when the antenna was connected versus the radiation scattering of the test setup, the conclusion that the overall pattern relates well to the simulated results can be made.

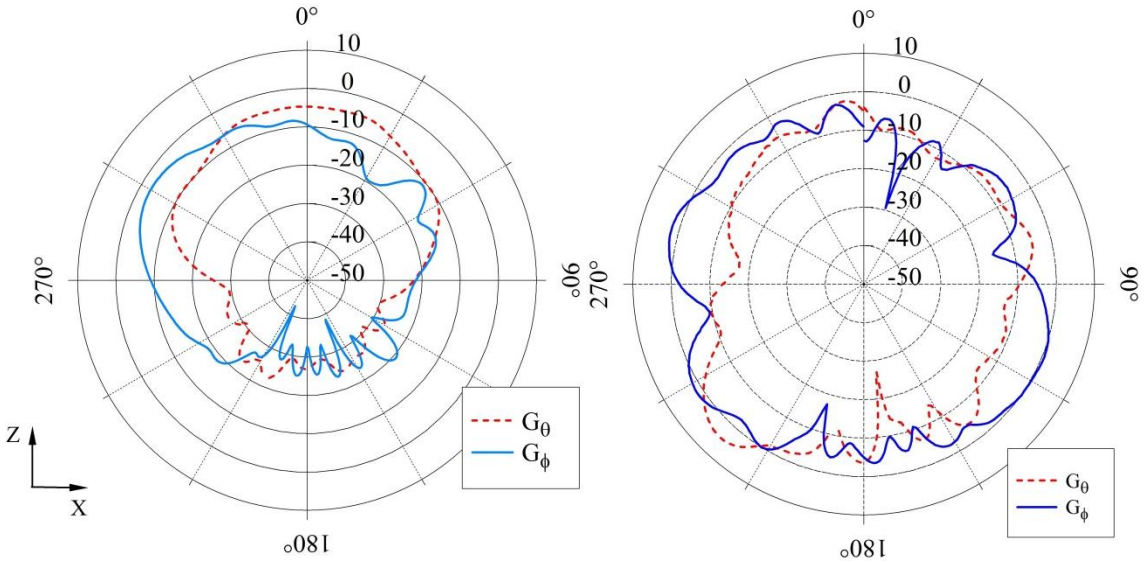

Figure 7.33: Comparison between simulated (left) and measured (right) absolute gain patterns at 3.5 GHz for the ϕ= 0º plane.

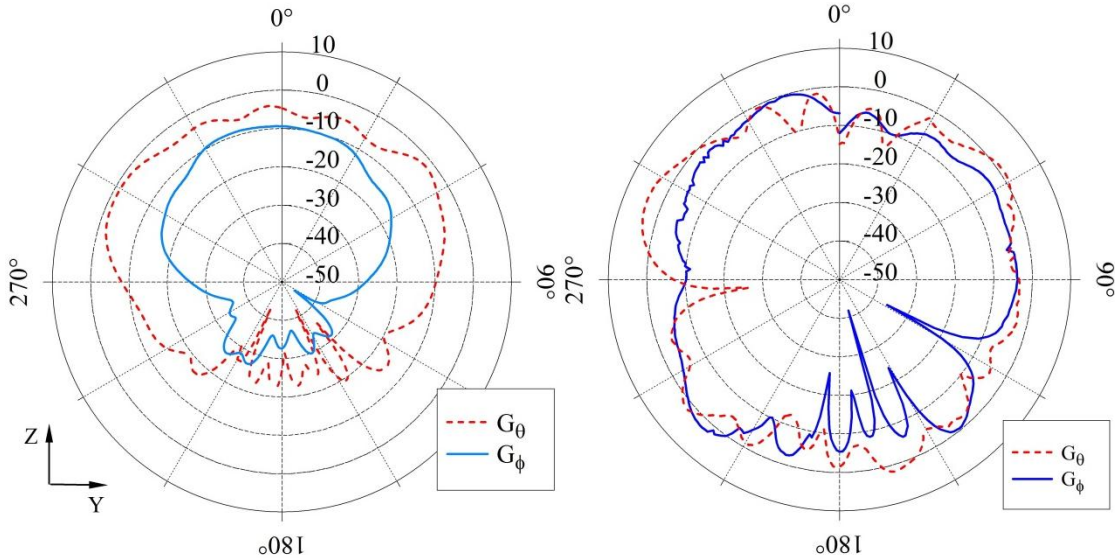

Figure 7.34: Comparison between simulated (left) and measured (right) absolute gain patterns at 3.5 GHz for the ϕ = 90º plane.

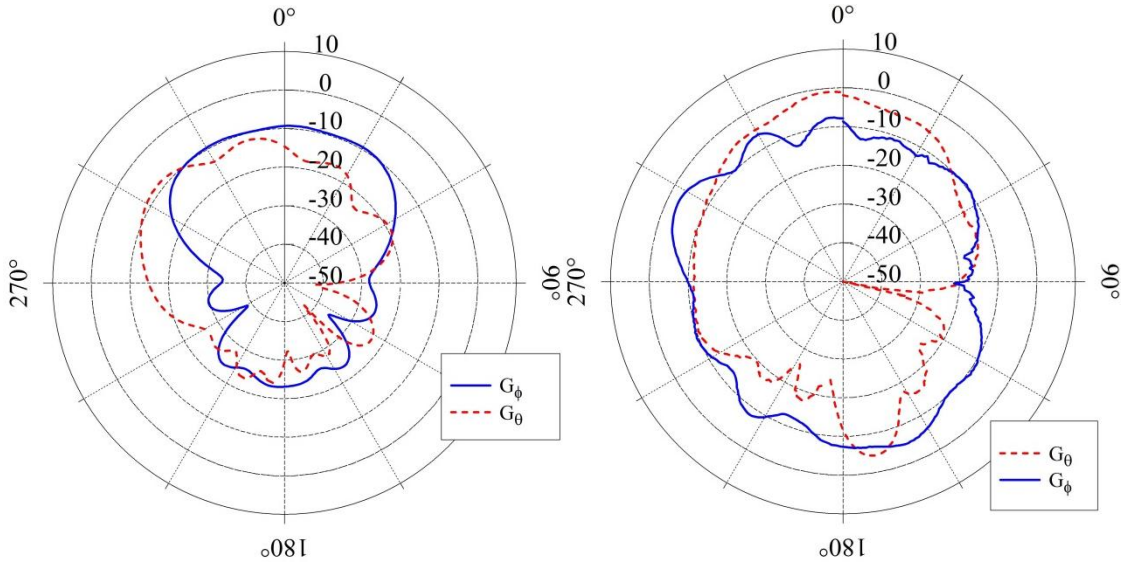

Figure 7.35: Comparison between simulated (left) and measured (right) absolute gain patterns at 2.4 GHz for the ϕ = 0º plane.

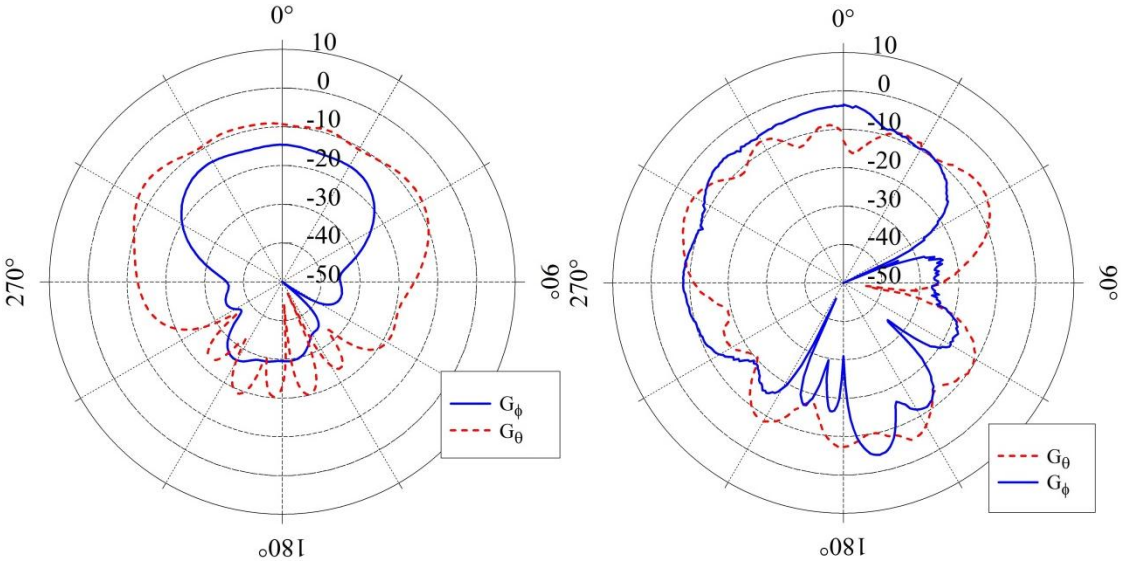

Figure 7.36: Comparison between simulated (left) and measured (right) absolute gain patterns at 2.4 GHz for the ϕ = 90º plane.

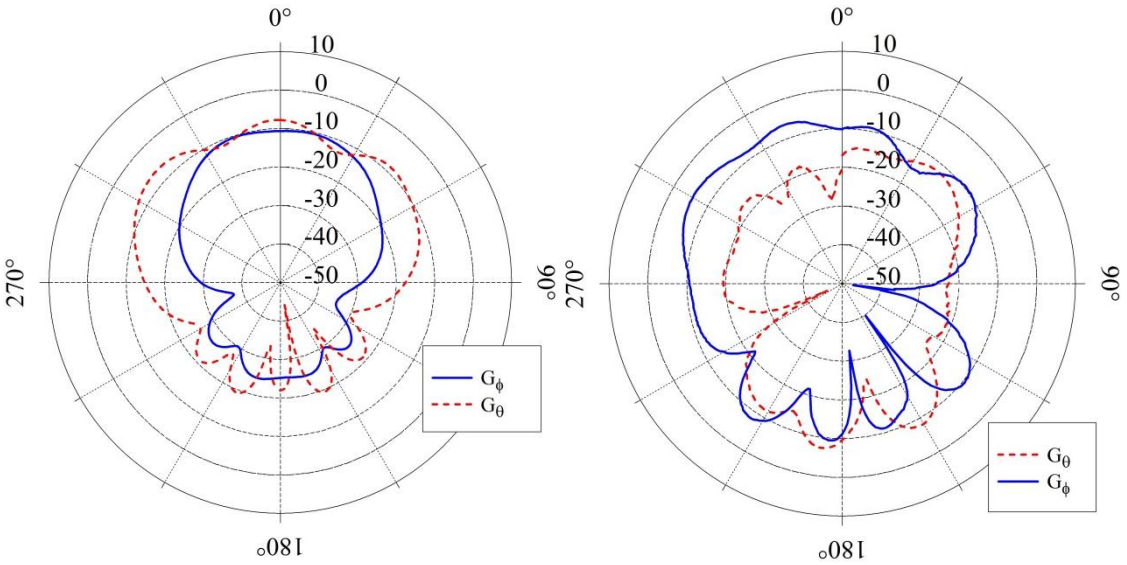

Figure 7.37: Comparison between simulated (left) and measured (right) absolute gain patterns at 2.0 GHz for the $\phi = 0^{o}$ plane.

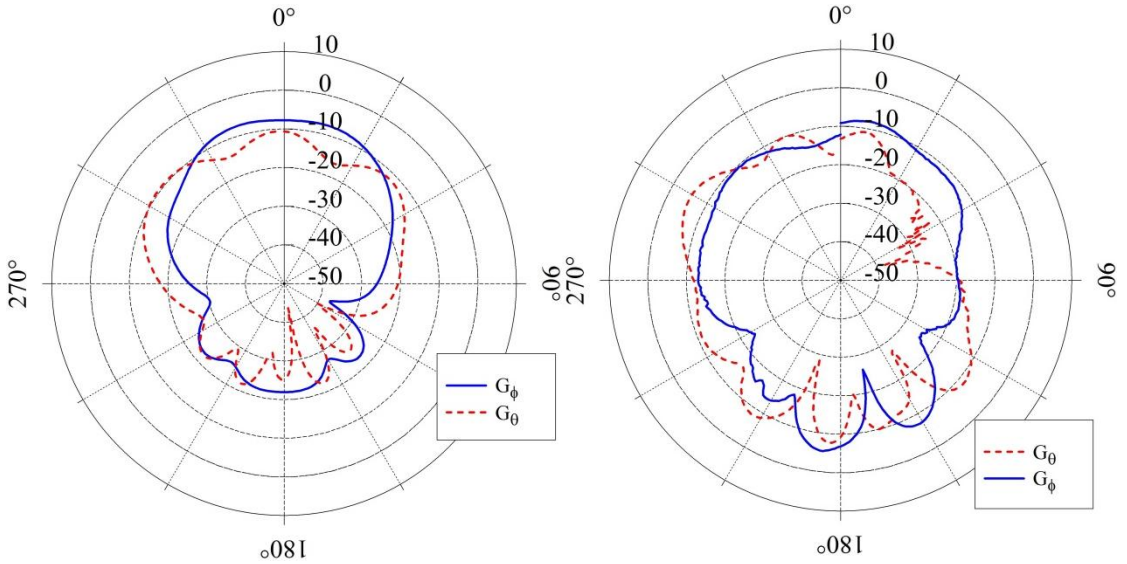

Figure 7.38: Comparison between simulated (left) and measured (right) absolute gain patterns at 2.0 GHz for the $\phi = 90^{o}$ plane.

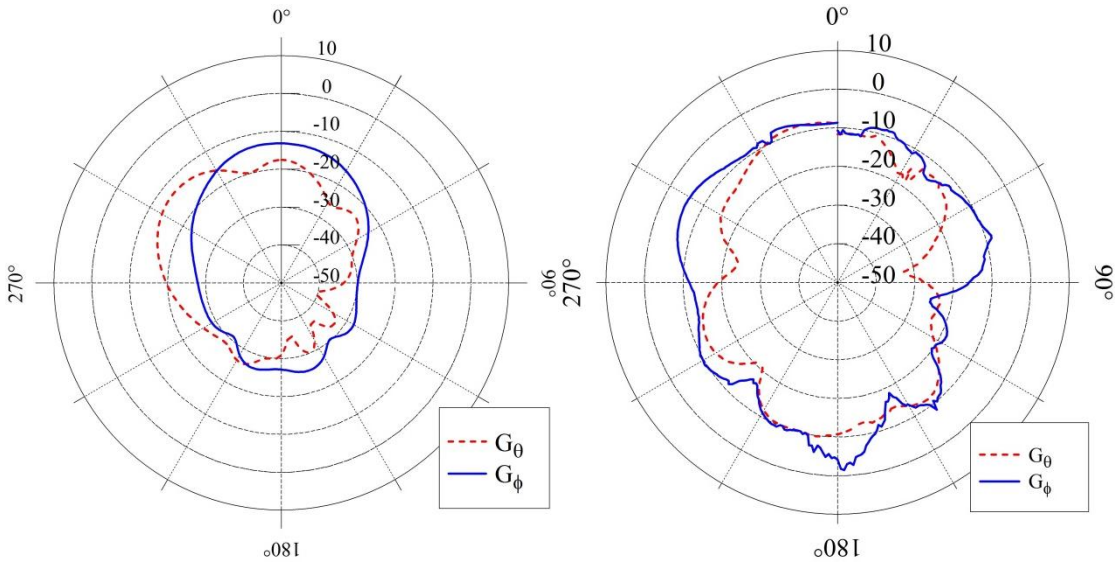

Figure 7.39: Comparison between simulated (left) and measured (right) absolute gain patterns at 1.8 GHz for the ϕ = 0º plane.

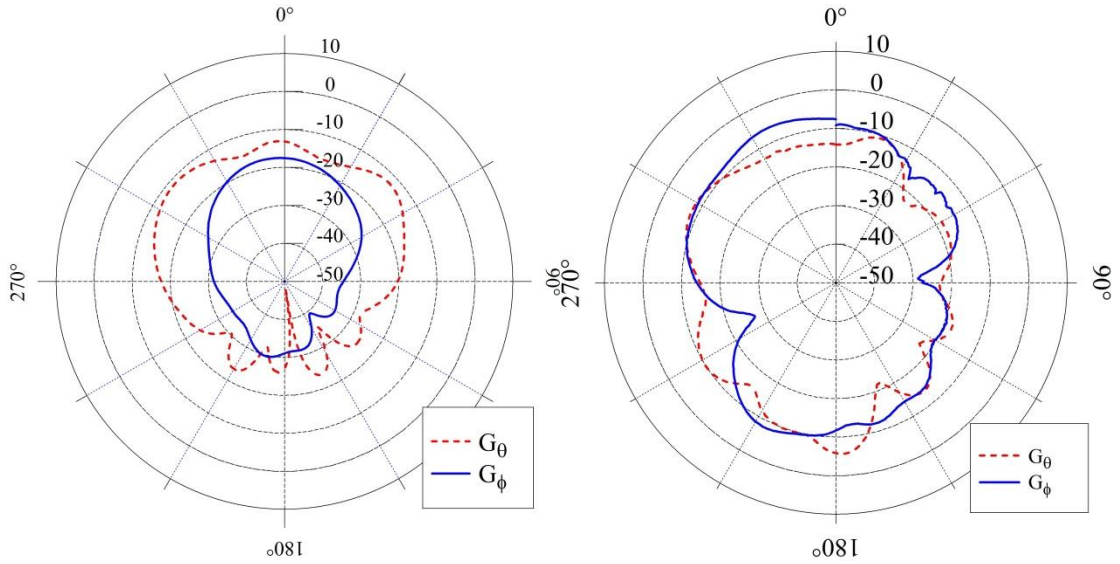

Figure 7.40: Comparison between simulated (left) and measured (right) absolute gain patterns at 1.8 GHz for the ϕ = 90º plane.

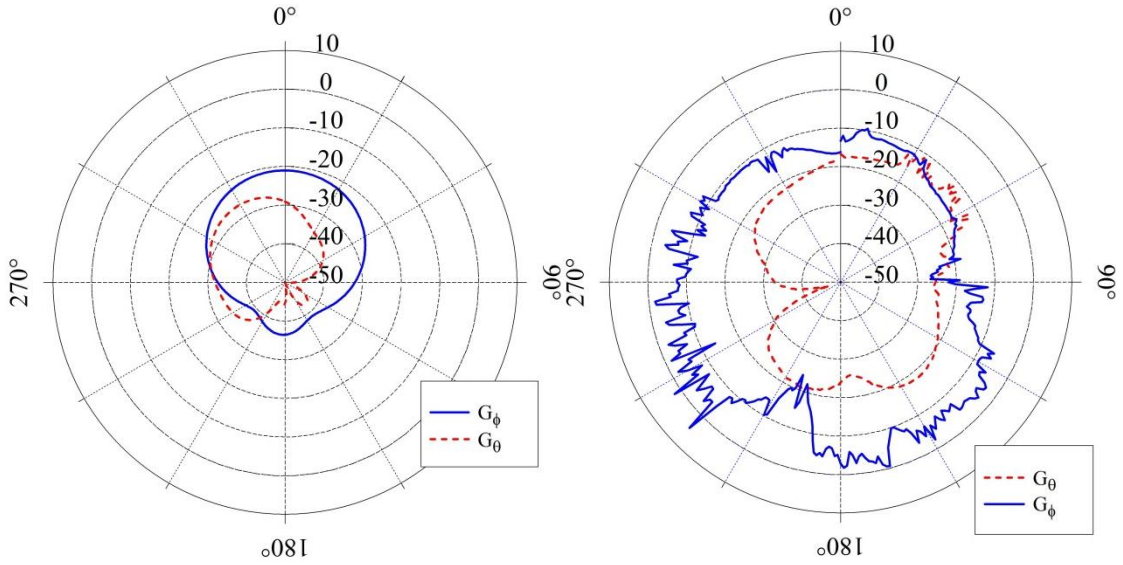

Figure 7.41: Comparison between simulated (left) and measured (right) absolute gain patterns at 0.9 GHz for the ϕ = 0º plane.

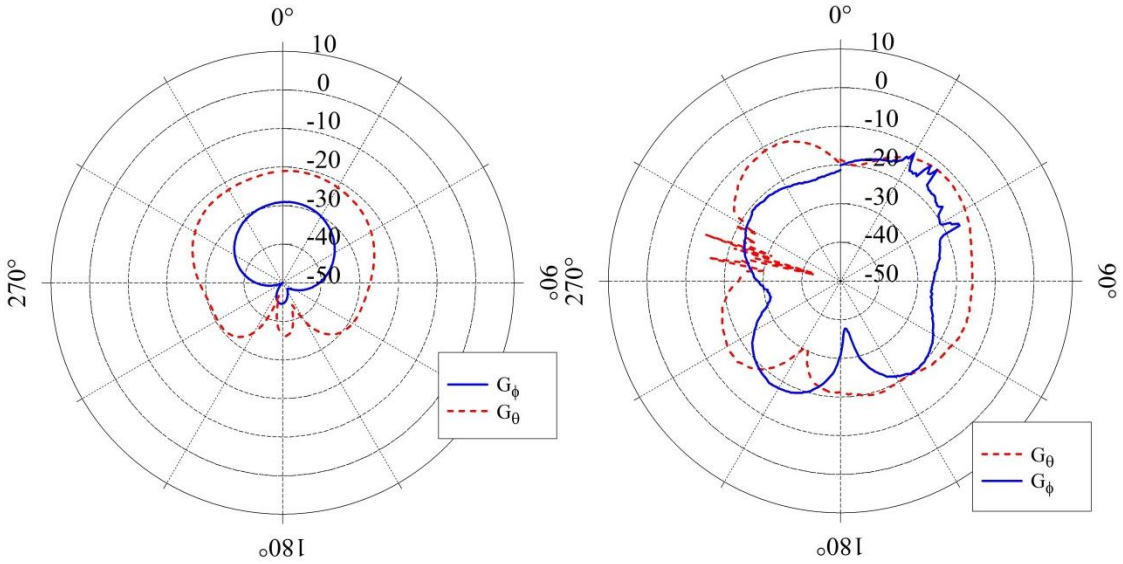

Figure 7.42: Comparison between simulated (left) and measured (right) absolute gain patterns at 0.9 GHz for the ϕ = 90º plane.

Overall, hand fabrication techniques combined with the losses in the conductive epoxy and varactor diodes can severely impact the performance of the antenna. It is believed that most of the discrepancies between simulation and measurement values for the antenna can be explained through the added losses in the epoxy and the varactors. More precise fabrication techniques must be utilized in order to eliminate construction errors.

7.4.4 Efficiency measurement

Measuring the radiation efficiency of an electrically small antenna is often done using the Wheeler cap method [32]. A Wheeler cap is a metal structure, usually cubic, that completely encloses the antenna, preventing radiation from propagating outside of the cap. The Wheeler cap works by effectively shorting out the far-field radiation of the antenna. When the Wheeler cap is placed over the antenna, a network analyzer can be used to measure the ohmic loss resistance of the antenna, without affecting the radiating environment that the antenna "sees." Likewise, when the cap is removed, the network analyzer can be used to measure the overall antenna radiation resistance. Once both of these quantities are known, a close approximation of the radiation resistance can be calculated according Equation 7.1. Once the radiation resistance of the antenna is known, the radiation efficiency of the antenna can be easily calculated using Equation 7.2, where R_{rad} is the radiation resistance of the antenna, R_{ant} is the resistance measured with the cap removed, and R_{loss} is the resistance measured with the cap on.

$$R_{rad} = R_{ant} - R_{loss} \tag{7.1}$$

$$\eta = \frac{R_{rad}}{(R_{rad}+R_{loss})} \tag{7.2}$$

In order to construct a Wheeler cap for measuring antenna efficiency, certain considerations must be made to ensure an accurate measurement. Placing a Wheeler cap over an antenna is the equivalent of putting a resonant cavity into the antenna's environment. If a resonant frequency of the cavity is close to that of the desired efficiency measurement, the Wheeler cap method will not give accurate results. Ideally, the Wheeler cap should be designed such that the first resonance of the cavity occurs above the desired measurement frequency of the antenna under test (AUT). For antennas with a very large frequency range, such as the one described in this thesis, a multiplicity of differently sized caps would be needed to ensure proper measurement for

all five frequency bands. Luckily, it is well documented [33] that as long as the cavity resonances do not occur near the frequency bands of interest, the measurement should be able to be made successfully. Equation 7.3 shows how to calculate the resonant frequencies of a rectangular cavity for both the TE and TM modes.

$$f_r = \frac{c}{2\pi}\sqrt{\left(\frac{m\pi}{a}\right)^2 + \left(\frac{n\pi}{b}\right)^2 + \left(\frac{p\pi}{bc}\right)^2} \tag{7.3}$$

$TM\ modes$	$TE\ modes\ (m = n \neq 0)$
m = 1,2,3 ...	m = 0, 1,2 ...
n = 1,2,3 ...	n = 0,1,2 ...
p = 0,1,2 ...	p = 1,2,3 ...

Another requirement in the design of a Wheeler cap is to make sure that the cap does not interfere with the near-field region of the antenna. Wheeler originally defined the "radianlength" ($\lambda_o / 2\pi$) as the length at which the near-fields transition to far-fields [32]. By ensuring that the largest dimension of the antenna is at least a radianlength away from the conducting cap, the near-field, and therefore the antenna environment, is not affected and a measurement can be taken.

Figure 7.43 is a two-dimensional diagram of the spacing required for a Wheeler cap. In the figure, *b* represents the maximum size of the antenna, *a* represents the size of the Wheeler cap, and the radianlength is also depicted.

To avoid interference of cavity resonances with the desired measured frequency bands, two different Wheeler caps were necessary to ensure constant radianlength separation and avoid cavity resonance modes. Tables 7.2 and 7.3 show the first six cavity resonances for the two Wheeler caps used.

Table 7.2: Wheeler cap resonant frequencies for 108 x 108 x 98.5 mm cap.

Cap resonant frequencies f_r (GHz)
1.964
2.061
2.485
3.106
3.168
3.459

Table 7.3: Wheeler cap resonant frequencies for 65 x 65 x 80 mm cap.

Cap resonant frequencies f_r (GHz)
2.973
3.264
3.764
4.971
4.982
5.16

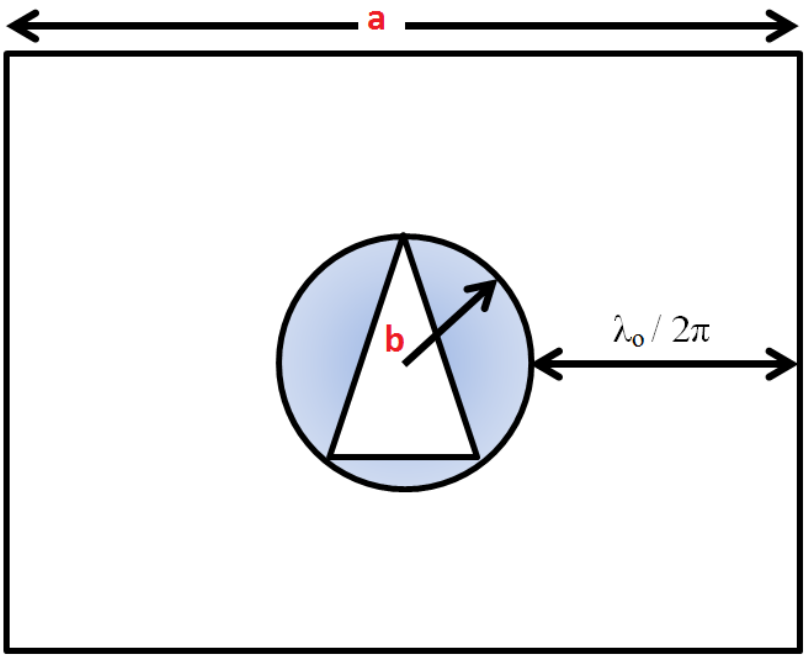

Figure 7.43: Wheeler cap design dimensions.

The Wheeler cap method is a very simple and reliable way to measure small antenna efficiencies; however, it is not appropriate for all antennas. Wheeler's method lacks the ability to differentiate between series and parallel resonant antennas. To address this lack, a modified

version of the Wheeler cap method has been developed that uses a transformation of the measured reflection coefficient to account for either a series or parallel model [34]. Using this modified method, the lowest reflection coefficient point is rotated counter-clockwise until it intersects with the Smith chart's real impedance axis. If the rotated angle is less than π, the series antenna model is used; if the rotated angle is greater than π, the parallel antenna model is used [34]. For the parallel model, Equation 7.4 is used to calculate efficiency, where G_{cap} is the conductance measured with the cap on and G_{fs} is the conductance measured with the cap removed.

$$\eta = 1 - \frac{G_{cap}}{G_{fs}} \tag{7.4}$$

Table 7.4: Measured vs. simulated efficiencies for the final design.

Match Frequency [GHz]	Simulated Radiation Efficiency [%]	Measured Radiation Efficiency [%]
3.5	20	25
2.4	6	10
2.0	5	< 1
1.8	2	< 1
0.900 (0.869 simulated)	1	< 1

Table 7.4 contains the simulated and measured efficiencies of the final antenna. It should not be surprising that the measured efficiencies of the larger modified final antenna are higher at some frequencies due to the increase of the structure's electrical size. However, for the lowest three frequencies, the measured efficiencies were less than one percent. The most likely reason for this is the extra resistive losses present in the epoxy and the varactors. Overall the simulations and measurements generally agree. It should be noted that for these extremely small sizes the efficiency is expected to be low (Section 5.2.1).

Table 7.5 contains the simulated gain figures for the final antenna design and measured gain figures for the modified final antenna. Due to its small electrical size the antenna has very small gain figures, even in simulation obtaining a maximum of -1.25 dB of gain at 3.5 GHz. The measured gains from the modified final antenna are greater than the simulated gains, but the electrical size of the antenna increased significantly with the modified final antenna and therefore larger measured gains are to be expected. Also the measured gain data contains noise

from the DC bias lines and some backplane radiation which can slightly skew the results. For the most part the measured and simulated gains correspond with each other relatively well.

Table 7.5: Measured vs. simulated gains for the final design.

Match Frequency [GHz]	Simulated Gain [dBi]	Measured Gain [dBi]
3.5	-1.25	3
2.4	-6.56	-1
2.0	-6.7	-5.4
1.8	-11.38	-6
0.900 (0.869 simulated)	-20.8	-10

Chapter 8

CONCLUSION AND FUTURE WORK

An antenna design based on an inductively loaded sector antenna was obtained for frequency tuning for the GSM 900, GSM 1800, 3G, WiFi, and WiMAX bands. The antenna was optimized for maximum frequency tuning and finally realized the entire frequency range through the use of a novel double varactor design. A DC bias network was designed and characterized through the use of realistic capacitor and varactor models to be "invisible" to the operation of the antenna. Final simulations show an antenna design capable of tuning all five required frequency bands while maintaining nearly 10% bandwidth and reasonable radiation efficiency for electrical size.

The final design was fabricated and measured and the results compared to simulation. Significant differences between the simulated and measured values were explained due to the extremely sensitive and complex nature of the antenna structure. Future work will include more precise fabrication techniques and better conductive epoxy to help address the difficult fabrication and additional resistive losses.

REFERENCES

[1] G. H. Huff and J. T. Bernhard, "Integration of packaged RF MEMs switches with radiation pattern reconfigurable square spiral microstrip antennas," *IEEE Trans. Ant. Prop.*, vol. 54, no. 2, pp. 464-469, Feb. 2006.

[2] S. Zhang, G. H. Huff, J. Feng, and J. T. Bernhard, "A pattern reconfigurable microstrip parasitic array," *IEEE Trans. Ant. Prop.*, vol. 52, no. 10, pp. 2773-2776, Oct. 2004.

[3] N. C. Soldner, P. E. Mayes, and J. T. Bernhard, "Electrically-small inductively loaded low-profile dual sector antennas in random arrays for surface exploration and mapping," in *Proc. Second IEEE Int. Conf. on Space Mission Challenges for Information Technology*, Jul. 2005, pp. 516-519.

[4] N. C. Soldner, "Design and analysis of electrically-small inductively loaded dual sector antennas for surface sensing applications," M.S. thesis, University of Illinois at Urbana-Champaign, Urbana, Illinois, 2006.

[5] H. A. Wheeler, "Fundamental limitations of small antennas," *Proc. I.R.E.*, vol. 25, pp. 1479-1484, Dec. 1947.

[6] P. E. Mayes, "Inductively loaded, stacked sector antennas," in *Proc. 25th Ann. Antenna Appl. Symp.*, Allerton Park, Monticello, Illinois, Sep. 2001, pp. 152-170.

[7] S. R. Best, "The radiation properties of electrically small folded spherical helix antennas," *IEEE Trans. Ant. Prop.*, vol. 52, no. 4, pp. 953-960, Apr. 2004.

[8] P. E. Mayes and P. W. Klock, "Impedance and gain bandwidths of broadband, electrically small, stacked conical resonator antennas," in *Proc. 27th Ann. Antenna Appl. Symp.*, Allerton Park, Monticello, Illinois, Sep. 2003, pp. 256-258.

[9] S. R. Best, "Low Q electrically small linear and elliptical polarized spherical dipole antennas," *IEEE Trans. Ant. Prop.*, vol. 53, no. 3, pp. 1047-1053, Mar. 2005.

[10] C. Harrison, "Monopole with inductive loading," *IEEE Trans. Ant. Prop.*, vol. 11, no. 4, pp. 394-400, Jul. 1963.

[11] L. J. Chu, "Physical limitations of omni-directional antennas," *Jour. App. Phy.*, vol. 19, pp. 1163-1175, Dec. 1948.

[12] D. Schaubert, F. Farrar, A. Sindoris, and S. Hayes, "Frequency agile microstrip antennas," *Ant. Prop. Society Int. Symp.*, vol. 18, pp. 601-604, Jun. 1980.

[13] D. Schaubert, F. Farrar, A. Sindoris, and S. Hayes, "Microstrip antennas with frequency agility and polarization diversity," *IEEE Trans. Ant. Prop*, vol. 29, no. 1, pp. 118-123, Jan. 1981.

[14] P. Bhartia and I. Bahl, "A frequency agile microstrip antenna," *Ant. Prop. Society Int. Symp.*, vol. 20, pp. 304-307, May 1982.

[15] J. H. Lim, G. T. Back, Y. I. Ko, C. W. Song, and T. Y. Yun, "A reconfigurable PIFA using a switchable PIN-diode and a fine-tuning varactor for USPCS/WCDMA/m-WiMAX/WLAN," *IEEE Trans. Ant. Prop.*, vol. 58, no. 7, pp. 2404-2411, July 2010.

[16] J. T. Bernhard, "Reconfigurable antennas," in *Synthesis Lectures on Antennas #4.* San Rafael, CA: Morgan & Claypool, 2007, pp. 11-20.

[17] D. J. Roscoe, L. Shafai, A. Ittipiboon, M. Cuhaci, and R. Douville, "Tunable dipole antennas," in *Proc. of the IEEE/URSI Int. Symp. on Ant. and Prop.*, vol. 2, 1993, pp. 672-675.

[18] J. Kiriazi, H. Ghali, H. Radaie, and H. Haddara, "Reconfigurable dual-band dipole antenna on silicon using series MEMS switches," in *Proc. of the IEEE/URSI Int. Symp. on Ant. and Prop.*, vol. 1, 2003, pp. 403-406.

[19] S. Kawasaki and T. Itoh, "A slot antenna with electronically tunable length," *in Proc. of the IEEE/URSI Int. Symp. on Ant. and Prop.*, vol. 1, 1991, pp. 130-133.

[20] S. V. Hum, "Analysis of varactor diode-tuned frequency agile antennas," in *2010 Proc. of the Fourth European Conf. on Ant. and Prop. (EuCAP)*, April 12-16, 2010, pp.1-5.

[21] P. E. Mayes, "Using multiple resonators for increasing the impedance bandwidth of electrically small antennas," in *Proc. 24th Ann. Ant. Appl. Symp.*, Allerton Park, Monticello, Illinois, Sep. 2000, pp. 246-269.

[22] S. R. Best, "A discussion on the properties of electrically small self-resonant wire antennas," *IEEE Antennas Propag. Mag.*, vol. 46, no. 6, pp. 9-22, Dec. 2004.

[23] Microsemi, "Microsemi product directory," April 2011. [Online]. Available: http://www.Microsemi.com

[24] Microsemi, "GC15003," "GC15014," and "GC15012" datasheets," April 2011.[Online]. Available: http://www.Microsemi.com

[25] J. T. Bernhard, J. J. Adams, M. D. Anderson, and J. M. Martin, "Measuring electrically small antennas: Details and implications," *IEEE Int. Workshop on Antenna Technology, 2009 (iWAT 2009)*, March 2-4, 2009, pp.1-4.

[26] Dielectric Laboratories, "Dielectric Laboratories product catalogue," April 2011.[Online]. Available: http://www.dilabs.com/products/products.aspx?catid=8.

[27] Dielectric Laboratories, "C11CF510J-6UN-X Multilayer CapCad," and "C06BL851X-1UN-X0T DC Block CapCad," April 2011. [Online]. Available: http://www.dliextra.net/capcad/default.aspx

[28] Microsemi, "Frequency Linear Tuning Varactors – Application Notes," April 2011. [Online]. Available: http://www.microsemi.com/micnotes/705.pdf

[29] Skyworks, "Varactor SPICE Models for RF VCO Applications," April 2011. [Online]. Available: http://www.skyworksinc.com/uploads/documents/200315B.pdf

[30] P. Sampson, private communication, Apr. 2011.

[31] Microsemi, "150 Series Outline datasheet," April 2011. [Online]. Available: http://www.Microsemi.com

[32] H. A. Wheeler, "The radiansphere around a small antenna," *Proc. of the Institute of Radio Engineers,* vol. 47, pp. 1325-1331, Aug. 1959.

[33] Y. Huang, R. M. Narayanan, and G. R. Kadambi, "On Wheeler's method for efficiency measurement of small antennas," in *Ant. Prop. Society Int. Symp.*, vol. 3, July 2001, pp. 346-349.

[34] W. E. McKinzie III, "A modified Wheeler cap method for measuring antennas efficiency," in *Ant. Prop. Society Int. Symp.*, vol. 1, July 1997, pp. 542-545.